Proton computed tomography

Catherine Thérèse Quiñones

N°d'ordre NNT : 2016LYSEI094

THESE de DOCTORAT DE L'UNIVERSITE DE LYON
opérée au sein de
l'INSA de LYON

Ecole Doctorale N° 160
ELECTRONIQUE, ELECTROTECHNIQUE, AUTOMATIQUE

Spécialité/ discipline de doctorat :
Traitement du Signal et de l'Image

Soutenue publiquement/à huis clos le 28/09/2016, par :

Catherine Therese Quiñones

Proton computed tomography

Devant le jury composé de :

Dauvergne, Denis	Directeur de Recherche, CNRS, Grenoble	Président
Royle, Gary	Professeur, University College London, London	Rapporteur
Seco, Joao	Professeur, University of Heidelberg, Heidelberg	Rapporteur
Buvat, Irène	Directeur de Recherche, CNRS, Orsay	Examinatrice
Dauvergne, Denis	Directeur de Recherche, CNRS, Grenoble	Examinateur
Létang, Jean Michel	Maître de Conférences, INSA-LYON, Villeurbanne	Directeur de thèse
Rit, Simon	Chargé de Recherche, CNRS, Villeurbanne	Co-directeur de thèse

Département FEDORA – INSA Lyon - Ecoles Doctorales – Quinquennal 2016-2020

SIGLE	ECOLE DOCTORALE	NOM ET COORDONNEES DU RESPONSABLE
CHIMIE	CHIMIE DE LYON http://www.edchimie-lyon.fr Sec : Renée EL MELHEM Bat Blaise Pascal 3e etage secretariat@edchimie-lyon.fr Insa : R. GOURDON	M. Stéphane DANIELE Institut de Recherches sur la Catalyse et l'Environnement de Lyon IRCELYON-UMR 5256 Équipe CDFA 2 avenue Albert Einstein 69626 Villeurbanne cedex directeur@edchimie-lyon.fr
E.E.A.	ELECTRONIQUE, ELECTROTECHNIQUE, AUTOMATIQUE http://edeea.ec-lyon.fr Sec : M.C. HAVGOUDOUKIAN Ecole-Doctorale.eea@ec-lyon.fr	M. Gérard SCORLETTI Ecole Centrale de Lyon 36 avenue Guy de Collongue 69134 ECULLY Tél : 04.72.18 60.97 Fax : 04 78 43 37 17 Gerard.scorletti@ec-lyon.fr
E2M2	EVOLUTION, ECOSYSTEME, MICROBIOLOGIE, MODELISATION http://e2m2.universite-lyon.fr Sec : Sylvie ROBERJOT Bât Atrium - UCB Lyon 1 04.72.44.83.62 Insa : H. CHARLES secretariat.e2m2@univ-lyon1.fr	M. Fabrice CORDEY CNRS UMR 5276 Lab. de géologie de Lyon Université Claude Bernard Lyon 1 Bât Géode 2 rue Raphaël Dubois 69622 VILLEURBANNE Cédex Tél : 06.07.53.89.13 cordey@univ-lyon1.fr
EDISS	INTERDISCIPLINAIRE SCIENCES-SANTE http://www.ediss-lyon.fr Sec : Sylvie ROBERJOT Bât Atrium - UCB Lyon 1 04.72.44.83.62 Insa : M. LAGARDE secretariat.ediss@univ-lyon1.fr	Mme Emmanuelle CANET-SOULAS INSERM U1060, CarMeN lab, Univ. Lyon 1 Bâtiment IMBL 11 avenue Jean Capelle INSA de Lyon 696621 Villeurbanne Tél : 04.72.68.49.09 Fax :04 72 68 49 16 Emmanuelle.canet@univ-lyon1.fr
INFOMATHS	INFORMATIQUE ET MATHEMATIQUES http://infomaths.univ-lyon1.fr Sec :Renée EL MELHEM Bat Blaise Pascal 3e etage infomaths@univ-lyon1.fr	Mme Sylvie CALABRETTO LIRIS – INSA de Lyon Bat Blaise Pascal 7 avenue Jean Capelle 69622 VILLEURBANNE Cedex Tél : 04.72. 43. 80. 46 Fax 04 72 43 16 87 Sylvie.calabretto@insa-lyon.fr
Matériaux	MATERIAUX DE LYON http://ed34.universite-lyon.fr Sec : M. LABOUNE PM : 71.70 –Fax : 87.12 Bat. Direction Ed.materiaux@insa-lyon.fr	M. Jean-Yves BUFFIERE INSA de Lyon MATEIS Bâtiment Saint Exupéry 7 avenue Jean Capelle 69621 VILLEURBANNE Cedex Tél : 04.72.43 71.70 Fax 04 72 43 85 28 jean-yves.buffiere@insa-lyon.fr
MEGA	MECANIQUE, ENERGETIQUE, GENIE CIVIL, ACOUSTIQUE http://mega.universite-lyon.fr Sec : M. LABOUNE PM : 71.70 –Fax : 87.12 Bat. Direction mega@insa-lyon.fr	M. Philippe BOISSE INSA de Lyon Laboratoire LAMCOS Bâtiment Jacquard 25 bis avenue Jean Capelle 69621 VILLEURBANNE Cedex Tél : 04.72 .43.71.70 Fax : 04 72 43 72 37 Philippe.boisse@insa-lyon.fr
ScSo	ScSo* http://recherche.univ-lyon2.fr/scso/ Sec : Viviane POLSINELLI Brigitte DUBOIS Insa : J.Y. TOUSSAINT Tél : 04 78 69 72 76 viviane.polsinelli@univ-lyon2.fr	M. Christian MONTES Université Lyon 2 86 rue Pasteur 69365 LYON Cedex 07 Christian.montes@univ-lyon2.fr

*ScSo : Histoire, Géographie, Aménagement, Urbanisme, Archéologie, Science politique, Sociologie, Anthropologie

———————————————————-

“I shall be telling this with a sigh
Somewhere ages and ages hence:
Two roads diverged in a wood, and I—
I took the one less traveled by,
And that has made all the difference.”
-The road not taken, Robert Frost-

———————————————————-

To my parents, Teresa and Rodrigo...
for introducing me to the fun world of physics.

Acknowledgements

In a span of three years, several individuals helped me along the way and I would like to convey my heartfelt appreciation and deepest gratitude to everyone.

I would like to start thanking the members of the Thesis Panel Committee. I could not have finished this thesis without the help of my supervisors, Simon Rit and Jean-Michel Létang, who guided me during the entire course of the PhD program. I am thankful to them for helping me pull through the whole program and for patiently answering my queries knowing that I did not have a solid background in medical imaging nor in signal processing. Their insights and inputs were the best I could ever ask for. I would also like to thank Gary Royle, Joao Seco, Irène Buvat and Denis Dauvergne for reviewing the thesis content and the manuscript, as well as for the constructive inquiries during the defense.

My sincerest gratitude also goes to my labmates, the CLB-Tomorodio group, headed by David Sarrut. We may have varied research topics but our meetings and presentations helped me a lot in understanding other imaging modalities in the field. I will surely miss the small talks and stimulating discussions we have had during coffee/tea breaks, and for all the fun we have had in the last three years. Gloria has always been a good friend and always there to extend her help whenever I needed one.

I would also like to express my gratitude to the CNRS and the Rhone-Alpes region administrations for funding my doctorate program.

I would also like to extend my gratitude to Ate Brenda and Don, for being my family here in Lyon.

Lastly, I would like to apologize to everyone who helped but I was unable to mention here. My mind might be forgetful, but my heart remembers it all.

Abstract

The use of protons in cancer treatment has been widely recognized due to the precise stopping range of protons in matter. In proton therapy treatment planning, the uncertainty in determining the range mainly stems from the inaccuracy in the conversion of the Hounsfield units obtained from x-ray computed tomography to proton stopping power. Proton CT (pCT) has been an attractive solution as this modality directly reconstructs the relative stopping power (RSP) map of the object. The conventional pCT technique is based on measurements of the energy loss of protons to reconstruct the RSP map of the object. In addition to energy loss, protons also undergo multiple Coulomb scattering and nuclear interactions which could reveal other interesting properties of the materials not visible with the RSP maps.

This PhD work is to investigate proton interactions through Monte Carlo simulations in GATE and to use this information to reconstruct a map of the object through filtered back-projection along the most likely proton paths. Aside from the conventional energy-loss pCT, two pCT modalities have been investigated and implemented. The first one is called attenuation pCT which is carried out by using the attenuation of protons to reconstruct the linear inelastic nuclear cross-section map of the object. The second pCT modality is called scattering pCT which is performed by utilizing proton scattering from measurements of the angular variance to reconstruct the relative scattering power map which is related to the radiation length of the material. The accuracy, precision and spatial resolution of the images reconstructed from the two pCT modalities were evaluated qualitatively and quantitatively and compared with the conventional energy-loss pCT.

While energy-loss pCT already provides the information needed to calculate the proton range for treatment planning, attenuation pCT and scattering pCT give complementary information about the object. For one, scattering pCT and attenuation pCT images provide an additional information intrinsic to the materials in the object. Another is that, in some studied cases, attenuation pCT images demonstrate a better spatial resolution and showed features that would supplement energy-loss pCT reconstructions.

Keywords: proton computed tomography, energy-loss proton CT, attenuation proton CT, scattering proton CT, distance-driven binning, relative stopping power, linear inelastic cross-section, radiation length, filtered backprojection

Résumé

L'utilisation de protons dans le traitement du cancer est largement reconnue grâce au parcours fini des protons dans la matière. Pour la planification du traitement par protons, l'incertitude dans la détermination de la longueur du parcours des protons provient principalement de l'inexactitude dans la conversion des unités Hounsfield (obtenues à partir de tomographie rayons X) en pouvoir d'arrêt des protons. La tomographie proton (pCT) est une solution attrayante car cette modalité reconstruit directement la carte du pouvoir d'arrêt relatif à l'eau (RSP) de l'objet. La technique pCT classique est basée sur la mesure de la perte d'énergie des protons pour reconstruire la carte du RSP de l'objet. En plus de la perte d'énergie, les protons subissent également des diffusions coulombiennes multiples et des interactions nucléaires qui pourraient révéler d'autres propriétés intéressantes des matériaux non visibles avec les cartes de RSP.

Ce travail de thèse a consisté à étudier les interactions de protons au travers de simulations Monte Carlo par le logiciel GATE et d'utiliser ces informations pour reconstruire une carte de l'objet par rétroprojection filtrée le long des chemins les plus vraisemblables des protons. Mise à part la méthode pCT conventionnelle par perte d'énergie, deux modalités de pCT ont été étudiées et mises en œuvre. La première est la pCT par atténuation qui est réalisée en utilisant l'atténuation des protons pour reconstruire le coefficient d'atténuation linéique des interactions nucléaires de l'objet. La deuxième modalité pCT est appelée pCT par diffusion qui est effectuée en mesurant la variation angulaire due à la diffusion coulombienne pour reconstruire la carte de pouvoir de diffusion, liée à la longueur de radiation du matériau. L'exactitude, la précision et la résolution spatiale des images reconstruites à partir des deux modalités de pCT ont été évaluées qualitativement et quantitativement et comparées à la pCT conventionnelle par perte d'énergie.

Alors que la pCT par perte d'énergie fournit déjà les informations nécessaires pour calculer la longueur du parcours des protons pour la planification du traitement, la pCT par atténuation et par diffusion donnent des informations complémentaires sur l'objet. D'une part, les images pCT par diffusion et par atténuation fournissent une information supplémentaire intrinsèque aux matériaux de l'objet. D'autre part, dans certains des cas étudiés, les images pCT par atténuation démontrent une meilleure résolution spatiale dont l'information fournie compléterait celle de la pCT par perte d'énergie.

Mots clés: tomographie proton, tomographie proton par perte d'énergie, tomographie proton par atténuation, tomographie proton par diffusion, échantillonnage des projections piloté par la distance, pouvoir d'arrêt relatif, section nucléaire efficace, longueur de radiation, rétroprojection filtrée

List of abbreviations

AgBr silver bromide

AQUA Advanced Quality Assurance

ART algebraic reconstruction technique

BPF backprojection-then-filtering

CERN European Organization for Nuclear Research

CMOS APS complementary metal oxide semi-conductor active pixel sensor

CNAO Centro Nazionale di Adroterapia Oncologica

CREATIS Centre de Recherche en Acquisition et Traitement de l'Image pour la Santé

CSDA continuous-slowing-down-approximation

CsI cesium iodide

CSP cubic-spline path

CSUSB California State University, San Bernadino

CT computed tomography

DAQ data acquisition

DECT dual-energy CT

DMR dual modality reconstruction

FBP Filtered back-projections

FDK Feldkamp-Davis-Kress

FNAL Fermi National Accelerator Laboratory

FWHM Full-width-at-half-maximum

GATE Geant4 Application for Emission Tomography

GEANT4 Geometry and Tracking 4th generation v10.01.p02

GEM gas electron multiplier

GPU graphical processing unit

HPGe hyperpure germanium detector

HU Hounsfield unit

I mean excitation energy

IMRT intensity-modulated photon therapy

INFN Istituto Nazionale di Fisica Nucleare

IPNL Institut de Physique Nucleaire

KEK National Laboratory for High Energy Physics

KVI-CART KVI-Center for Advanced Radiation Technology

LAMPF Los Alamos Meson Physics Facility

LBL Lawrence Berkeley Laboratory

LET linear energy transfer

LLU Loma Linda University

LLUMC Loma Linda University Medical Center

LMU Ludwig Maximilians University

LUT look-up-table

MC Monte Carlo

MCNPX Monte Carlo N-Particle eXtended

MCS multiple Coulomb scattering

MGH Massachusetts General Hospital

MLP most-likely path

MTF modulation transfer function

MWPC multiwire proportional chamber

NaI sodium iodide

NIRS National Institute of Radiological Sciences

NIST National Institute of Standards and Technology

NIU Northern Illinois University

NSR nuclear scattering radiography

PBA pencil beam algorithm

PCI phase contrast x-ray imaging

pCT proton computed tomography

PET positron emission tomography

PMB Physics in Medicine and Biology

PRaVDA Proton Radiotherapy Verification and Dosimetry Applications

pRG proton radiograph

PRIMA PRoton IMAging

PSD position-sensitive detector

PSI Paul Scherrer Institute

RBE relative biological effectiveness

RED relative electron density

RERD residual energy-range detector

ROI region-of-interest

RSP relative stopping power

SART simultaneous algebraic reconstruction technique

Sci-Fi scintillating fiber hodoscope

SCIPP Santa Cruz Institute of Particle Physics

SiPM silicon photomultiplier

SiSD silicon strip detector

SLP straight-line path

SPECT single-photon emission computed tomography

SSC single scattering

TPC time projection chamber

TPS treatment planning software

UCSC University of California Santa Cruz

WEPL water-equivalent path length

WLSF wavelength shifting fiber

xCT x-ray computed tomography

Contents

List of Tables

List of Figures

Introduction

The use of protons in cancer treatment has been widely recognized due to the precise stopping range of protons in matter. In proton therapy treatment planning, the uncertainty in determining the range mainly stems from the inaccuracy in the conversion of the Hounsfield units obtained from x-ray computed tomography to proton stopping power. Proton CT (pCT) has been an attractive solution as this modality directly reconstructs the relative stopping power (RSP) map of the object. The conventional pCT technique is based on measurements of the energy loss of protons to reconstruct the RSP map of the object. In addition to energy loss, protons also undergo multiple Coulomb scattering and nuclear interactions which could reveal other interesting properties of the materials not visible with the RSP maps.

This PhD work is to investigate proton interactions through Monte Carlo simulations in GATE and to use this information to reconstruct a map of the object through filtered back-projection along the most likely proton paths. Aside from the conventional energy-loss pCT, two pCT modalities have been investigated and implemented. The first one is called attenuation pCT which is carried out by using the attenuation of protons to reconstruct the linear inelastic nuclear cross-section map of the object. The second pCT modality is called scattering pCT which is performed by utilizing proton scattering from measurements of the angular variance to reconstruct the relative scattering power map which is related to the radiation length of the material. The accuracy, precision and spatial resolution of the images reconstructed from the two pCT modalities were evaluated qualitatively and quantitatively and compared with the conventional energy-loss pCT.

The manuscript is structured as follows: chapter 1 and chapter 2 are extensive reviews of the literature on proton therapy and proton imaging that led to the actual work; chapter 3 focuses on the investigation of the physical processes of proton interactions in matter together with the Monte Carlo (MC) validation of the processes; chapter 4 describes the energy-loss proton CT technique to reconstruct the relative stopping power (RSP) map; chapter 5 describes attenuation pCT to reconstruct the inelastic nuclear cross-section κ-map; chapter 6 describes the methods for scattering proton CT to reconstruct the relative scattering power map and finally chapter 7 presents the conclusion and outlook of the study.

Chapter 1

Protons for cancer therapy

Contents

1.1 Clinical rationale

Radiation therapy or radiotherapy is a non-invasive procedure in treating cancer. The aim in radiotherapy is to deliver a maximum dose to the tumor volume while the surrounding healthy tissues should receive minimal dose. Different radiation sources interact differently in human tissues and consequently affect the effectiveness of the treatment. Conventional radiotherapy uses high energetic x-ray beams to damage the cancer cells. By examining the depth dose profile of x-rays in water as shown in Figure 1.1, it is observed that x-rays deposit a high entrance dose and then a gradual decrease of the dose after reaching its peak. Suppose a tumor is located at a depth of 140 mm, this means that healthy tissues near the skin region receive the maximum dose and a significant amount of dose deposition after the tumor volume is inevitable. The potential of using protons and heavy-ions in radiation therapy was first proposed by Wilson (1946) after discovering that protons and heavy ions deposit a maximum dose, also called the Bragg peak, at a precise depth in a tissue as shown in Figure 1.1. Not only the tumor volume receives the maximum dose, but importantly, the surrounding healthy tissues receive a minimal amount of dose. Conformal treatment is achieved by positioning the Bragg peak such that it hits the tumor volume, either by varying the incident proton energy or by placing range shifters along the beam-line before the patient.

Experiments on the physical and radiobiological properties of proton beams have been studied as early as 1948 at the Lawrence Berkeley Laboratory (LBL) in the USA in 1946 and their first cancer patients were finally treated with proton beams in 1955 (Tobias et al., 1958). It was not until 1990 that proton treatment facilities were adopted in clinical practice. While the development of intensity-modulated photon therapy (IMRT) increased dose conformity at least for regularly shaped targets,

however, Paganetti (2012) also pointed out that the integral dose is still higher with photons than with protons. Various dosimetric studies have demonstrated that normal tissue sparing is better with protons and ions (Paganetti, 2011). This makes proton/ion therapy a better choice especially for deep-seated tumors and tumors close to critical structures, e.g. head-and-neck treatments. The low dose to healthy tissues could also reduce the risk of developing secondary cancer. In addition, pediatric patients could also benefit from this procedure as it could limit the radiation exposure to healthy and developing tissues.

Despite the promising potential of particle therapy in cancer treatment, the benefits could not be utilized efficiently right from the start because of the limitations in patient imaging and beam delivery. The large capital expenditure to build proton accelerators when it was first proposed hindered its widespread clinical applications. However, in the past 15 years, along with the advancements in accelerator technology coupled with the reduction of operational costs, hospitals around the world are adapting this technology to treat cancer patients that benefit the most from the depth-dose advantage of proton therapy. Furthermore, due to the increased awareness of the advantages of charged particle therapy, a phase of rapid expansion of proton treatment centers throughout the world has been observed. Table A.1 and Table A.3 show the lists of currently operating charged particle therapy centers in the world and centers under construction to date. A majority of these particle therapy facilities use protons beams and only a few of these centers are combined proton/carbon ion facilities. Carbon ions provide superior physical dose distributions due to reduced lateral scattering, reduced range straggling, and an increased entrance-to-peak ratio as shown in Figure 1.1. Moreover, carbon ions have a higher linear energy transfer (LET) than protons and photons. Because of this, it is believed that carbon ions are more effective in killing oxygen-deficient tumors that are radioresistant to both protons and photons (Held et al., 2016). Despite the improved physical and biological aspects of carbon ions over protons, more hospitals are still opting to build proton facilities as evidenced by the growing number of proton therapy facilities. One reason is that carbon ion facilities cost about two to three times more than proton facilities. Another is that, despite the sharper Bragg peak, which could be an advantage for better tumor control, however, this also makes carbon ion treatment more susceptible to uncertainties in the treatment planning, i.e. increased risk of normal tissue damage compared with protons. Furthermore, unlike the distal falloff of protons at the end of range, the depth-dose profile of carbon ions is characterized by a nuclear tail consisting of secondary particles produced from the fragmentation of carbon ions. Modeling of the dose distribution should be done not only for the *primaries* but also for high-LET secondary particles along the beam line and in the tail region to avoid damage to normal tissues (Paganetti, 2002). Despite the theoretical advantage in terms of biological and physical characteristics of carbon ions over protons, clinical evidence of the benefits is still lacking (Jakel et al., 2013). The use of helium ions was also proposed to replace protons for improved dose conformation while having a similar relative biological effectiveness (RBE) to protons (Jakel et al., 2013). The merits and demerits between the choice of particle in therapeutic purposes have been a subject of debates for many years, partly due to lack of clinical evidence (Zips and Baumann, 2013).

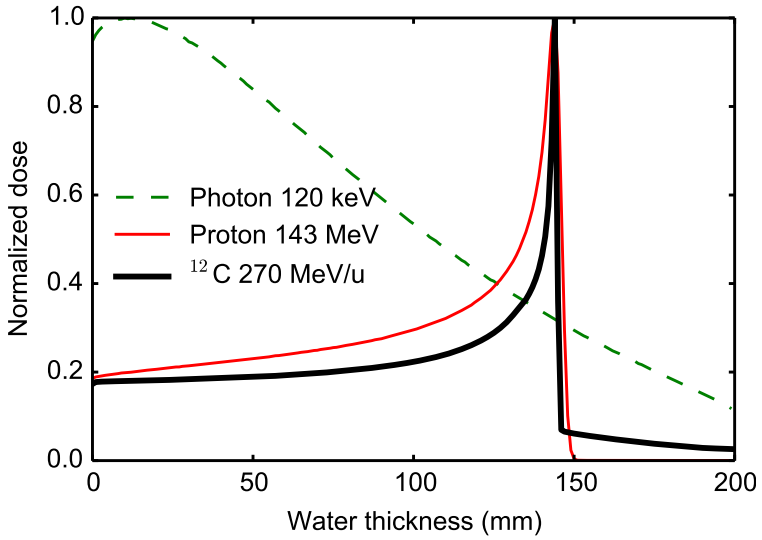

Figure 1.1: Normalized depth-dose curves from GEANT4 simulations of photons and ions traversing a 20 cm water box.

1.2 Uncertainties in the treatment planning

The uncertainties inherent in the conventional radiotherapy, which include geometrical variations, patient positioning and organ motion, are also present in proton radiotherapy. However, there exists an important source of uncertainty specific to proton therapy, i.e. an estimate of the proton range. In proton therapy treatment planning, the two important quantities to be determined are: (1) the incident energy so that the protons will stop where the tumor volume is located, i.e the proton range and (2) the dose that will be deposited. Both quantities can be estimated by integrating the different stopping power (discussed further in subsection 3.1.1) of the materials along the beam-line. Multiple tradeoffs are necessary and by understanding these sources of error, an optimized treatment plan could be achieved.

Range uncertainty

In most proton therapy centers, range verification and dose calculations are carried out using the images acquired from x-ray computed tomography (xCT). Protons and photons propagate differently in the patient, thus, the Hounsfield unit (HU) derived from xCT images are converted to proton stopping power by means of a calibration curve derived from stoichiometric measurements of different tissue-like materials (Schneider et al., 1996; Yang et al., 2012; Ainsley and Yeager, 2014). The calibration technique can be summarized as follows: First, the constant parameters for the photoelectric effect coherent scattering and Klein-Nishina cross-sections of photon interactions are calculated. Second, the elemental proton stopping powers are then derived from these parameters. Third, the proton stopping power and HU for real tissue materials are then calculated including basic conversions for the HU obtained from xCT images to proton stopping power for all types of material encountered. Lastly, three separate linear curves for organ-like tissue, fat-like tissue,

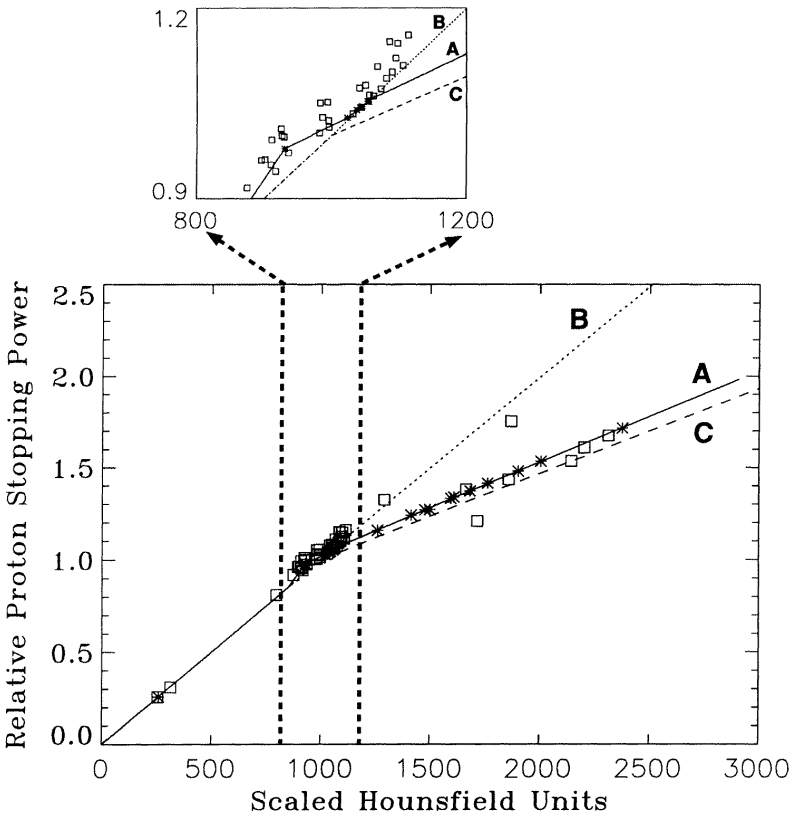

Figure 1.2: Calibration curves for the transformation of Hounsfield values into relative proton stopping power. The solid line shows the stoichiometric calibration (A) for biological tissues, the dotted line the tissue substitute calibration for Mylar/Melinex/PTFE (B) and the dashed line the tissue substitute calibration for B110/SB5 (C). The squares represent calculations for tissue substitutes and the stars are calculations based on the chemical composition of real tissues. The small plot shows in detail the Hounsfield number range corresponding to soft tissue. Figure taken from Schneider et al. (1996).

and bone-like tissue are created and combined to make a final calibration curve as shown in Figure 1.2.

The conversion of the HU to proton stopping power based on a stoichiometric conversion using animal tissues has been reported to be up to ±1.8% for bone and ±1.1% for soft tissues which translates into a range uncertainty of 1-3 mm (Schaffner and Pedroni, 1998). Another source of uncertainty is range straggling which will be described further in subsection 3.1.3. This means that protons of the same incident energy will not stop at the same position. For this reason, there is usually a variability rate or safety margin that is introduced into the calculations for proton treatment planning. Not taking into account the safety margins could have more severe consequences in proton therapy treatment planning than in the conventional radiation therapy. For instance, underestimation of the range margin would shift the sharp distal fall-off, causing an under-dosage of the tumor and high-risk damage to normal tissues. Paganetti (2012) has outlined the different safety margins imposed by some proton therapy facilities. For example, at the Massachusetts General Hos-

pital (MGH), an uncertainty in the proton beam range of 3.5% plus an additional 1 mm of the range is assumed. This results in a deliberate overshoot of 8 mm for a 20 cm range field in soft tissue which is substantial. Some hospitals, e.g. the MD Anderson Proton therapy center in Houston (Mohan and Bortfeld, 2011), Loma Linda University Medical Center (LLUMC) and Roberts Proton Therapy Center at the University of Pennsylvania, all apply 3.5% + 3 mm while the University of Florida Proton Therapy Institute uses 2.5% + 1.5 mm. A larger safety margin translates to less conformal dose distribution.

A source of uncertainty in the stoichiometric calibration method is the estimation of the I-values used to convert the HU values to proton stopping power (Besemer et al., 2013). It is reported that the uncertainties in the I-value estimate for different materials can be in the order of 10-15%, hence, limiting the proton range accuracy. Moreover, treatment planning softwares use the I-value of water to represent all human tissues. The I-value variations between 67.2 and 80 eV can have a substantial impact on the proton beam range (Andreo, 2009). Difference between 75 and 80 eV results in a 0.8 to 1.2% difference in the predicted stopping power in the therapeutic energy range. The small discrepancies in the calculated local energy deposition can result in a significant change in range because they may accumulate over the entire beam path (Matsufuji et al., 1998; Paganetti, 2012). These numbers do include the uncertainty in the I-value. Thus, the pure uncertainty due to stopping power conversion is presumably ∼0.5%.

Dose uncertainty

To produce the depth-dose profile in the patient (similar to what is shown in Figure 1.1), dose calculations by the treatment planning software (TPS) for proton therapy can be based on either analytical or Monte Carlo (MC) methods. The choice of the modality is usually a trade-off between accuracy and speed.

High accuracy dose calculations can be achieved with MC simulations especially for heterogeneous media. MC methods use theoretical models or experimental cross-section data for electromagnetic and nuclear interactions for simulations on a particle-by-particle basis. It not only simulates detailed physical interactions of different particle types but the randomness of the different interactions are also accounted for. One drawback of this method is the computational demands. MC simulations involve tracking the detailed history of each particle at every step (energy, direction, position) and calculations are based on probabilistic physical models to simulate the trajectory of the particle. MC codes such as Monte Carlo N-Particle eXtended (MCNPX) (Waters et al., 2007) and GEANT4 (Allison et al., 2006) were already experimentally validated to simulate particle interactions with high accuracy. Single-tracking MC method is time-consuming and requires high computer processing capabilities. Although this issue can be addressed through parallel computing and the use of a graphical processing unit (GPU) (Jia et al., 2012; Souris et al., 2016), single-tracking MC simulations in TPSs are not yet widely used in clinical practice. An alternative is to use track-repeating algorithms (Yepes et al., 2016) wherein the probability density of each interaction in water, e.g. collision and scatter cross-sections, based on MC generated data are used to provide faster dose calculations.

Despite the better accuracy of MC based TPS system, analytical methods such as the pencil beam algorithm (PBA) (Schaffner, 2008; Ciangaru et al., 2005; Szymanowski and Oelfke, 2002) and ray tracing (Calvel et al., 2008) are still widely used. In PBA, a broad beam is divided into smaller pixels and each individual pencil beam is transported through the target material and the sum of the dose distributions from each pencil beam are then calculated to determine the total dose. Ray-tracing methods, on the other hand, involve converting the WEPL along one dimension to extract the predetermined dose in water. This method is faster in terms of calculation speed, however, it is not robust for areas with heterogeneities unlike the PBA method.

Another source of dose uncertainty is the estimate of the *inelastic* nuclear cross-sections for different materials (Palmans and Verhaegen, 2005). Dose deposition is mainly caused by the *inelastic* nuclear interactions not only by the *primaries* but also the *secondaries*. Current methods involve quantifying these physical processes and scaling them accordingly in terms of the HU. Although the uncertainty is small for low energies, e.g. 60 MeV for ocular tumors, this effect could be substantial in the high-energy range, i.e. above 150 MeV.

Other sources of uncertainties

While the above lists the main factors of uncertainties, other causes of uncertainties in the treatment planning include patient setup, surgical implants, surgical glues, dental implants and reconstructive surgery. Respiratory and cardiac motion could also be a source of uncertainty and there are various ways in the literature to reduce xCT artifacts due to motion. In addition, an adaptive proton plan (Schulte and Wroe, 2012) should be carried out due to the shrinkage of tumors over the course of treatment. This can be achieved by recalculating the proton stopping power of the tissues to adjust the dose along the beam path.

1.3 Imaging alternatives in treatment planning

Other imaging techniques may reduce the uncertainty in the determination of the proton stopping power. A new approach in xCT imaging technique which uses two x-ray spectra, called dual-energy CT (DECT) demonstrate a better RSP estimate than the single energy technique. Hybrid techniques such as positron emission tomography (PET)-CT scanner have been investigated at the Loma Linda University (LLU). While conventional xCT imaging technique is based on the measurement of the attenuation of x-ray beams after traversing the patient, a new technique, also known as phase contrast x-ray imaging (PCI), which is based on measurements of the interference patterns of the x-ray beam to determine the refractive index of different materials (Fu et al., 2013) could also be a potential for diagnosis applications.

Despite the potential of the aforementioned imaging modalities for diagnostic and treatment planning applications for proton therapy, these techniques still involve calibration schemes which in a way limits the efficiency of the method. Scaling of the quantities derived from photon measurements to the equivalent for protons by means of calibration curves is not robust to uncertainties. For this reason, direct

imaging with protons to acquire the stopping power map of the object has been gaining interest in the past years. This mode of imaging will be further discussed in chapter 2.

Chapter 2

Protons for medical imaging

Contents

In radiotherapy, an imaging modality serves four purposes: (1) for diagnosis, i.e. to show the anatomy of interest; (2) for dosimetry, i.e. to provide physical quantities for dose calculations; (3) to properly position the patient just before treatment and (4) for functional imaging. In proton therapy, an xCT image could already provide the information needed both for diagnosis and dose calculation purposes. However, the intrinsic uncertainties in xCT images for proton therapy limits its efficiency for dose calculations and hence, paved the way for a revived interest to use protons to address this issue.

2.1 Historical development of proton imaging

Proton imaging, in general, is based on transmission measurements, i.e. the information of the incoming and transmitted particle/s, be it *primaries* or *secondaries*. Unlike x-rays, where imaging is mainly based on the attenuation information, proton interaction in tissues involves several processes, thus, proton imaging could be carried out in several ways (Cookson, 1974; Bopp et al., 2013, 2015).

2.1.1 Attenuation based proton imaging

Early images using proton beams were acquired using the attenuation of protons which is similar in concept as in x-ray radiography, where the particles that come out of the object are detected by radiographic films placed downstream the object to be imaged. The incident energy of the proton is just enough such that the proton range

falls just a few centimeters after the object, hence, it was also called the end-of-range method. In 1968 at the Harvard Cyclotron Laboratory, Koehler (1968) produced the first proton radiograph using a 160 MeV proton beam (reduced to 137 MeV by a lead scatterer) incident onto a 18 g/cm^2 thick stack of aluminum absorbers with a piece of 0.035 g/cm^2 thick aluminum foil inserted in the center. Although the insert only contributes a small portion of the total thickness of the aluminum, the radiograph revealed a clear outline of the insert, i.e. a much better contrast, but with a relatively poorer spatial resolution than those produced with x-rays. The fuzziness of the edges was reported to be caused by the small angle scattering of the protons in the aluminum that extended up to 0.15 cm from the true edge. This effect has also been observed by West and Sherwood (1972) in a 160 MeV proton radiograph of biological tissues, that of a mouse (Figure 2.1), and of some objects for possible applications in nondestructive testing (West and Sherwood, 1973; West, 1975). Steward and Koehler (1973*a*) demonstrate the first application of proton radiography on tumor detection, i.e. proton radiographs of several normal human tissues and malignant tumors, e.g. a human brain with a primary neuroectodermal tumor and a metastatic tumor from the pancreas. It has been reported that a dose of less than 1 cGy at the first surface could already yield satisfactory images. X-ray radiographs were also carried out on the same specimens, under the same conditions, to compare with the proton radiographs and it has been reported that the proton beam method offers a better means of visualization of the internal structure and tumors in the specimen than with x-rays. This is because the transmission of protons is relatively insensitive to variations in the chemical composition of the absorber but, in comparison, is highly sensitive to density variations. The method was found of great importance considering that most diseases, including cancer, originate and largely reside within soft tissues. Steward and Koehler (1973*b*) performed more experiments on human brain autopsy specimens using 125 cGy of first surface dose for each exposure and confirmed the useful contrast in proton radiographs to detect even the pathological changes within tissue structures which were not visible on x-ray radiographs, e.g. intracerebral hemorrhage (Figure 2.2). Steward and Koehler (1974) also conducted proton radiographs on tumor-bearing areas within the breast with considerably lower tissue doses (0.3 cGy) than those used in conventional mammography or even with xeroradiographic methods.

Although the technique of attenuation radiography has been reported to be a powerful tool which complements and in some instances even supplements x-ray radiography, proton imaging has not progressed much in this direction because of the gaining popularity and the improved spatial resolution of x-ray radiography. It is, however, worth noting that in some literature where proton scattering radiography is mentioned, they are in principle actually attenuation radiography, e.g. in West and Sherwood (1973) and Cookson (1974). The interplay of the attenuation and scattering in the proton radiographs might cause naming ambiguities in the context of this manuscript, and thus, the term attenuation is chosen for this kind of transmission imaging to differentiate it from scattering imaging which will be discussed further in chapter 6.

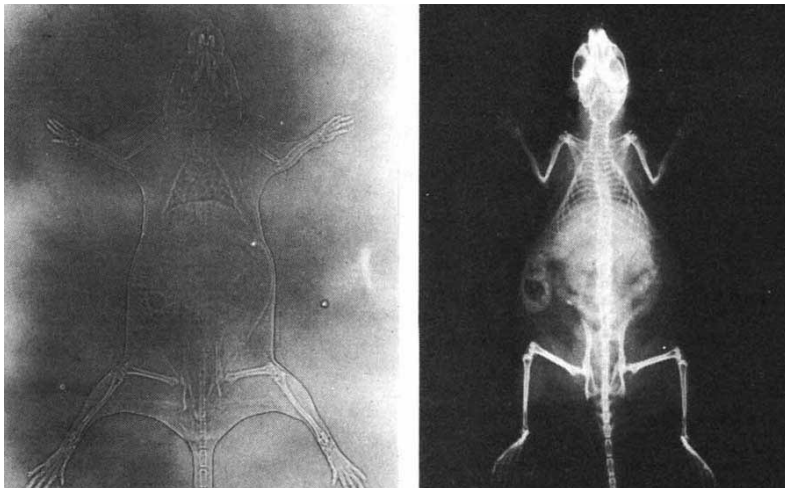

Figure 2.1: (*a*)Proton radiograph of a mouse with its feet 2.5 cm from the film and its back in contact with the film. (*b*) X-radiograph of the same mouse (22 kV on tungsten). Both *a* and *b* have undergone two reversals in processing and so are of the same shading as the original radiograph. The figure is taken from West and Sherwood (1972).

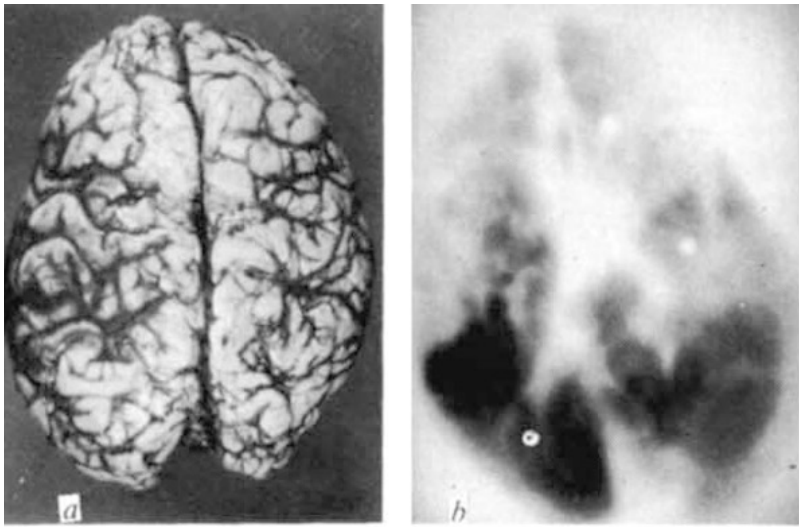

Figure 2.2: (*a*) Photograph of superior view of brain. Note slight discolouration and swelling of left hemisphere which contains the lesion. (b) Proton radiograph (positive) taken through vertical thickness of specimen. Note dense area on left corresponding to intracerebral blood clot. The figure is taken from Steward and Koehler (1973*b*).

2.1.2 Energy-loss based proton imaging

In proton therapy, the incident energy of the protons must be accurately determined such that the Bragg peak is just at the exact position of the tumor volume. This can be achieved by knowing the specific ionization of the tissues along the

beam-line. Since the rate of energy loss, i.e. the stopping power, of protons depends on their energy and the chemical composition in which they are slowing down, then a map of the stopping power can be obtained.

The idea of using the energy-loss of proton beams for imaging was first proposed by Cormack (1963) to reconstruct the stopping power map of the object under the assumption that tissues vary in density rather than in chemical composition. It was not until the late 1970s that pCT was finally carried out at the Harvard cyclotron laboratory (Cormack and Koehler, 1976) following the success of CT reconstructions from measurements obtained at the LBL using alpha particles (Goitein, 1972). Their setup consisted of the 158 MeV external beam, series of brass collimator, a lead scatterer and sodium iodide (NaI) scintillator counters. The phantom was a cylinder made up of Lucite and varying densities of sugar solutions. The reconstructed quantity of interest was the density of the materials in the phantom and a density difference of 0.5% was achieved. Although the quantity of interest for proton therapy is not the density but the stopping power of the material, their calculations of the stopping power from the reconstructed density introduced a doubt which they believed is due to the blurring at the interface of the materials, which, they later call the West-Sherwood effect (West and Sherwood, 1972, 1973). It has been reported that the low doses of protons and heavy ions could already give diagnostically useful images although the amount of information it could give and its medical interest, in general, has yet to be proven compared with xCT. Following the paper of Steward (1976) on the diagnostic potential of proton and heavy-ion radiography, the interest in proton imaging triggered interest in the medical field and led to establishments of a beam line at the Fermi National Accelerator Laboratory (FNAL) exclusively dedicated to proton radiography studies (Curry and Steward, 1978) with proton energy that could reach 200 MeV (Full-width-at-half-maximum (FWHM) beam spread of less than 3.61 MeV) and fluence rates from 2×10^3 to 2×10^5 protons/cm^2 over a 28-cm diameter field.

Proton CT experiments were also carried out at the Los Alamos Meson Physics Facility (LAMPF) (Hanson et al., 1978; Hanson, 1979; Hanson et al., 1981). Their experimental setup consisted of a proton source that could reach as high as 240 MeV, a hyperpure germanium detector (HPGe) to measure the exit energy, multiwire proportional chamber (MWPC) as position detectors and scintillation counters to trigger the data acquisition system. The residual energy and exit position were recorded on a magnetic tape for off-line analysis. Tracking of the exit position and angle of each proton was performed and appropriate cuts were carried out inspired by other charged particle radiography experiments, e.g. alpha particles/helium ions (Huesman et al., 1975; Crowe et al., 1975) performed at the LBL. A 2D image was reconstructed using Filtered back-projections (FBP) using SLPs. Although the use of a curved proton path during reconstruction was already considered, it was not yet implemented. Hanson et al. (1978) pointed out that aside from eliminating the beam hardening artifact encountered in xCT scans, pCT has a significant dose advantage with respect to xCT when imaging with tissues. Calculations on the dose advantage were performed to compare the proton and x-ray doses required to produce reconstructions with identical density resolution and it has been reported that protons could provide the same density resolution as monochromatic x-rays with a reduction of the surface dose by a factor of 3.9 for a 20 cm diameter specimen. The

poor spatial resolution of proton images which is due to the MCS as observed by early pRG and pCT images limits the full potential of the new method and suggested that the use of heavy ions may reduce the scattering effects on the images. Proton CT experiments were eventually carried out using fresh human tissues including scans of brain specimen and adult heart specimen with myocardial infarction (Hanson et al., 1982).

2.1.3 Nuclear scattering based proton imaging

Protons not only undergo multiple scattering but also nuclear elastic scattering when traversing tissues. Saudinos et al. (1975) first demonstrate the possibility of using the nuclear scattering of 500-1000 MeV protons to directly obtain a three-dimensional map of the relative hydrogen concentrations of a specimen. The trajectory of the incident and scattered protons were determined using scintillation detectors to trace the vertex of the interaction and from this, the hydrogen content was inferred. In their experiments, a 540 MeV proton beam was used to irradiate two eggs, one hard-boiled and one incubated. Since fat has a higher percentage of heavy nuclei, a difference between yolk and albumen could be observed via the nuclear scattering radiography (NSR). It has been reported that a voxel size of about 1 mm^3 is achievable and their preliminary measurements gave a volume resolution of 10 mm^3 even with an incomplete setup. Further work at the European Organization for Nuclear Research (CERN) (Charpak et al., 1976) using a 600 MeV proton beams incident onto carbon, paraffin and water phantoms demonstrate a resolution of 2 mm^3. Measurements on test animals were even carried out but the resolution was limited to 43 mm^3 due to low statistics. Tomographic reconstructions were eventually carried out in Saclay, France (Berger et al., 1978) on a skull, with a brain, a sphenoid bone, and a spinal cord and vertebra. The results showed good contrast between the marrow and the bones in a spinal cord as well as correct display of the structure of sphenoid bone. Further work on a human head using 1 GeV protons was also carried out (Duchazeaubeneix, 1980). An interesting aspect of this method is that the incident energy and the range straggling are unimportant because the nuclear cross-section varies only slowly with the incident proton energy. Although, there is a clear proof of principle of the method and possible applications in medical imaging as this could be a key to differentiate the chemical composition of a specimen, however, due to the scarcity of high-energy proton accelerators and the limit imposed on the data by the speed of the acquisition from the detector system, this method has not been further explored. The results were promising but the practical use of the method is limited by the need of a big accelerator to produce the 1 GeV proton beam (Saudinos, 1987).

2.2 Clinical rationale

Further work on proton imaging became stagnant after the gain in interest of x-ray imaging for diagnosis especially with the advent of low-dose CT. If the only advantage of the proton technique is better dose, then the extra cost of building such facility does not justify its clinical advantage. Although studies on proton

accelerator and detector designs that could cater to the demands of proton imaging were already considered (Martin et al., 1975; Moffett et al., 1975), however, its potential for treatment planning in proton therapy did not show sufficient grounds for clinical application. It was not until the beginning of the 1990s, spurred by the growing interest in proton therapy, that the need for a precise treatment plan, which involves range verification and patient positioning, triggered a strong desire to improve pRG and pCT for use in clinical practice. Because of the demands for accurate dosimetry, research work on proton imaging has been focused on exploiting the energy-loss technique.

Schneider and Pedroni (1995) conducted quantitative evaluation of the uncertainties in the treatment planning at the Paul Scherrer Institute (PSI), Switzerland by performing test on animal patients. They have found out that there are inaccuracies in the treatment planning as a result of the incomplete modeling of the MCS effects and the systematic errors in proton stopping powers derived from xCT scans which could result in sizable deviations in predicted versus measured proton dose distributions. This daunting task in treatment planning, among others, urged scientists to reinvestigate the potential of proton radiography as a quality assurance tool for proton treatment planning. Proton CT experiments were carried out using a 590-MeV proton beam (degraded to 219 MeV). The individual protons were first tracked before and after the scanned object using MWPCs and then stopped using an NaI detector (with plastic scintillator as a trigger) which measured their residual energies. The spatial information of the two wire chambers was used to reconstruct the most likely trajectory of the proton within the object using the formalism they derived (Schneider and Pedroni, 1994) as opposed to previous pCT reconstructions with SLPs. Aside from individual proton tracking before and after the object, they also demonstrated that radiographic projections acquired from the average exit range and energy-loss plotted against the transverse x and y coordinates of the entrance detector improved significantly the spatial resolution of the pCT image compared with using the data of the coordinates at the exit detector. Although individual proton tracking both at the entrance and exit detector yielded the best spatial resolution so far, the method was still limited to the low proton rate, i.e. 1000 protons per second, which was attributed to three factors: (1) slow movement of the range shifter (100 ms); (2) difficulty of the NaI crystal to operate at MHz event rates and; (3) slow data transfer (1kHz). In 1999, the PSI group improved their setup for fast in vivo radiography (Pemler et al., 1999). They used scintillating fiber hodoscopes and plastic scintillator range telescope to detect the position and range of 10^6 proton/s as single coincidence events. The accuracy of their residual-range images was $\sim$1 mm and the precision is 0.3% for the 200 protons/mm^2.

In 2000, Zygmanski et al. (2000) published a paper on pCT experiments carried out at the MGH, USA. Their pCT setup was designed such that projection data are acquired at a significantly reduced time for in vivo measurements. The new setup included a cone-beam source instead of the traditional CT fan-beam and energy modulation techniques to produce a uniform dose versus depth. Since their system was unable to measure the exit angle of the individual protons, and thus, the West-Sherwood effect which is characterized by the sharp positive and negative spikes along the boundaries was apparent. Efforts were made to partially correct this artifact by redistributing the signal from the external to internal regions such

that the overall area under the signal distribution is conserved by a power-law. The localization of the artifacts in the image can then be done by filtering the image with gradient filters. This correction technique considerably reduced the MCS edge effect at the air-phantom interface from 200% to 25%. Proton CT images were then reconstructed using the Feldkamp-Davis-Kress (FDK) (Feldkamp et al., 1984) and the spatial resolution was reported to be 0.5 line pairs/cm. It has been suggested that methods of deconvolution which could improve pCT reconstructions with MCS corrections could be applied similar to what is done in single-photon emission computed tomography (SPECT) (Frey and Tsui, 1993, 1994).

Following the opening of the Proton Treatment Center at the LLUMC in the beginning of the 1990s (Slater et al., 1992), another pCT collaboration emerged between the LLUMC and the Santa Cruz Institute of Particle Physics (SCIPP)-University of California Santa Cruz (UCSC) (Johnson et al., 2003; Sadrozinski et al., 2003). The group considered semiconductor technology (Keeney et al., 2002), i.e. silicon strip detector (SiSD) to measure the position and energy of the individual protons traversing a hollow aluminum cylinder. The use of GEANT4 for MC simulations on proton imaging was also carried out. A significant improvement of the spatial resolution has been observed when the exit angles were also recorded and angular cuts were implemented. Further studies were carried out including quantification of the trade-offs and scaling between dose, spatial resolution, density resolution and voxel size in an idealized pCT system (Satogata et al., 2003). The group then proposed a conceptual design of a pCT system that meets certain safety and practical constraints for applications in proton therapy (Schulte et al., 2004) as summarized in Table 2.1. They also demonstrated that measurements of the exit angles of the individual protons and the application of selection filter/cuts based on a criterion determined from their MC simulations significantly improved the edge profile of the pCT images compared with those without filters on the exit angles.

In 2004, the PSI group published the first proton radiograph of a live canine patient that previously received proton therapy for a nasal tumor (Schneider et al., 2004). The proton radiograph, acquired with 214 MeV incident protons and single tracking of protons, was reported to have a spatial resolution of $\sim$1 mm. The 0.03 mGy dose received by the canine during exposure was a factor of 50-100 smaller than for a comparable x-ray image.

2.3 State of the art

Data acquisition in energy-loss based proton imaging can be carried out in two ways: (1) integrating and (2) single-tracking. The proton integrating method only involves a detector, a RERD, downstream the patient wherein the resulted signal per pixel is then calibrated to WEPL. The proton integrating approach has been investigated in (Rinaldi, 2011; Seco and Depauw, 2011; Krah et al., 2015). On the other hand, in single tracking systems, aside from the RERD, two PSDs located before and after the object are used to measure the position and direction of each proton.

A significant increase of publications appeared in the literature as a result of the emergence of pRG/pCT groups worldwide. This section presents the status of

Table 2.1: Design specifications for a pCT scanner for therapeutic applications. Table taken from (Schulte et al., 2004).

Category	**Parameter**	**Value**
Proton source	Energy	$\sim$ 200 MeV (head) $\sim$ 250 MeV (trunk)
	Energy spread	$\sim$ 0.1%
	Beam intensity	10^3 - 10^5 protons/sec
Accuracy	Spatial resolution	$<$ 1 mm
	Electron density resolution	$<$ 1%
Time Efficiency	Installation time	$<$ 10 min
	Data acquisition time	$<$ 5 min
	Reconstruction time	$<$ 15 min (treatment planning) $<$ 5 min (verification)
Reliability	Detector radiation hardness	$>$ 1000 Gy
	Measurement stability	$<$ 1%
Safety	Maximum dose per scan	$<$ 5 cGy
	Minimum distance to the patient	10 cm

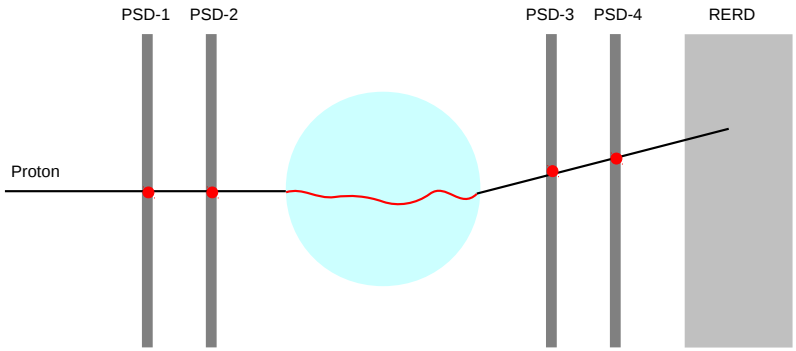

Figure 2.3: A schematic of the ideal proton-tracking proton radiography/proton CT system. PSD, position-sensitive detector; RERD, residual energy-range detector.

the different groups in terms of their hardware development and also reconstruction techniques to improve the accuracy and precision of pRG/pCT images carried out in the past 10 years.

2.3.1 Hardware

Table 2.2 shows a summary of Poludniowski et al. (2015) on the recent hardware developments of the different pRG/pCT groups. Figure 2.3 shows a schematic diagram of a pCT system proposed by LLU/UCSC/Northern Illinois University (NIU) based on proton-tracking of individual protons. The setup consisted of a proton

source, two sets of PSD located before and after the phantom and a RERD. Their prototype was completed in 2010 and the first results were presented with 1% accuracy after using the MLPs (Penfold et al., 2010; Hurley et al., 2012).

In 2007, the Italian project PRoton IMAging (PRIMA), became operational aiming at developing hardware and software techniques (Cirrone et al., 2007; Menichelli et al., 2010; Talamonti et al., 2010; Cirrone et al., 2011; Talamonti et al., 2012; Civinini et al., 2013; Scaringella et al., 2013; Vanzi et al., 2013; Civinini et al., 2010; Lo Presti et al., 2014). Their pCT setup was similar to the LLU/UCSC/NIU design, with PSDs based on SiSDs and a YAG:Ce crystal calorimeter for energy detection with the aim to detect protons with a ∼1 MHz particle rate in the range of 250 MeV to 270 MeV.

Another group in Italy, under the TERA Foundation, obtained a funding from the Centro Nazionale di Adroterapia Oncologica (CNAO) to develop a series of devices for a project entitled Advanced Quality Assurance (AQUA) (Amaldi et al., 2011; Bucciantonio et al., 2013). Their approach is proton range radiography rather than tomography. They used a pair of gas electron multiplier (GEM) PSDs and a scintillator stack to measure the residual proton range after crossing a target.

The PRaVDA Consortium, developed a very different alternative of using radiation-hard complementary metal oxide semi-conductor active pixel sensor (CMOS APS) technology for proton-counting and tracking applications (Poludniowski, Allinson, Anaxagoras, Esposito, Green, Manolopoulos, Nieto-Camero, Parker, Price and Evans, 2014; Esposito et al., 2015; Price et al., 2015; Taylor et al., 2015, 2016). The PRaVDA Range Telescope (RT), uses a stack of 24 CMOS APS to measure the residual proton energy after the patient.

Construction of a pCT system is also carried out at the Niigata University, Japan, with beam test performed at the HIMAC of National Institute of Radiological Sciences (NIRS) (Saraya et al., 2014). They developed a prototype system for pCT with SiSDs and performed a beam test for imaging. A spatial resolution of 0.45 mm was achieved for a 25-mm-thick polyethylene object.

Various detectors were proposed to achieve the optimal resolution for position and energy detection. Seco et al. (2014) presented a comprehensive review on the characteristic of radiation detectors for dosimetry and imaging. The following are the different detector candidates for RERDs and PSDs investigated by the different groups both for pRG and pCT applications using either integrating or single-tracking approach.

Position sensitive detectors (PSDs)

Candidates for PSDs include SiSDs, plastic scintillators and nuclear emulsion films. The use of SiSDs as position trackers, despite the relatively high cost per area compared with plastic scintillators, are favorable because of its high efficiency and low noise. Although the use of SiSDs have been the popular choice, nuclear emulsion film detectors (interleaved with tissue equivalent absorbers) to measure the position and residual range of protons can also be an alternative (Braccini et al., 2010). Nuclear emulsion film detectors consist of a gel with silver bromide (AgBr) crystals where a latent track is formed after the passage of an ionizing particle. Tracks can

Table 2.2: A summary of current and recent proton radiography pRG/pCT prototypes. Table updated from (Poludniowski et al., 2015).

Group	Year of Reference	Area (cm^2)	Position-sensitive detector technology (number of units)	Residual energy-range detector technology	Proton rate (Hz)	pCT or pRG
PSI	2005	22.0 × 3.20	x-y scintillating fiber hodoscope (Sci-Fi) (2)	Plastic scintillator telescope	1 M[a]	pRG
LLU/UCSC/NIU - Phase 1	2013	17.4 × 9.00	x-y SiSDs (4) (80 μm)	cesium iodide (CsI) (Tl) calorimeters	15 k[a]	pCT
LLU/UCSC/California State University, San Bernadino (CSUSB) - - Phase 2	2016; 2016	36.0 × 9.00	x-y SiSDs (66 μm) (4)	Plastic scintillator hybrid telescope (1%)	2 M[a]	pCT
AQUA	2013	30.0 × 30.0	x-y GEMs (2)	Plastic scintillator telescope	1 M[a]	pRG
PRIMA I	2014	5.10 × 5.10	x-y SiSDs (4)	YAG : Ce calorimeters	10 k[a]	pCT
PRIMA II	2014	20.0 × 5.00	x-y SiSDs (4)	YAG : Ce calorimeters	1M	pCT
Istituto Nazionale di Fisica Nucleare (INFN)	2014	30.0 × 30.0	x-y Sci-Fi (4)	x-y Sci-Fi	1M	pCT
NIU/FNAL/Delhi	2016	22.0 × 10.0	x-y Sci-Fi (4)(0.27 mm)	Plastic scintillator telescope	2M	pCT
Niigata University	2014	9.00 × 9.00	x-y SiSDs (4)	NaI(Tl) calorimeter	30 k[a]	pCT
Proton Radiotherapy Verification and Dosimetry Applications (PRaVDA)	2016	9.30 × 9.60	x-u-v SiSDs (4)	5.0x10.0 cm2CMOS APS telescope	1M	pCT
KVI-Center for Advanced Radiation Technology (KVI-CART)	2016	3.00 × 3.00 (downstream) and 10.0 × 10.0 (upstream)	GridPix-based gas-filled time projection chambers (TPCs) (2)		BaF_2 crystal	pRG
Japanese Group-Hiroshima	2016			20.0 × 20.0 × 5.00 cm^3 plastic scintillator + CCD camera		pCT

The reference for each system corresponds to the most recent publication for the system in question.
The designation of pCT or pRG indicates whether the initial stated aims include pCT.
[a]Quoted figure (or a value close to it) has been experimentally demonstrated.

be visualized and analyzed by optical microscopes. Gas electron multiplier (GEM) is also a candidate as trackers because it is relatively inexpensive, easily expandable to large surface coverage and with low mass compared with solid-state trackers.

Residual energy-range detectors (RERDs)

In energy-loss based proton imaging, the difference between the incident energy and the measured residual energy after passing through a material is converted to WEPL. There are two ways to obtain the WEPL: (1) by measuring the residual WEPL with a range counter; and (2) by calculations from proton residual energy detected by a calorimeter. A range counter usually consists of a stack of thin plastic

scintillators. The scintillation light produced is directed to a silicon photomultiplier (SiPM) and is read-out by a wavelength shifting fiber (WLSF). The last downstream tile determines the water equivalent range of each proton. The WEPL can then be calculated from the range measurements with and without the object. A direct readout using SiPMs is also possible, however, this approach is sensitive to noise and temperature. With a calorimeter, the proton is stopped by the crystals and the WEPL is derived from the calibrated response of the device. The RERD design of the second generation pCT scanner of the LLU/UCSC/CSUSB group is a hybrid between a range counter and a calorimeter. It is made up of multi-stage scintillators. The range is determined by the position of the last stage where a response is detected and additionally, the residual energy is determined by the response of the scintillator.

The precision in energy-loss based pCT images relies heavily on the resolution of the energy detector. Moreover, even with perfect detectors, the precision is influenced by energy straggling of the protons in the material and is improved by increasing the number of incident protons, i.e. the dose to the patient (Sadrozinski et al., 2004). Schulte et al. (2005) quantified the relationship of the noise-dose to the patient and presented good trade-offs for optimal pCT.

2.3.2 Software

Due to the complex nature of proton interactions, proton imaging requires different approaches in terms of data processing and image reconstruction compared with the conventional xCT. In general, pCT software development revolves around improving the accuracy and the spatial resolution of the images. This involves precise data selection and proton path estimate coupled with a fast and reliable data processing and reconstruction algorithm. The parameters that will be discussed in the following subsections are applicable for the single proton tracking method and may in some way or another applicable as well with the proton integrating method.

Data selection

Data selection of the detected protons depends mainly on the inverse problem or the reconstruction model used. In energy-loss based pCT, data selection that meets the assumption of Bethe's equation is required. This means that only *primaries* without any nuclear interaction should be considered. In practice, tracking down the interactions of the individual *primaries* and *secondaries* is impossible to achieve. The role of MC simulations using softwares like GEANT4 in determining the behavior and the statistics of the *primaries* and *secondaries* had been an indispensable tool in pCT data processing. Standard routine is based on 3-σ cuts (Schulte et al., 2008) on the angular and energy distributions per pixel to filter out the *secondaries* and *primaries* with elastic nuclear interactions. This criteria is, however, based on the assumption of a homogeneous water cylinder at a specific incident energy and material thickness. The robustness of this method and its effect on the accuracy of the pCT images have yet to be investigated.

Proton path estimates

Different path estimates have been proposed to model the stochastic nature of proton propagation in a material. These path estimates are straight-line path (SLP), most-likely path (MLP) and cubic-spline path (CSP).

The classic SLP is the easiest and computationally, the fastest among the three path estimates. This method is achieved by determining only the exit position of the proton and doing backprojections in a straight line towards the entrance position. Most photon based imaging are SLP-based because, in principle, photons are not deflected by the atomic electrons of the medium. However, it is a different case with protons, which undergo several collisions and deflections by the electrons and the nucleus.

To address this, a curved proton path, also called MLP, was also proposed which is based on formalisms that minimizes the path estimate error after imposing some boundary conditions. Williams (2004) presented an MLP formalism using a Gaussian approximation of MCS and a χ^2 formalism incorporating the effect of continuous energy loss and when the entrance and exit positions and angles are known. The results show that the MLP predicts the true path to better than 1 mm. This implies that pCT reconstructions using the MLP should have at least 1 mm pixel size to have good accuracy. A drawback of Williams (2004) formalism is that it cannot be directly applied to cases in which only entry and exit location but not direction is available. Schulte et al. (2008) derived an improved, matrix-based MLP that is reported to track 200 MeV protons within 0.6 mm on average when employing the 3-σ cuts on relative exit energy and exit angle to eliminate the majority of events not conforming to the Gaussian model of MCS used in the MLP derivation. Erdelyi (2009) further carried out an MLP formalism using functional analysis method based on Lagrange multiplier to constrain the MLP on the exit energies. Another approach is to use the probability envelope map MLP (Wang et al., 2010). The performance of the MLP in pCT reconstructions were investigated in (Li and Liang, 2004; Li et al., 2006).

Due to the computational demands of MLP, an alternative is to use a spline estimate, also known as CSP. The CSP was found to demonstrate good performance but with significantly faster convergence time than the MLP estimate. The CSP proposed by earlier studies only takes into account the position and direction of the incoming and exiting protons. A recent improvement is carried out by further optimizing the proton path with the energy-loss information of the protons, thus, improving the spatial resolution of the pCT images (Collins Fekete et al., 2015).

The curved path estimates demonstrate the best performance, however, the models are still incomplete because the heterogeneities of the human body were not accounted for. Wong et al. (2009) characterized the systematic errors that are introduced by regions of bone and air density and how this affects the accuracy of pCT in surrounding voxel both in terms of spatial and density reconstruction accuracy as well as the performance of the different path estimates, e.g. SLP and CSP (Li et al., 2006; Wang et al., 2011). It has been demonstrated that SLP provide the fastest computational speed but with worst resolution.

Data processing and reconstruction algorithms

While there have been significant improvements in pCT, our group at Centre de Recherche en Acquisition et Traitement de l'Image pour la Santé (CREATIS) (Lyon, France) in collaboration with the Institut de Physique Nucleaire (IPNL) (Lyon, France) and the Ludwig Maximilians University (LMU) (Munich, Germany), focused on the improvement of the accuracy and precision as well as the spatial resolution of pCT images. Research activities started in 2012 and Rit et al. (2013) first demonstrated the feasibility of using the MLP on FBP using distance-driven projections. The details of this method will be presented in chapter 4. Quantitative MC evaluations on the advantages of pCT over xCT in the estimate of proton range has also been carried out by Arbor et al. (2015). An improved backprojection-then-filtering (BPF) based on the two-step Hilbert transform to reconstruct proton CT images has also been proposed by Rit et al. (2015).

Image reconstruction algorithms can be performed either by an analytical method or an iterative method. Reconstructions with SLPs are usually carried out using an analytical method, particularly, the FBP. A novel approach to pCT reconstruction using BPF is proposed by Poludniowski, Allinson and Evans (2014). This method is however limited to back-projections along a straight path, and so, with the introduction of a curved MLP or CSP during reconstruction, an iterative technique became the means of reconstruction modality. Iterative algorithms based on algebraic reconstruction technique (ART) have been proposed (Penfold and Censor, 2015) and implemented (Bruzzi et al., 2016). **?** compared the image quality of proton/ion CT with respect to particle therapy, taking into account different reconstruction methods.

Hybrid proton imaging methods

The finite range of about 33 cm of water of most commercial proton therapy systems limits the sites that can be scanned from a full 360° rotation. A new technique converting megavoltage x-ray projections into virtual proton projections using existing relations of proton projections and multispectral megavoltage x-ray projections for human tissue has also been carried out by Wang et al. (2012). The converted virtual projections demonstrate an uncertainty of ±0.8% compared with the ground truth while the reconstructed images had an uncertainty of ± 1.1%. If these images are used for treatment planning, the average proton range uncertainty is estimated to be less than 1.5% for an imaging dose in the mGy range. Converted proton projections can be blended with existing proton projections. Hansen et al. (2014) also proposed a similar method to overcome the problem using a dual modality reconstruction (DMR) combining the proton data with a cone-beam x-ray.

2.4 Summary and conclusion

The chapter presented the developments in proton imaging. In the medical context, proton imaging is driven by the demands to improve the estimate of the RSP maps. Most efforts in proton imaging have been directed towards the improvement

of the accuracy and precision of the energy-loss based imaging method to reconstruct the RSP map of the material. Several hardware technologies have also been proposed to meet the demands of the imaging method considered. Aside from energy-loss, the other imaging methods, like attenuation and scattering could also give information about the material. The objective of this thesis is to investigate these other proton imaging modalities for possible applications in proton therapy.

Chapter 3

Physics of proton interactions in matter

Contents

A proton is a subatomic particle with a positive charge and usually denoted with symbol p or p^+ or even H^+. Proton interaction in matter are of two types: electromagnetic and nuclear.

3.1 Electromagnetic interactions

When a charged particle, such as a proton, traverses matter, it interacts with the electrons of the medium causing the slowing down and small-angle scattering of the protons.

3.1.1 Mean energy loss

The rate at which a proton loses energy in a material, i.e. the stopping power S, increases as the proton slows down and depends on the kinetic energy and the stopping material. The stopping power S of a material is defined for the ensemble of particles/beam rather than for the individual particle. In many applications or experiments involving protons, the rate of energy loss, $\mathrm{d}E$ per unit length $\mathrm{d}x$, is expressed such that it is independent of the mass density ρ, hence, the mass stopping power S/ρ is defined by,

$$\frac{S}{\rho} = -\frac{\mathrm{d}E}{\rho \mathrm{d}x} \tag{3.1}$$

Bethe (1930) derived a formula describing the energy loss of charged particles in a medium and later, Bloch (1933) included a correction for the quantum mechanical

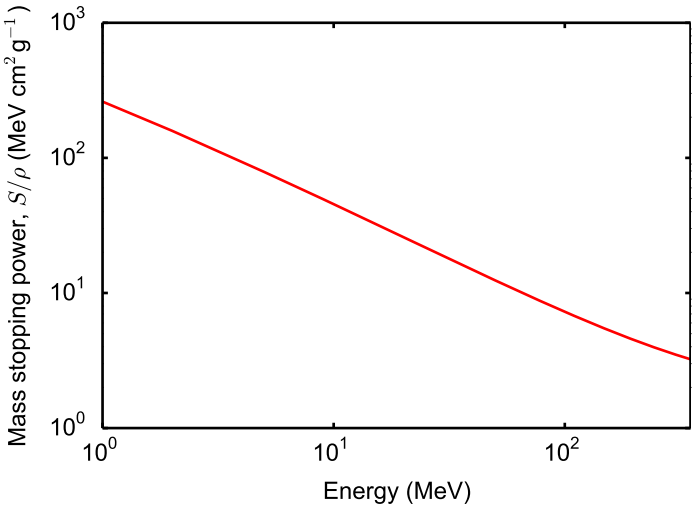

Figure 3.1: NIST/GEANT4 data of the total proton mass stopping power S/ρ as a function of energy in water.

effects. The Bethe-Bloch equation is given by,

$$\frac{S}{\rho} = -\frac{\mathrm{d}E}{\rho \mathrm{d}x} = 4\pi N_A r_e^2 m_e c^2 \frac{Z}{A}\frac{z^2}{\beta^2}\left[\ln\frac{2m_e c^2\beta^2}{I(1-\beta^2)} - \beta^2 - \frac{\delta}{2} - \frac{C}{Z}\right] \tag{3.2}$$

where N_A is the Avogadro's number, r_e is the classical electron radius, m_e is the mass of an electron, z is the charge of the projectile, Z is the atomic number of the absorbing material, A is the atomic weight of the absorbing material, c is the speed of light in vacuum, $\beta = v/c$ where v is the velocity of the projectile, I is the mean excitation energy of the absorbing material, δ is the density effect corrections due to the shielding of remote electrons by close electrons and will result in reduced energy loss at higher energies, and C/z is the shell correction item to correct for the atomic binding in compounds, which is important only for low energies where the velocity v of the incident particle is close to the velocity of the atomic electrons. Figure 3.1 shows the proton mass stopping power S/ρ in water as a function of energy taken from the NIST/GEANT4 database.

From Equation 3.2, it can be observed that the mass stopping power S/ρ is proportional to Z/A. The ratio Z/A for most elements (except hydrogen) varies around 0.5-0.4. The stopping power S also depends on the I-value of the material which has a dependence on the atomic number Z (Figure 3.2). Because of the logarithmic dependence of the stopping power S with the mean excitation energy I, it is often assumed that the stopping power S varies weakly with the mean excitation energy I. Hence, as stated earlier, in treatment planning protocol, the mean excitation energy I for the different biological tissues is often assumed to be of water, i.e., $I_{material} = I_{water} = 78$ eV. Note, however, that the stopping power S is not dependent on the mass of the projectile, it rather depends on the square of the charge ($z = 1$ for proton). Although it depends on the inverse square of the velocity, the dependence is also weak. Therefore, the stopping power S is most strongly dependent on the electron density ρ_e of the material.

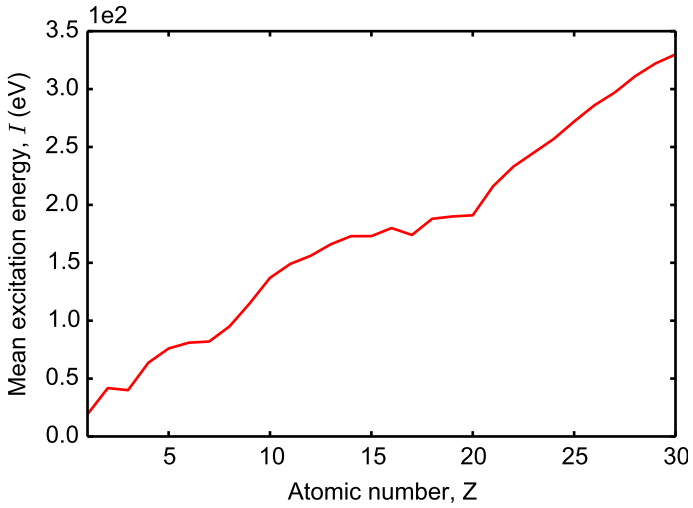

Figure 3.2: GEANT4 data of the mean excitation energy I as a function of the atomic number Z.

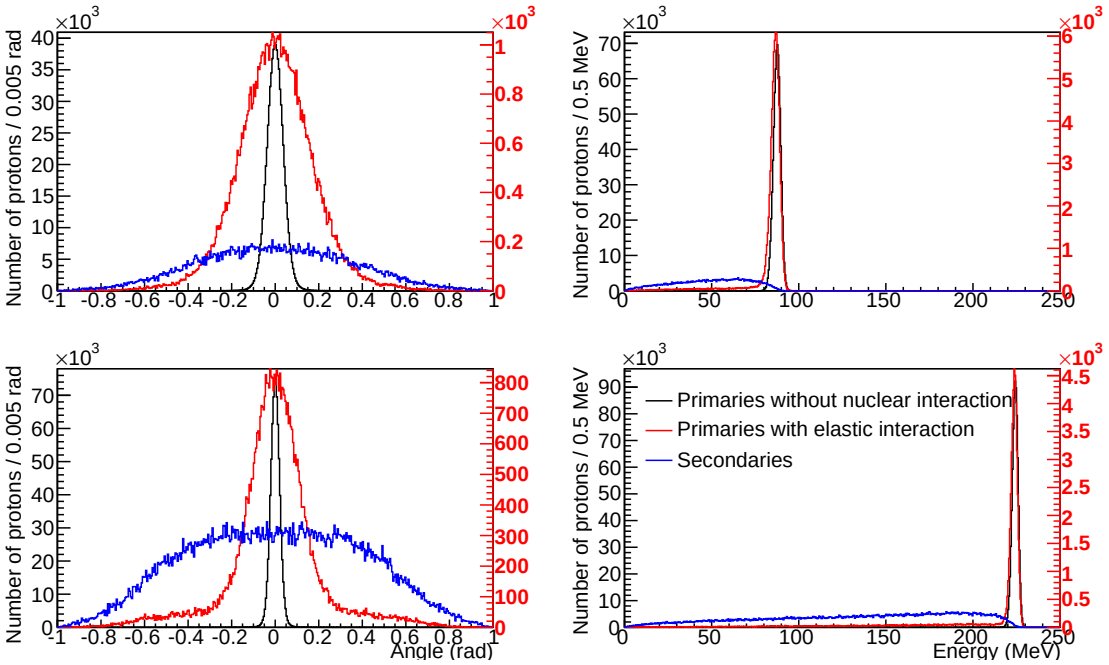

Figure 3.3: Exit angular distributions (left) and energy distributions (right) for 200 MeV (top) and 300 MeV (bottom) pencil beams. The ordinates are the number of exit protons traversing the water box ($20\times20\times20$ cm^3) for 1 million incident protons. The left scales are for *primaries* without nuclear interactions only (black curves) while the right scales are for the rest of the protons (red and blue curves).

3.1.2 Energy-loss straggling

As mentioned earlier, the stopping power S is a measure of the mean stopping power of a beam. This is because, even though a monoenergetic proton beam is incident onto a material, each proton would undergo different atomic collisions.

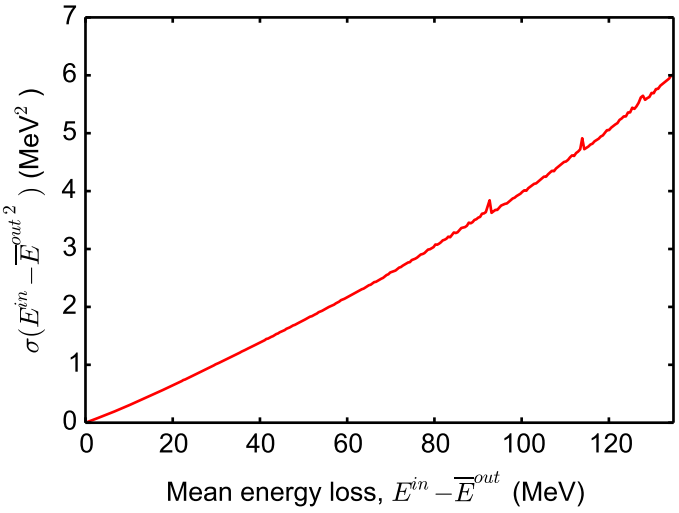

Figure 3.4: GEANT4 simulation of the variance of the mean energy loss $\sigma(E^{in} - E^{out})^2$ as a function of mean relative energy loss $E^{in} - E^{out}$ for protons in water.

The interaction between the incident protons and the electrons of the target is subject to statistical fluctuations which also results in variations in the amount of energy transferred to the material. This phenomenon is called energy straggling and most evident by the distribution of the energy after traversing the target and also the limiting resolution of energy detectors. The analytical formula to describe the energy straggling is quite complex. Instead, the energy straggling distributions of non-relativistic heavy particles, can be approximated using the theory of Tschalär (1968) as explained by Schulte et al. (2005) which is described by the differential equation:

$$\frac{\mathrm{d}}{\mathrm{d}x}\sigma_T^2(x) = \kappa_2(x) - 2\left(\frac{\mathrm{d}}{\mathrm{d}E}\kappa_1\left(E(x)\right)\right)\sigma_T^2(x) + \text{higher order terms} \tag{3.3}$$

where

$$\kappa_2(x) = \eta_e K \frac{1 - \frac{1}{2}\beta^2(E(E_{in}, x))}{1 - \beta^2(E(E_{in}, x))} \tag{3.4}$$

and $k_1(E(x))$ is the linear stopping power S described by the Bethe formula (Equation 3.2) without the relativistic correction terms. The higher-order terms contain higher-order derivations of k_1 with respect to energy which are small values and can be neglected.

Figure 3.4 shows how the variance of the energy loss varies as a function of the mean relative energy loss. A power law approximation has also been suggested by several authors (Chu et al., 1993; Bortfeld, 1997) to conveniently estimate the σ as a function of the proton beam range. The variance σ can be approximated as a function of the path length of a particle in water (expressed in centimeters) as,

$$\sigma_x \approx 0.012\ R_{water}^{0.935} \tag{3.5}$$

where R_{water} is the range in water or the WEPL.

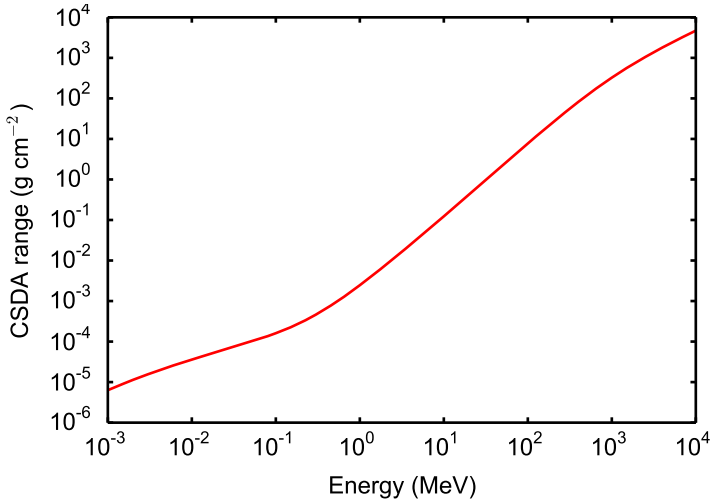

Figure 3.5: Continuous-slowing-down-approximation (CSDA) range of protons in water as a function of energy.

3.1.3 CSDA range

For a single incident proton, the range is defined as the depth where an incident proton with initial energy E_{in} stops in the material, i.e. when its energy decreases to zero. For an ensemble of particles of uniform incident energy, the NIST defines the continuous-slowing-down-approximation (CSDA) range R as the approximation to the average path length traveled by a charged particle as it slows down to rest, calculated in the continuous-slowing-down approximation. In this approximation, the rate of energy loss at every point along the track is assumed to be equal to the total stopping power. The CSDA range of an individual particle can be calculated from the rate of energy loss by,

$$R(E_{in}) = \int_0^{E_{in}} \left(\frac{\mathrm{d}E}{\mathrm{d}x}\right)^{-1} \mathrm{d}E \tag{3.6}$$

where x is the current position of the particle. The range in Equation 3.6 also approximates the WEPL, which is an important quantity in the clinical environment. Due to the statistical fluctuations in the energy-loss process, the range is also subject to this uncertainty. Therefore, the range usually refers to the average value of the WEPL.

The statistical fluctuations in the energy-loss process results in the dispersion of the path length of a particle beam, i.e. range straggling. Figure 3.5 shows that the logarithm of the range and the logarithm of the energy follows a power law as observed by Bragg and Kleeman (1905). The Bragg-Kleemann rule is defined as

$$R_{CSDA} = \alpha E_{in}^{p} \tag{3.7}$$

where p is a dimensionless quantity and α is a material-dependent constant proportional to the square root of the effective atomic mass of the absorber and inversely proportional to the mass density of the absorber. By performing a least-square fitting of the R_{CSDA}, Bortfeld (1997) obtained $p = 1.77$ and $\alpha = 0.0022$ cm/MeV with an error of 2% if $E_{in} \leq 200$ MeV.

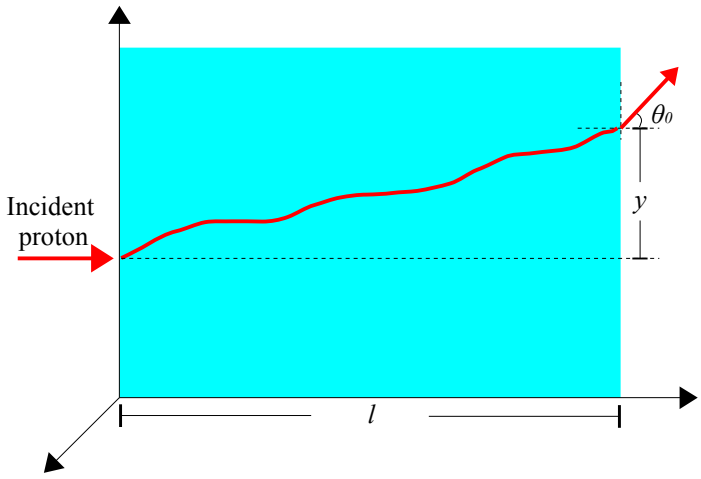

Figure 3.6: Schematic of proton scattering in a material. After traversing a thickness l, The MCS is characterized by an angular deviation θ_0 and lateral displacement y.

3.1.4 Multiple Coulomb scattering (MCS)

The stochastic collision of the primary protons onto the atomic electrons of the material results to multiple deviations from its original direction. The MCS is characterized by an angular deviation and lateral displacement along the beam path as illustrated in Figure 3.6. The theory of the MCS for electrons and charged particles was first developed by Moliere (1948) using a small-angle approximation of the deviation. Several authors attempted to simplify and even improve Moliere's theory for thick materials (Bethe, 1953) and in some way or another created misconceptions in the interpretation. Highland (1975) derived a formula based on Moliere's theory to quantify the scattering angle θ_0 after traversing a slab of thickness l given by,

$$\theta_0 = \frac{14.1 \text{ MeV}}{pv}\sqrt{\frac{l}{X_0}}\left(1 + \frac{1}{9}\log_{10}\frac{l}{X_0}\right) \tag{3.8}$$

where X_0 is the radiation length and p and v are the initial momentum and velocity of the proton respectively. The terms in parentheses are the single scattering corrections in Moliere's theory. Highland assumed a slab that is finite but sufficiently thin that pv does not decrease much ($l \ll$ proton range). Note that Equation 3.8 is already an integral expression and cannot be applied to a thicker slab by reinterpreting l as a step size Δx. Gottschalk (2010) redefined Equation 3.8 for thick slabs by removing the logarithmic term from the sum or integral. The new formula is called the "generalized Highland formula" and is defined as,

$$\theta_{\text{Highland}} = \left(1 + \frac{1}{9}\log_{10}\frac{l}{X_0}\right)\frac{1}{X_0^{1/2}}\left(\int_0^l \left(\frac{14.1 \text{ MeV}}{p(x)v(x)}\right)^2 \mathrm{d}x\right)^{\frac{1}{2}} \tag{3.9}$$

where x is the current position of the proton. Equation 3.9 reduces to Equation 3.8 for thin slabs and was found in agreement with the experimental data and the Moliere/Fano theory (Gottschalk, 2010).

MCS implementation in GEANT4

In GEANT4, particle transport is governed by MC simulations. A step size Δx should be defined at the beginning of the simulation and should be small enough such that Equation 3.8 is valid. Note, however, that GEANT4 uses 13.6 MeV instead of 14.1 MeV which is the accepted value of the 1986 Particle Properties Data Book. It was reported in Grevillot et al. (2010) that the incorrect use of a step size limitation affects the range prediction. This same parameter also affects the scattering angle estimate at the end of the track wherein for thick materials, the sum of the discrete θ_0s then defines the angular scattering after traversing a thickness l. This scheme poses a limitation because the step size Δx is not well established and could bias the estimate after traversing very thick and even dense materials.

Scattering power

To address the step size dependence, Gottschalk (2010) proposed to use a scattering power T which is defined as the rate of change of the mean squared projected MCS angle $A = \langle\theta^2\rangle$ for a given depth x, hence,

$$T \equiv \frac{\mathrm{d}\langle\theta^2\rangle}{\mathrm{d}x} = \frac{\mathrm{d}A}{\mathrm{d}x} \tag{3.10}$$

For a sufficiently thin single slab, pv does not change much, thus,

$$A = \langle\theta^2\rangle = \int_0^l T(x)\mathrm{d}x \tag{3.11}$$

Note that, for thicker slabs, pv can be related to x as long as we know the range-energy relation in the material. The integral expression in Equation 3.11 is crucial as it depends on the scattering power T which could overestimate or underestimate the angular variance A. The goal is to recover Moliere's scattering angle as a function of depth even with thick materials. Gottschalk (2010) pointed out that:

1. T must take into account the competition between the Gaussian core and the single scattering tail of the angular distribution, which affects the rate of change in the Gaussian width and leads to the single scattering correction.

2. The single scattering correction requires that $T(x)$ should be nonlocal. Aside from the material properties and energy at the point of interest x, $T(x)$ must depend also on how much multiple scattering has already taken place.

With these two conditions, Gottschalk (2010) reviewed three local and two nonlocal formulas of T and from these, the T that is nonlocal was chosen. An improved "differential Moliere" T_{dM} formula was then derived by the following procedure:

1. The numerical derivative of the Moliere/Fano/Hanson $\langle\theta^2\rangle$ was calculated to determine the single scattering correction.

2. The formula T_{IC} (ICRU Report 35) for protons was simplified and a material dependent property, the scattering length X_S, was used.

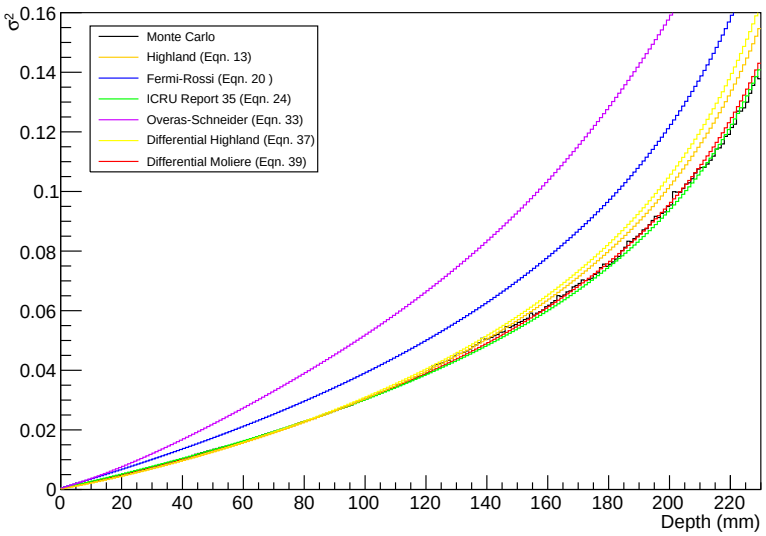

Figure 3.7: The variance of the angular distribution (rad^2) as a function of depth x (mm) in water for 200 MeV incident protons. The theoretical models are found in (Gottschalk, 2010).

3. The T_{dM} was deduced based on the simplifications of the T_{IC} and by including a nonlocal correction factor f_{dM}, which by virtue of the Øverås approximation, parameterizes the single scattering correction.

The T_{dm} is finally defined as,

$$T_{\mathrm{dM}} \equiv f_{\mathrm{dM}}(pv, p_1v_1)\left(\frac{E_S}{pv}\right)^2 \frac{1}{X_S} \tag{3.12}$$

where

$$f_{\mathrm{dM}} \equiv 0.5244 \;+\; 0.1975\log_{10}\left[1-(pv/p_1v_1)^2\right] \;+\; 0.2320\log_{10}(pv) \;-\; 0.0098\log_{10}\left[1-(pv/p_1v_1)^2\right] \tag{3.13}$$

and $E_S = 15.0$ MeV. Figure 3.7 shows a comparison of the different analytical formulas to evaluate the angular variance as a function of depth. The pv term used as an input to the formulas at each depth was obtained using MC simulations. It shows that the T_{dM} and T_{IC} are in good agreement with the MC results.

For MC simulations, the T_{dm} is quite useful as it avoids the step size dependence. Moreover, since the T_{dM} is non-local, it can be used to mixed slabs and could be useful for the analytical dose calculations as incorrect MCS model affects the Bragg peak dose.

3.2 Nuclear interactions

Aside from electromagnetic interactions, protons also undergo interactions with the atomic nuclei of the medium. Nuclear interactions are of two types: *elastic* and *inelastic* (ICRU63). Since both interactions may force the protons to scatter at large angles, they can also be called nuclear scattering. The nuclear cross-sections

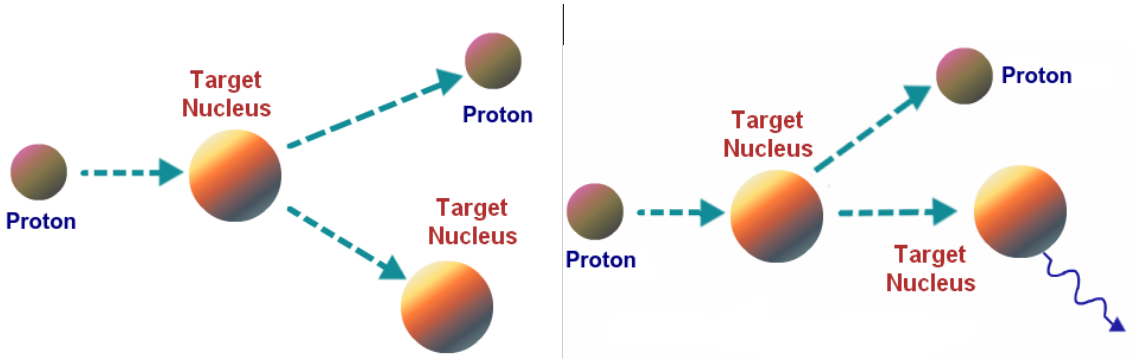

Figure 3.8: Illustration of proton elastic (left) and inelastic interactions (right).

determine the decrease of the fluence of the *primary* protons, i.e. attenuation; the proton range; and the production of secondaries along the beam path in different media.

3.2.1 Elastic

Elastic scattering is a reaction in which the incident projectile scatters off the target nucleus, with the total kinetic energy conserved. This means that the internal state of the target nucleus and of the projectile are unchanged by the reaction. From the nuclear reactions in (Paganetti, 2011), the left column of Figure 3.8 illustrates a proton p having an elastic nuclear interaction with a target nucleus ^{16}O. Thus,

$$p +^{16} O \rightarrow p +^{16} \mathrm{O} \tag{3.14}$$

in which the target ^{16}O remains in the ground state and the total kinetic energy of the system is conserved.

In the case of the human body, some materials, e.g. water, contain free hydrogen. The collision of an impinging proton and a free hydrogen, i.e.

$$p +^{1} H \rightarrow p + p \tag{3.15}$$

yields two protons, approximately in right angles to each other. This kind of nuclear interaction is still elastic because the primary proton merely transferred some of its energy to the target hydrogen nuclei without altering its state in the process. Figure 5.1 shows the total linear elastic nuclear cross-section for selected elements as a function of energy. Figure 3.10 shows the differential elastic cross-section as a function of angle.

3.2.2 Inelastic

On the other hand, *inelastic* scattering occurs when a proton is absorbed and then re-emitted (the target nucleus absorbs some energy internally and is left in an excited state) as illustrated in Figure 3.8 and shown by the following relation:

$$p +^{16} \mathrm{O} \rightarrow p +^{16} \mathrm{O}^{*} \tag{3.16}$$

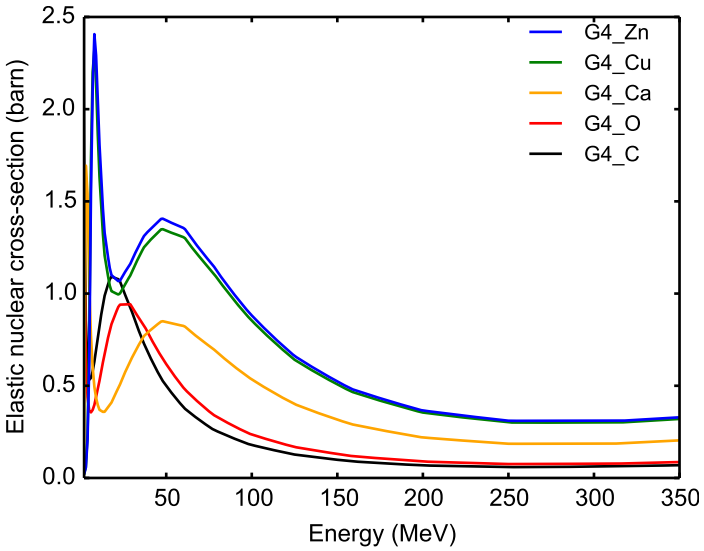

Figure 3.9: GEANT4 data of the *elastic* nuclear cross-section of some elements as a function of energy for proton.

where the symbol * denotes an excited state. The total kinetic energy of the system is not conserved because some of the energy of the incident proton is transferred to the target nucleus, leaving it in the excited state.

A special type of proton inelastic interaction is the quasi-inelastic as shown by the following example:

$$p + {}^{16}O \rightarrow p + p + {}^{15}\mathrm{N} \tag{3.17}$$

This type of reaction is also called nuclear fragmentation. The total kinetic energy of the above interaction is also not conserved because some of the incident proton's energy is used to fragment the target nucleus.

Most of the secondary particles from proton-nucleus collisions are due to inelastic interactions. Possible secondaries in the therapy range include protons, neutrons, γ rays, heavy fragments such as alphas, and recoiling residual nucleus. Unlike electromagnetic interaction of protons, in which the theoretical models are accurate and simple, nuclear interactions on the other hand are complicated and less tested. Different Monte Carlo nuclear models have been evaluated to check their validity for therapeutic applications. A Monte Carlo simulation was carried out by Seltzer (1993) to determine the fraction of energy transferred to secondary particles for a 150 MeV protons onto a ^{16}O target nuclei as shown in Table 3.1. The final energy of incident protons undergoing inelastic nuclear interactions is mostly transferred to protons, neutrons and photons. The production of heavy fragments is not significant, e.g. 2.9% of the total proton energy for alphas, however, these heavy fragments could in principle have a significant relative biological effect (RBE) because of their high-LET (Seltzer, 1993; Paganetti, 2002). This effect is rather small compared with incident carbons ions, whose depth dose profile is characterized by a "train wreck" or nuclear tail at the end of its range.

There have been studies which attempted to quantify the probability of inelastic interactions in matter. For example, Janni (1982) combined theory with experi-

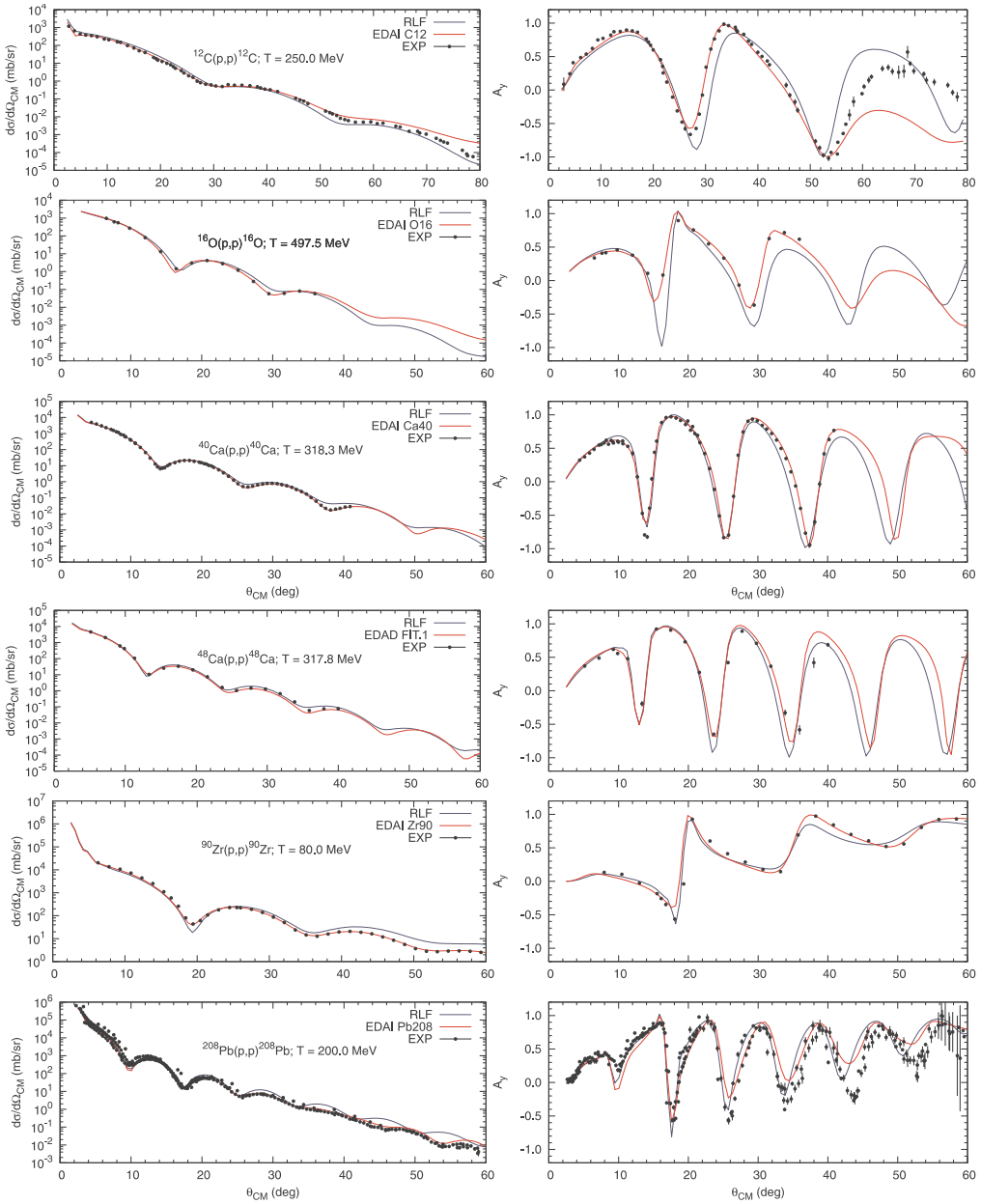

Figure 1. Benchmarking with proton data. The results for the cross sections $d\sigma/d\Omega$ and analyzing power A_y at different energies and nuclei using RLF parametrization (proton and neutron densities of nuclei are obtained within relativistic mean-field theory with NLSH parameters) and "global" Dirac phenomenological optical potential are compared with the experimental data [13].

Figure 3.10: Figure taken from Ivanov et al. (2011).

Table 3.1: The secondary particles in a $p-^{16}$O reaction (Seltzer, 1993).

secondary particle	proton	deuteron	triton	^{3}He	α	Recoils	neutron
fraction of energy	0.57	0.016	0.002	0.002	0.029	0.016	0.20

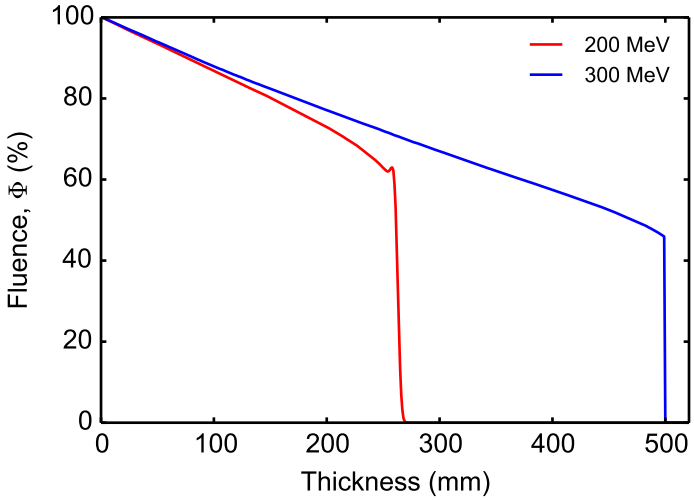

Figure 3.11: Relative fraction of the primary fluence Φ as a function of depth in water for 200 MeV and 300 MeV incident energies simulated using GEANT4/GATE.

mental data to evaluate the proton nuclear inelastic cross-section for various materials while Chadwick (1997) used a slightly different procedure and compared the nuclear cross-section as a function of energy from a different set of experimental data. GEANT4 also use physical models to be used in the simulation. Figure 3.12 shows the nuclear inelastic cross-section of selected elements as a function of energy. It can be observed that a threshold energy around ∼7 MeV is needed to surmount the Coulomb repulsion of the atom. At energy E_{res} around 20 MeV, the inelastic cross-section exhibits a resonance maximum and after that, the inelastic cross-section decreases exponentially. For proton kinetic energies higher than 120 MeV, an asymptotic behavior is reached. These observations are also in agreement with what is observed by (Ulmer and Matsinos, 2012). In the range of energies considered for therapy, i.e. greater than $<$ 250 MeV, the cross-sections for inelastic interactions become nearly independent of energy. At therapeutic energies, the probability is indeed constant. Note, however, that the total interaction probability for a stopping proton is the integral of the inelastic cross section over the range. The gradual decrease of the number of protons as a function of depth is caused by the removal of protons by nuclear reactions. The distal falloff at the end of the range (Figure 1.1) is due to the protons having already exhausted their remaining energy to the absorbing medium.

3.3 Summary and conclusion

The various physical interactions of protons in matter have been explored. In general, protons interact with matter via collisions with the atoms of the medium. The collisions with the atomic electrons result to energy loss and multiple Coulomb scattering while collisions with the nucleus results to elastic scattering and creation of secondaries. Different proton interactions have been modeled with good accuracy and will be the basis to formulate the inverse problems for image reconstructions in

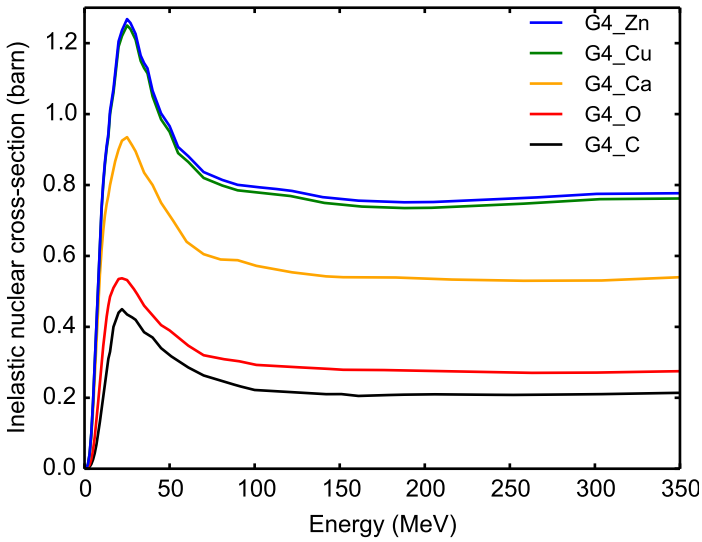

Figure 3.12: GEANT4 data of the *inelastic* nuclear cross-section of some elements as a function of proton energy.

the following chapters.

Chapter 4

Energy-loss proton CT

Contents

This chapter presents the energy-loss pCT method based on the paper of Rit et al. (2013) to reconstruct the RSP-map of the object by measuring the loss of energy of the proton after traversing the object.

4.1 The inverse problem

To derive the inverse problem for energy-loss pCT, we start by considering Bethe's equation (Equation 3.2) to calculate the rate of energy loss $\mathrm{d}E/\mathrm{d}x$ of a proton, i.e. the stopping power S, along the MLP $\mathbf{\Gamma}(w)$, with w the distance from the source. Thus,

$$-\frac{\mathrm{d}E}{\mathrm{d}\mathbf{\Gamma}\left(w\right)}\left(\mathbf{\Gamma}\left(w\right)\right) = S(\mathbf{\Gamma}(w), E(\mathbf{\Gamma}(w))). \tag{4.1}$$

Neglecting Bloch's correction for the density effect and shell corrections is valid because of the relatively small contributions of these terms in the energy range for pCT. Now, from Equation 4.1, the stopping power S can be written as,

$$S(\mathbf{\Gamma}(w), E(\mathbf{\Gamma}(w))) = \rho_e\left(\mathbf{\Gamma}\left(w\right)\right) K \frac{1}{\beta^2(E(\mathbf{\Gamma}(w)))}\left[\ln\left(\frac{2m_e c^2}{I(\mathbf{\Gamma}(w))}\frac{\beta^2(E(\mathbf{\Gamma}(w)))}{1-\beta^2(E(\mathbf{\Gamma}(w)))}\right) - \beta(E(\mathbf{\Gamma}(w)))^2\right] \tag{4.2}$$

where ρ_e is the relative electron density of the material with respect to water, $K = 170$ MeV/cm, m_e is the electron mass and β is the proton velocity relative to the speed of light. By rearranging Equation 4.1, we get,

$$-\mathrm{d}E(\mathbf{\Gamma}(w)) = S(\mathbf{\Gamma}(w), E(\mathbf{\Gamma}(w)))\mathrm{d}\mathbf{\Gamma}\left(w\right). \tag{4.3}$$

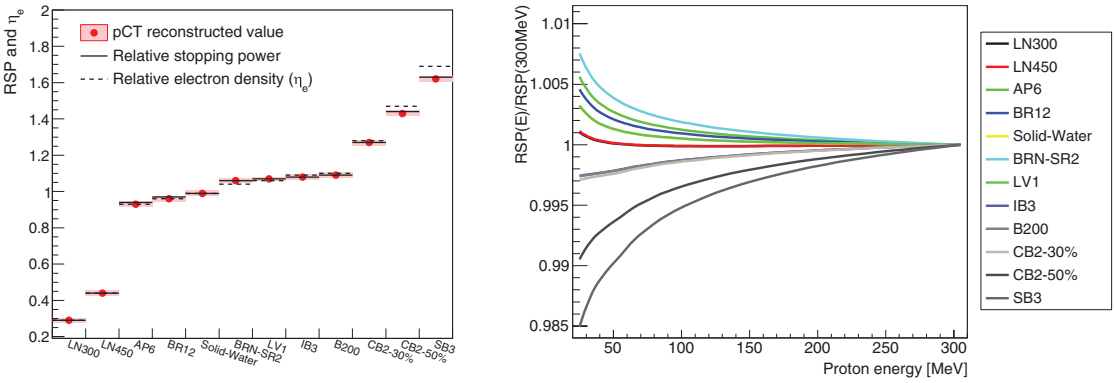

Figure 4.1: Left: reconstructed values of Gammex 467 materials in pCT images compared to theoretical RED and RSP. Right: GEANT4 RSP of Gammex 467 materials, divided by the 300 MeV value, as a function of the proton energy. Figure taken from Arbor et al. (2015).

Dividing both sides of Equation 4.3 with the stopping power of water S_{water}, we get on the right hand side the RSP $= S_{\text{mat}}/S_{\text{water}}$ that should be energy independent for the equation to be valid. It is shown in Figure 4.1 (right) that for a 300 MeV incident energy traversing a 33 cm thick material, the RSP of the material is indeed almost constant as a function of energy, i.e. with <1% variation. We can therefore integrate the material independent left hand side over the energy and the energy independent right hand side over the spatial coordinate. Thus,

$$-\int_{E^{in}}^{E^{out}} \frac{\mathrm{d}E(\mathbf{\Gamma}(w))}{S_{\text{water}}(E(\mathbf{\Gamma}(w)))} = \int_0^l \frac{S(\mathbf{\Gamma}(w), E(\mathbf{\Gamma}(w)))}{S_{\text{water}}(E(\mathbf{\Gamma}(w)))} \mathrm{d}\mathbf{\Gamma}\,(w) \tag{4.4}$$

where S_{water} is the energy dependent stopping power of water, E^{in} and E^{out} are the entrance and exit energies respectively and l is the thickness of the material. Equation 4.4 is, therefore, the inverse problem for energy-loss pCT. Note, however, that the left-hand side of Equation 4.4 is just the energy-loss WEPL.

4.2 The pCT scanner

Figure 4.2 shows the conceptual design of a pCT system for the estimation of the MLP of each proton (Schulte et al., 2003) with the notations used in this manuscript following Rit et al. (2013). A point source with a circular trajectory was used. For a given source position, the 3D coordinate system is represented by the orthonormal basis $\{\boldsymbol{u}, \boldsymbol{v}, \boldsymbol{w}\}$ where $\boldsymbol{u}$ and $\boldsymbol{v}$ define the orientation of the detectors and $\boldsymbol{w}$ defines the source-to-isocenter direction. Let $i \in \boldsymbol{I} \subset \mathbb{R}$ be the index of the tracked protons and E_i^{in} and E_i^{out} are the energies of the proton at the entrance and exit detectors. Following Schulte et al. (2008), the MLP $\mathbf{\Gamma}_i$ of the i-th proton is assumed to be a function of its projection w on the $\boldsymbol{w}$ axis, i.e. $\mathbf{\Gamma}_i(w) \cdot \boldsymbol{w} = w$. A set of two-dimensional (2D) tracking detectors located before and after the object are used to record the entrance $\mathbf{\Gamma}_i(w^{in})$ and exit $\mathbf{\Gamma}_i(w^{out})$ positions of each proton traversing the object with w^{in} and w^{out} the distances of the entrance and exit tracking detectors from the source, respectively. The convex hull of the object is also assumed to be

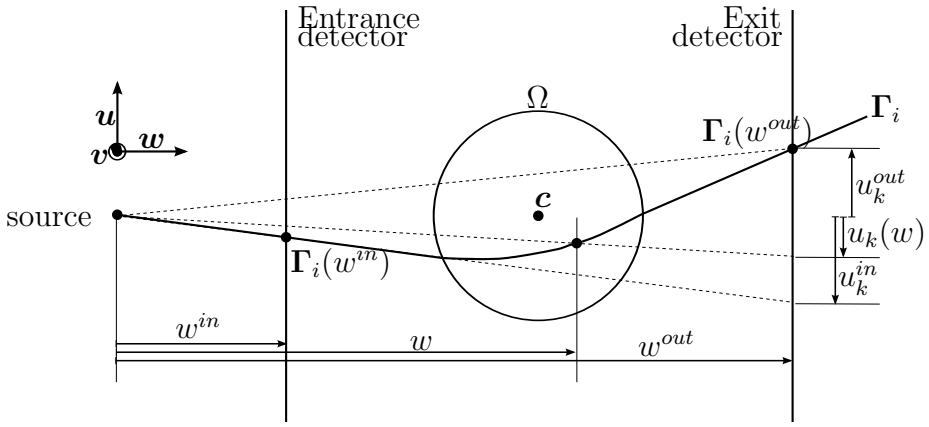

Figure 4.2: Schematic top view of the pCT scanner used in this study.

known and is defined by $\boldsymbol{\Omega}$. Therefore, the MLP of each proton is estimated using $\boldsymbol{\Omega}$, $\boldsymbol{\Gamma}_i(w^{in})$ and $\boldsymbol{\Gamma}_i(w^{out})$.

Introducing $G : \mathbb{R}^2 \to \mathbb{R}$ as the energy integral or energy-loss WEPL, hence, the WEPL integral is rewritten as,

$$G(E_i^{in}, E_i^{out}) = \int_{E_i^{out}}^{E_i^{in}} \frac{\mathrm{d}E}{S_{\mathrm{water}}(E)}. \tag{4.5}$$

4.3 Distance-driven binning

Filtered back-projections (FBP) reconstructions carried out in the past were all based on the use of SLPs to trace the proton trajectory in the material. This limits the use of analytical reconstruction methods for pCT in favor of iterative methods, e.g. algebraic reconstruction technique (ART). However, Rit et al. (2013) demonstrated that curved proton path could be used for FBP by binning the projections at different distances w from the source defined by the curved path estimate. The distance-driven binning technique uses any path estimate, e.g. MLP or CSP, to define the path of the individual proton.

To demonstrate, we first let $\boldsymbol{j} \in \boldsymbol{J} \subset \mathbb{Z}^2$ be a set of spatial indices corresponding to a grid of the virtual proton radiograph and h: $\mathbb{R}^2 \to \mathbb{R}$ the pixel indicators,

$$h_{\boldsymbol{j}}(\boldsymbol{y}) = \begin{cases} 1 & \text{if } \boldsymbol{y} \in \mathbb{R}^2 \text{ is in pixel } \boldsymbol{j}, \\ 0 & \text{otherwise.} \end{cases} \tag{4.6}$$

From these paths, each WEPL G per proton pair is binned in virtual radiographs at different distances w from the source. The final projection values are the average values of the WEPL G per pixel, hence, the distance-driven projection value $g_j^e(w)$ is defined as,

$$g_j^{\mathrm{e}}(w) = \frac{\sum_i h_j\left(u_i\left(w\right), v_i\left(w\right)\right) G(E_i^{in}, E_i^{out})}{\sum_i h_j\left(u_i\left(w\right), v_i\left(w\right)\right)} \tag{4.7}$$

where the superscript e indicates that the projections were derived from energy-loss pCT method.

4.4 Image reconstruction

The distance-driven projection is computed for each source position and reconstruction of the RSP-map is then carried out and in the following chapters using the same reconstruction algorithm as in Rit et al. (2013), i.e. the FDK algorithm (Feldkamp et al., 1984) adapted with a voxel-specific backprojection selecting the distance w according to the distance between the voxel and the exit detector for each source position.

4.5 Statistical limitations

Quantification of the inherent noise in a CT image is important in evaluating the efficiency and usefulness of the image and the method. We first consider a CT image of a homogeneous cylinder where the isocenter of reconstruction is the center $\boldsymbol{c}$. The fluctuations on pixel-by-pixel basis in a CT image is generally caused by two factors: (1) the stochastic fluctuations in the measurement of data and (2) the noise contribution of the reconstruction method used. To put it forward, we let $\sigma_{RSP(\boldsymbol{c})}$ be the CT noise level in the isocenter $\boldsymbol{c}$, and that,

$$\sigma_{RSP(\boldsymbol{c})} = \frac{1}{P}\sum_{p=1}^{P} f\sigma_{g_{\boldsymbol{j}}^{\mathrm{e}}(w^c)} \tag{4.8}$$

where $\sigma_{g_j^{\mathrm{e}}(w^c)}$ is the standard deviation of the center-binned projection value in a single projection p and f is the noise contribution of the filter in the center. For a radially symmetric object whose projections vary slowly in the center $\boldsymbol{c}$ with sampling size a in both $\boldsymbol{u}$ and $\boldsymbol{v}$ directions, the noise contribution of the ramp filter is $f = \pi/\sqrt{12a^2}$ (Gore and Tofts, 1978).

Following the work of Schulte et al. (2005) and also considering a constant incident energy E^{in} throughout the scan and a perfect exit detector, the WEPL $G(E_i^{in}, E_i^{out})$ is only influenced by the straggling of the exit energy E^{out}. Using the first order error propagation to estimate the noise in the estimate of the WEPL $G(E_i^{in}, E_i^{out})$, i.e. σ_G, gives,

$$\sigma^2_{G(w)} = \sigma^2_{E^{out}} \left(\frac{\mathrm{d}G(E)}{\mathrm{d}E}\bigg|_{E=E^{out}} \right)^2 . \tag{4.9}$$

From Equation 4.5, the term in parenthesis is just the square of the inverse of the stopping power of water S_{water} as a function of the exit energy E^{out}, i.e. $S_{\text{water}}(E^{out})^{-2}$. Therefore, an estimate of the noise of a single projection is given by,

$$\sigma_{g_{j,p}^{\mathrm{e}}(w^c)} = \frac{1}{N}\frac{\sigma^2_{E^{out}}}{S_{\text{water}}(E^{out})^2} \tag{4.10}$$

where N is the number of binned protons in the central pixel $j = (0,0)$. The fluence of protons in the central pixel is defined as $\Phi^{out}_{(0,0)}(w) = N/a^2$. Equation 4.10 then translates to the noise in the center-binned RSP-map given by,

$$\sigma_{RSP(\boldsymbol{c})} = \frac{\pi}{\sqrt{12a^4 P \Phi^{out}_{(0,0)}(w^c)}} \frac{\sigma_{E^{out}}}{S_{\text{water}}(E^{out})}. \tag{4.11}$$

Since we are interested by the noise level in the center of the CT image at a given dose, we relate the central dose D_c to the total number of particles crossing the center for the entire scan. Under a straight line path approximation, in the center-binned projection, the exit fluence is related to the entrance fluence by

$$\Phi^{out}_{(0,0)}(w^c) = \Phi^{in}_{(0,0)} \exp(-2\kappa_{\text{mat}} r) \tag{4.12}$$

where r is the radius of the scanned cylinder and κ_{mat} is the attenuation coefficient of the material. The fluence in the center of the object, Φ^c, can be expressed in terms of the incident fluence $\Phi^{in}_{(0,0)}$ as

$$\Phi^c = \Phi^{in}_{(0,0)} \exp(-\kappa_{\text{mat}} r). \tag{4.13}$$

The absorbed dose in the center D^c is related to the fluence in the center Φ^c by

$$D^c = P\Phi^c \left(\frac{S_{\text{mat}}(E^c) + \kappa_{\text{mat}} \gamma E^c}{\rho_{\text{mat}}} \right) \tag{4.14}$$

where $S_{\text{mat}}(E^c)$ is the proton stopping power of the material for central energy E^c, ρ_{mat} is the mass density of the material and γ=0.65 is the energy-dependent fraction of energy transferred to *secondaries* during nuclear interactions (Schulte et al., 2005). Combining Equation 4.12, Equation 4.13 and Equation 4.14 to solve for the standard deviation $\sigma_{\text{RSP}(\boldsymbol{c})}$ gives,

$$\sigma_{\text{RSP}(\boldsymbol{c})} = \frac{\sigma_{E^{out}}}{S_{\text{water}}(E^{out})} \frac{\pi}{\sqrt{\dfrac{12a^4 D^c \rho_{\text{mat}} \exp(-\kappa_{\text{mat}} r)}{S_{\text{mat}}(E^c) + \kappa_{\text{mat}} \gamma E^c}}} \tag{4.15}$$

The methods presented here are the basis for the attenuation and scattering pCT. Further results and analysis of energy-loss pCT are presented in the next chapter.

Chapter 5

Attenuation proton CT

Contents

Proton interaction in matter not only involves energy loss but also nuclear scattering. In this chapter, we present a method for exploiting the inelastic nuclear scattering to reconstruct the inelastic cross-section map of the object. This approach, also known as transmission radiography and scattering radiography in the early days, is similar in principle as what is done in xCT. Characterization and comparison in terms of accuracy, precision and spatial resolution between the two pCT modalities, i.e. RSP-map for energy-loss pCT and κ-map for attenuation pCT were carried out. This work has been published in Physics in Medicine and Biology (PMB) (Quiñones et al., 2016).

5.1 The inverse problem

A proton beam can be characterized by its fluence Φ defined as the number of protons $\mathrm{d}N$, during a given exposure or treatment, crossing an infinitesimal element of area $\mathrm{d}A$ normal to the direction of the beam, $\Phi = \mathrm{d}N/\mathrm{d}A$. As mentioned in subsection 3.2.2, we assume that only the *inelastic* nuclear interactions remove *primaries* from the incident beam, hence, the attenuation of the *primary* fluence. When a proton beam with an initial fluence Φ^{in} at the entrance detector traverses an object and assuming that all protons follow the same path $\mathbf{\Gamma}$ and the *inelastic* nuclear cross-section is independent of the proton energy, the *primary* fluence

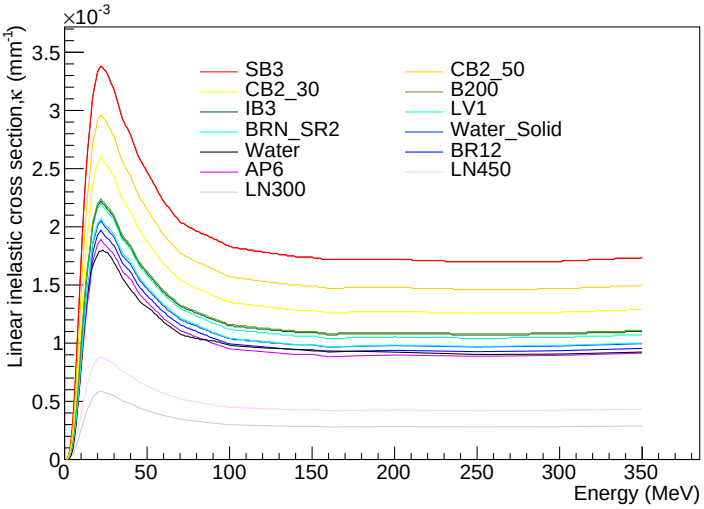

Figure 5.1: The linear *inelastic* cross-section of each tissue insert of the Gammex 467 phantom as a function of energy

decreases exponentially according to the exponential law given by

$$\Phi^{out} = \Phi^{in} \exp\left(- \int_{w^{in}}^{w^{out}} \kappa(\mathbf{\Gamma}(w)) \mathrm{d}\mathbf{\Gamma}(w) \right) \tag{5.1}$$

where κ is the 3D map of the linear macroscopic *inelastic* nuclear cross-section of protons in a material (Schulte et al., 2005; Bopp et al., 2013) and Φ^{out} is the fluence of protons detected by the tracking detector at position w^{out}. The assumption that the attenuation coefficient κ is only due to *inelastic* nuclear scattering is only valid if all the *primaries* with *elastic* nuclear scattering are counted by the exit detector.

Figure 5.1 shows the κ-values as a function of energy for the different materials of the Gammex 467 phantom (Gammex, Middleton, WI). Since the *inelastic* nuclear cross-section depends weakly on the energy for proton energies between 100 MeV and 300 MeV, it can be assumed to be independent of penetration depth. This further validates Equation 5.1 in the energy range considered for pCT if the residual energy is greater than 100 MeV.

In practice, each proton follows a different path and we propose to account for each path using the distance-driven binning which was first implemented for pCT reconstructions exploiting their energy loss in Rit et al. (2013). In the distance-driven binning algorithm, the projection value for each proton pair is scored with respect to different positions in space defined by the MLP. The same technique has been applied here except that the protons were counted during the distance-driven binning instead of averaging the energy-loss WEPL. Since proton scattering is 3D in nature, the fluence was calculated by considering those protons that went through the same 3D position in space for a given distance w.

The entrance fluence per pixel $\boldsymbol{j}$ with sampling size a both in the $\boldsymbol{u}$ and $\boldsymbol{v}$ directions is defined as,

$$\Phi^{in}_{\boldsymbol{j}} = \frac{1}{a^2} \sum_{k \in K} h_{\boldsymbol{j}}(u^{in}_k, v^{in}_k) \tag{5.2}$$

where K is the set of protons measured at the entrance detector for the current source position and the 2D coordinate (u_k^{in}, v_k^{in}) is the entrance position $\mathbf{\Gamma}(w^{in})$ projected onto the exit detector, as illustrated in Figure 4.2 for the first coordinate. The distance-driven fluence of the exit proton beam in a pixel $\boldsymbol{j}$ is then defined as,

$$\Phi_{\boldsymbol{j}}^{out}(w) = \frac{1}{a^2} \sum_{i \in I} h_{\boldsymbol{j}}(u_i(w), v_i(w)) \tag{5.3}$$

with $I \subset K$ the set of protons measured both at the entrance and the exit detector for the current source position and the 2D coordinate $(u_i(w), v_i(w))$ the projection of the 3D position $\mathbf{\Gamma}(w^{in})$ of the i-th proton at distance w onto the exit detector. Finally, the distance-driven projections are defined as,

$$g_{\boldsymbol{j}}^{\mathrm{a}}(w) = -\ln\left(\frac{\Phi_{\boldsymbol{j}}^{out}(w)}{\Phi_{\boldsymbol{j}}^{in}}\right). \tag{5.4}$$

A distance-driven projection is computed for each source position and reconstruction of the κ-map is then carried out using the same reconstruction algorithm as in Rit et al. (2013) and previously mentioned in section 4.4, *i.e.*, the FDK algorithm (Feldkamp et al., 1984) adapted with a voxel-specific backprojection selecting the distance w according to the distance between the voxel and the exit detector for each source position.

5.2 Statistical limitations

Following the formalism in estimating the noise in the RSP-map presented in section 4.5, the noise in the center of the center-binned κ-map is given by,

$$\sigma_{\kappa(\boldsymbol{c})} = \frac{1}{P} \sum_{p=1}^{P} f \sigma_{g_{\boldsymbol{j}}^{\mathrm{a}}(w^c)}. \tag{5.5}$$

In attenuation pCT, fluctuations in the estimate of the absorption coefficient are dependent on the statistics of the fluence of the exit protons $\Phi_{\boldsymbol{j}}^{out}$ detected at the exit detector. Using the first-order error propagation, the noise in the projection $g_{\boldsymbol{j}}^{\mathrm{a}}(w^c)$ is given by,

$$\sigma^2_{g_{\boldsymbol{j}}^{\mathrm{a}}(w^c)} = \sigma^2_{\Phi_{\boldsymbol{j}}^{out}} \left(\frac{\mathrm{d}g_{\boldsymbol{j}}^{\mathrm{a}}(w^c)}{\mathrm{d}\Phi_{\boldsymbol{j}}^{out}}\right)^2 \tag{5.6}$$

$$\tag{5.7}$$

Using the properties of a Poisson probability function, the variance of the detected protons is just the mean of the distribution, hence, $\sigma^2_{\Phi_{\boldsymbol{j}}^{out}} = \bar{\Phi}_{\boldsymbol{j}}^{out}$. After solving for the term in parenthesis, wherein the incident fluence $\Phi_{\boldsymbol{j}}^{in}$ is constant, the variance of the projection $\sigma^2_{g_{\boldsymbol{j}}^{\mathrm{a}}(w^c)}$ is

$$\sigma^2_{g_{\boldsymbol{j}}^{\mathrm{a}}(w^c)} = \bar{\Phi}_{\boldsymbol{j}}^{out} \left(\frac{1}{\bar{\Phi}_{\boldsymbol{j}}^{out}}\right)^2. \tag{5.8}$$

This then translates to a noise in the center-binned κ-map given by

$$\sigma_{\kappa(\boldsymbol{c})} = \frac{\pi}{\sqrt{12a^4 P \bar{\Phi}^{out}_{(0,0)}(w^c)}}. \tag{5.9}$$

Converting the exit fluence for all projections P to the equivalent dose deposited in the center results to

$$\sigma_{\kappa(\boldsymbol{c})} = \frac{\pi}{\sqrt{\dfrac{12a^4 D^c \rho_{\text{mat}} \exp(-\kappa_{\text{mat}} r)}{S_{\text{mat}}(E^c) + \kappa_{\text{mat}} \gamma E^c}}}. \tag{5.10}$$

Relating the ratio of the relative precision for attenuation and energy-loss pCT gives

$$\frac{\sigma_{\kappa(\boldsymbol{c})}/\kappa_{\text{mat}}}{\sigma_{\text{RSP}(\boldsymbol{c})}/\text{RSP}_{\text{mat}}} = \frac{S_{\text{water}}(E^{out})\text{RSP}_{\text{mat}}}{\sigma_{E^{out}}\kappa_{\text{mat}}}. \tag{5.11}$$

This ratio quantifies the advantage of energy-loss pCT over attenuation pCT in terms of noise for the same imaging dose.

5.3 Simulation experiments

The accuracy and precision of the proposed attenuation pCT to generate κ-maps were evaluated using a homogeneous water cylindrical phantom and the Gammex 467 phantom. The spatial resolution at a given depth was assessed using the Catphan 528 and the Spiral phantom described below. The κ-maps were then compared qualitatively and quantitatively with the RSP-maps acquired from energy-loss pCT.

5.3.1 Experiment 1: water cylindrical phantom

A pCT system was simulated using GATE v7.1 (Jan et al., 2011) to evaluate the precision (section 4.5 and section 5.2) of the new method of attenuation pCT incorporating the MLP. The setup is composed of a radiation source, a phantom and two perfect tracking detectors. A fan beam proton source was placed at 5 m from the isocenter with dimensions at the isocenter of 267 mm and 5 mm in the $\boldsymbol{u}$ and $\boldsymbol{v}$ directions, respectively. A total of 360 projection angles at one degree intervals was carried out. The $\boldsymbol{\Gamma}_i(w^{in})$ and $\boldsymbol{\Gamma}_i(w^{out})$ positions were recorded by the 25.7 cm $\times$ 10 cm tracking detectors located at 1 cm before and after the phantom. The QGSP_BIC physics list of Geant4.10.01.p02 and a proton step size limit of 1 mm were used for the Monte Carlo simulation purposes throughout this study.

To validate Equation 4.15 and Equation 5.10, we used a cylindrical phantom with a diameter of 20 cm filled with water. The incident energies considered were 200 MeV and 300 MeV which have enough momentum to traverse 20 cm homogeneous water. Two pCT acquisitions were carried out (1) using energy loss to generate an RSP-map and (2) using attenuation to generate a κ map. Distance-driven binned projections were obtained and binned in a lattice of $257 \times 1 \times 257$ samples with $1 \times 100 \times 1$ mm^3 spacing. In our simulations, the incident fluence $\Phi^{in}_{\boldsymbol{j}}$ was a known constant for all

pixels determined by the simulation geometry and the number of simulated incident protons (in practice, a projection without an object, *i.e.*, a *flat field* projection, would be required).

Since a fraction of the incident protons undergoes nuclear interactions while traversing a medium, the protons that are detected by the exit tracking detectors consist of both *primaries* and *secondaries*. The exit energy distributions per pixel are non-Gaussian, with a tail on the left side of the distributions as shown in Figure 3.3. At the central pixel of the exit detector, where most protons traverse 20 cm of water, around 96% are *primaries* of which only 86% are *primaries* without any nuclear interactions. The *secondaries* and a fraction of *primaries* with *elastic* scattering contribute to the tails of these distributions. Consequently, these events bias the reconstructed RSP images since they do not conform to the Gaussian model of the small angle MCS (Schulte et al., 2008). To filter these events, a 3σ cut using a robust estimator was imposed on both the energy and angular distributions. Doing this removes 12% of the exit protons, majority of which are *secondaries* and *primaries* with *elastic* scattering. A 3σ cut was however found inapplicable for attenuation pCT as this also removes *primaries* with *elastic* scattering. Instead, a larger 10σ cut on the angular distributions was carried out which is large enough to remove 80% of the *secondaries* while only removing 1% of the *primaries*. Unlike in energy-loss pCT, a sigma cut on the energy distribution was not carried out in attenuation pCT due to the difficulty in characterizing the overlay of several energy distributions at the boundary of heterogeneities (Krah et al., 2015), the obvious outliers being already eliminated by angle cuts.

According to Figure 5.1, the nuclear *inelastic* cross-section κ is only constant above 100 MeV. For this reason, a similar simulation was also carried out using 175 MeV incident proton beam to check the energy dependence of κ on the reconstructed image for low momentum protons.

5.3.2 Experiment 2: Gammex 467 phantom

The accuracy of the reconstruction method was evaluated using the Gammex 467 which has a diameter of 33 cm approximating the size of an average human pelvis and consisting of a matrix of sixteen 2.8 cm diameter holes of various tissue and water materials. The simulation setup is as described in subsection 5.3.1 and a 300 MeV fan beam proton source was used. The dimension of the source was increased to 377 mm at the isocenter in the $\boldsymbol{u}$ direction to irradiate the entire phantom in the plane of the source trajectory. This configuration gives a proton fluence $\Phi_{\boldsymbol{j}}^{in} \simeq 1763$ protons/mm^2 for each projection and a total dose of around 50 mGy at the center of the phantom. The detector size was set to 38 cm $\times$ 10 cm and the projected images were then binned in a lattice with $1 \times 100 \times 1$ mm^3 spacing. The large 100 mm height of the detector is required to measure as many scattered primaries as possible (Figure 3.3). Nuclear cuts as described in the previous section were also implemented. Table 5.1 shows the different intrinsic values of each insert. The density ρ, stopping power $\mathrm{d}E/\mathrm{d}x$ and RSP values were taken from Arbor et al. (2015) while the κ values were extracted from the Geant4 database of *inelastic* nuclear cross-sections.

Table 5.1: Densities ρ, stopping powers dE/dx, relative stopping powers RSP and linear nuclear *inelastic* cross-section κ values of the materials of the Gammex 467 calibration phantom for a 300 MeV proton beam.

Material	ρ (g cm^{-3})	dE/dx (MeV cm^{-1})	RSP	κ ($\times 10^{-4}$ mm^{-1})
LN300 lungs	0.30	1.023	0.291	2.84
LN450 lungs	0.45	1.552	0.442	4.26
AP6 Adipose	0.94	3.314	0.943	9.00
BR12 Breast	0.98	3.412	0.971	9.41
Water Solid CT	1.02	3.506	0.998	9.82
Water Insert	1.00	3.513	1.000	9.24
BRN-SR2 Brain	1.05	3.726	1.060	9.87
LV1 Liver	1.10	3.755	1.068	10.6
IB Inner Bone	1.14	3.808	1.083	10.9
B200 Bone Mineral	1.15	3.843	1.093	11.0
CB2-30% CaCO 3	1.34	4.468	1.271	12.8
CB2-50% CaCO 3	1.56	5.051	1.437	14.8
SB3 Spine Bone	1.82	5.733	1.631	17.3

5.3.3 Experiment 3: Catphan 528 phantom

To evaluate the spatial resolution of the imaging method qualitatively, the Catphan 528 high resolution phantom was used which is made up of a 20 cm water cylinder with 21 line patterns of 22 mm-thick aluminum sheets. The simulation geometry is also the same as subsection 5.3.1 using a 200 MeV incident proton beam and a dose of around 50 mGy at the center was considered. Two paths were considered during reconstruction: (1) the MLP using the distance-driven projections $g_{\boldsymbol{j}}(w)$ and (2) the SLP using only the exit projections $g_{\boldsymbol{j}}(w^{out})$. To account for all the protons binned at the exit detector for the SLP estimate, the images were binned and reconstructed on a $512 \times 1 \times 512$ grid with a $0.5 \times 100 \times 0.5$ mm^3 voxel size.

5.3.4 Experiment 4: Spiral phantom

The Spiral phantom is a 20 cm water cylinder with 21 aluminum cylindrical inserts of 15 mm diameter and arranged in a spiral manner. This phantom is used to evaluate the spatial resolution of the imaging method at different distances from the center of the reconstructed image. The images were also binned and reconstructed on a $512 \times 1 \times 512$ grid with $0.5 \times 100 \times 0.5$ mm^3 voxel size. This configuration is sufficient to have a good counting statistics (1172 protons per pixel per projection on average) for attenuation pCT. The simulation geometry is the same as subsection 5.3.1 using a 200 MeV incident proton beam and a total dose of around 50 mGy at the center.

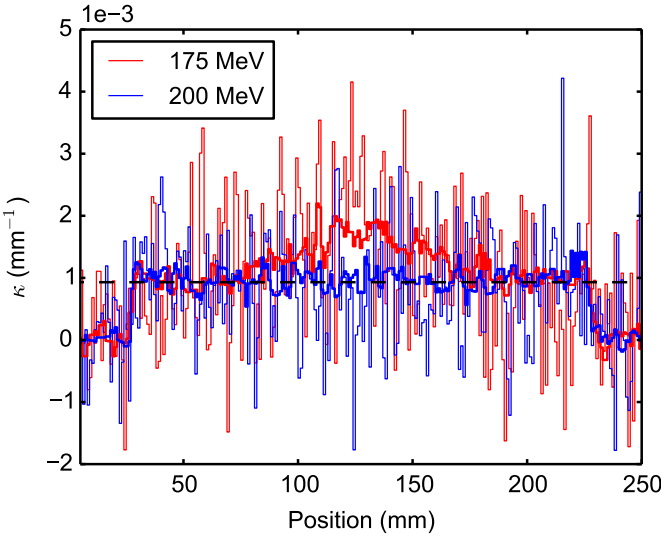

Figure 5.2: Line profiles of the reconstructed κ map of the water cylinder as a function of position for 175 MeV and 200 MeV. The horizontal dashed lines mark the nuclear *inelastic* cross-section value for water. The thick lines are profiles of the CT images after passing a 17×3 median filter on the CT image to reduce background noise and enhance low-frequency information.

5.4 Results

5.4.1 Experiment 1: water cylindrical phantom

Figure 5.2 shows the attenuation line profile of the MLP reconstruction of a homogeneous water cylinder for incident energies of 175 MeV and 200 MeV. It is observed that the line profiles have large fluctuations between neighboring pixels. A low-frequency inhomogeneity or *capping* artifact, best visible on the profiles of the median-filtered images, is also apparent for 175 MeV incident energy, *i.e.*, it shows that the attenuation values are not flat throughout the phantom wherein the central part is relatively overestimated compared to the phantom periphery.

The precision was evaluated by determining the variability of the reconstructed values for a given dose (Figure 5.3). Incident energies of 200 MeV and 300 MeV were chosen as these do not carry the inherent *capping* artifact present with lower momentum protons. Table 5.2 shows the values extracted from Monte Carlo simulations used to predict analytically the precision (equations Equation 5.10 and Equation 4.15). The discrete points are the standard deviations at the central pixel from a set of 50 reconstructed pCT maps for reconstructions with and without cuts to select *primaries* for attenuation pCT or *primaries* without nuclear interactions for energy-loss pCT. The graph shows a good agreement of the noise assessment with Monte Carlo simulations and analytical noise (Figure 5.3, discrete points vs continuous lines, respectively). Furthermore, it shows that for attenuation pCT, the relative noise with respect to dose does not vary much with energy and this result is consistent with the fact that the *inelastic* cross-section κ is constant above 100 MeV (Figure 5.1). The RSP-maps exhibit a better noise-dose ratio over the

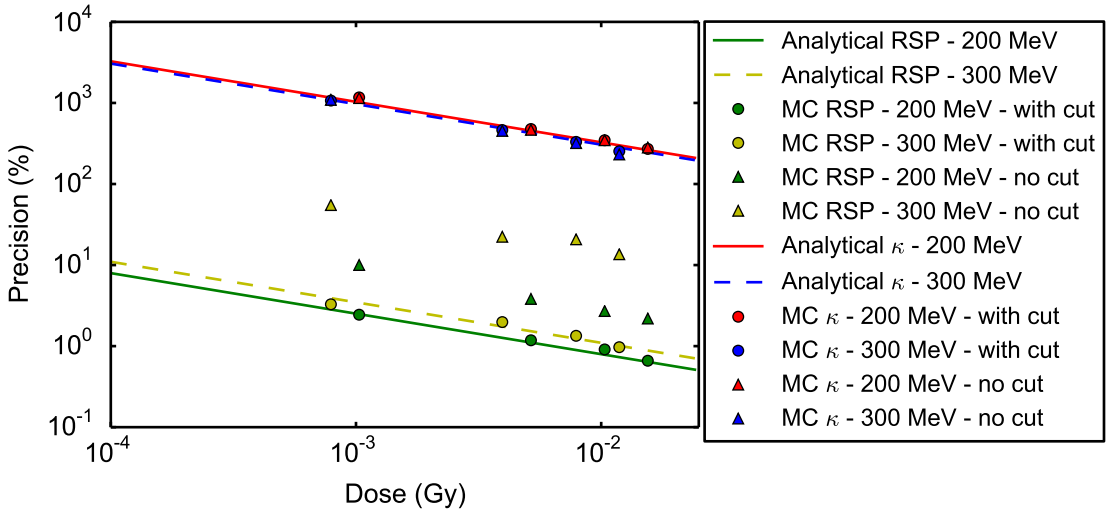

Figure 5.3: Comparison of the analytical estimate of the noise in the center predicted by Equation 5.10 and Equation 4.15 (solid and dashed lines) and the corresponding Monte Carlo simulations for validations (discrete points) for the κ and RSP-maps of a 20 cm water cylinder using incident energies of 200 MeV and 250 MeV. The sampling interval of the reconstructed images is $a = 1$.

Table 5.2: Constants used in this study: the linear nuclear *inelastic* cross-section of the material κ_{mat}, relative stopping power of the material RSP_{mat}, incident energy E^{in}, central energy E^c, stopping power as a function of central energy $S(E^c)$, mean residual energy $\bar{E}^{out}$, stopping power as a function of mean residual energy $S(\bar{E}^{out})$, the standard deviation of the residual energies $\sigma_{\bar{E}^{out}}$ and the fraction of proton energy transferred to secondary charged particles in nuclear interactions γ.

κ_{mat} ($\times 10^{-4}\text{mm}^{-1}$)	RSP_{mat} (no unit)	E^{in} (MeV)	E^c (MeV)	$S(E^c)$ (MeV/mm)	$\bar{E}^{out}$ (MeV)	$S(E^{out})$ (MeV/mm)	$\sigma_{\bar{E}^{out}}$ (MeV)	γ (no unit)
9.224	1	200	152.0	0.537	87.42	0.803	2.119	0.65
9.066	1	300	264.2	0.377	224.2	0.416	1.649	0.65

κ-map (Figure 5.3) with a precision which is about 411 and 278 times lower, as predicted by Equation 5.11 for 200 MeV and 300 MeV respectively. In both pCT reconstructions, the nuclear cuts imposed per pixel were found sufficient to filter out the proton data that do not conform to the reconstruction models and would impact the precision of the reconstructed values. Note, however, that the impact of nuclear *inelastic* interactions on the precision is not significant (Figure 5.3).

5.4.2 Experiment 2: Gammex 467 phantom

The reconstructed CT images of the Gammex 467 phantom are shown in Figure 5.4. The RSP-map shows more distinctly visible tissue inserts than the κ-maps due to the improved contrast-to-noise ratio. Figure 5.5 compares the theoretical and reconstructed κ for the different materials. The 10σ cut on the proton data

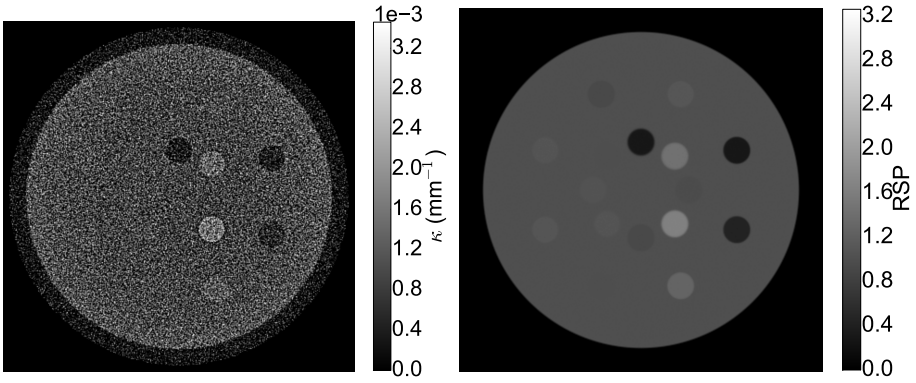

Figure 5.4: The κ-map (left) and RSP-map (right) of the Gammex 467 phantom for reconstructions using the MLP. The maximum value of the grayscale was chosen to be twice the maximum theoretical reconstruction value of the insert, which in this case is SB3. The factor 2 is necessary to account for the increase of κ at the borders due to the overshoot at these regions. In both imaging acquisitions, the minimum gray level was set to zero.

significantly improved the estimate of the reconstructed values with up to 10% error compared with 34% when considering all exit protons. While there is a significant improvement when implementing the cuts, the 10σ cut was found to cut more protons than it should have, which explains the overestimate of the reconstructed κ values together with *primaries* that have not been detected because they underwent nuclear *elastic* interaction. Despite the overestimate, the majority of the theoretical κ values still fall within at least 3σ of the reconstructed κ values. For reconstructions without data filtering, it can also be observed that low density materials, *i.e.*, the LN300 and LN450 materials, have negative mean values of the reconstructed κ because *secondaries* reaching the detector behind those inserts bias the accuracy towards negative values.

5.4.3 Experiment 3: Catphan 528 phantom

The spatial resolution was evaluated using the Catphan 528 phantom reconstructed using the MLP and the SLP (Figure 5.6 and Figure 5.7). The CT image reconstructed using the MLP demonstrate a better spatial resolution than the CT image reconstructed with SLP for both imaging modalities. The average line profiles across the first (1 line pair/cm) and fourth (4 line pairs/cm) set of bar patterns for reconstructions using the MLP are shown in Figure 5.7. The reconstructed κ values were, however, overestimated in Figure 5.7 due to the influence of the West-Sherwood effect (West and Sherwood, 1973) (following the nomenclature of (Cormack and Koehler, 1976)), *i.e.*, the interplay of attenuation and MCS around edges. Since the inserts are very small, the West-Sherwood effect gives an overshoot which is about four times larger than the expected value (Figure 5.7, top left).

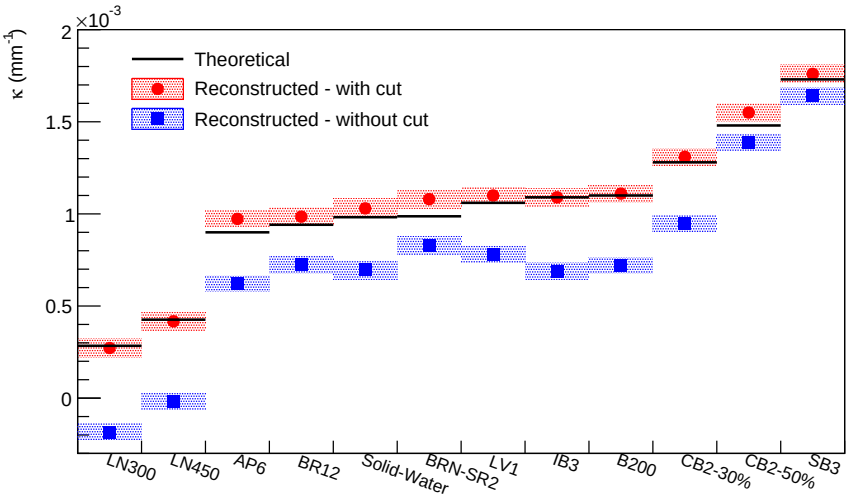

Figure 5.5: The Monte Carlo mean values of the reconstructed κ values of the ROI of each insert of the Gammex 467 phantom compared with the theoretical values. The height of the box plot relates the precision of determining the mean defined as twice the standard deviation of the pixels in the ROI divided by the square root of the number of pixels in the ROI. A similar comparison was carried out for the RSP map of the Gammex 467 implementing the same reconstruction algorithm in Arbor *et al* (2015).

5.4.4 Experiment 4: Spiral phantom

Figure 5.8 shows the reconstructed κ and RSP-maps of the Spiral phantom. Since the SLP images of the Catphan 528 phantom exhibit a poor spatial resolution, only the MLP images of the Spiral phantom are shown. Qualitatively, there is a loss of spatial resolution of the inserts near the periphery of the phantom for the κ-map. This is however the opposite for the RSP-map (Rit et al., 2013), where the inserts at the borders of the phantom show a better spatial resolution. This interesting detail can further be deduced by checking the line profiles of each insert as a function of distance from the center which is shown on the right column of Figure 5.8. In the figure, the overshoot and the undershoot at the borders of the inserts due to the West-Sherwood effect exhibit different amplitudes and the amplitudes vary inversely with the distance from the center. To validate quantitatively the distance to periphery dependence of the spatial resolution, the 10% to 90% distances at the edges are plotted in Figure 5.9. The spatial resolution of the RSP-map indeed improves as a function of distance from the image center while the spatial resolution of the κ-maps decreases with distance from the image center. Furthermore, the graph shows that the κ-map demonstrates a better spatial resolution than the RSP-map. This is found in agreement to the resolution test carried out using the Catphan 528 phantom in the previous section.

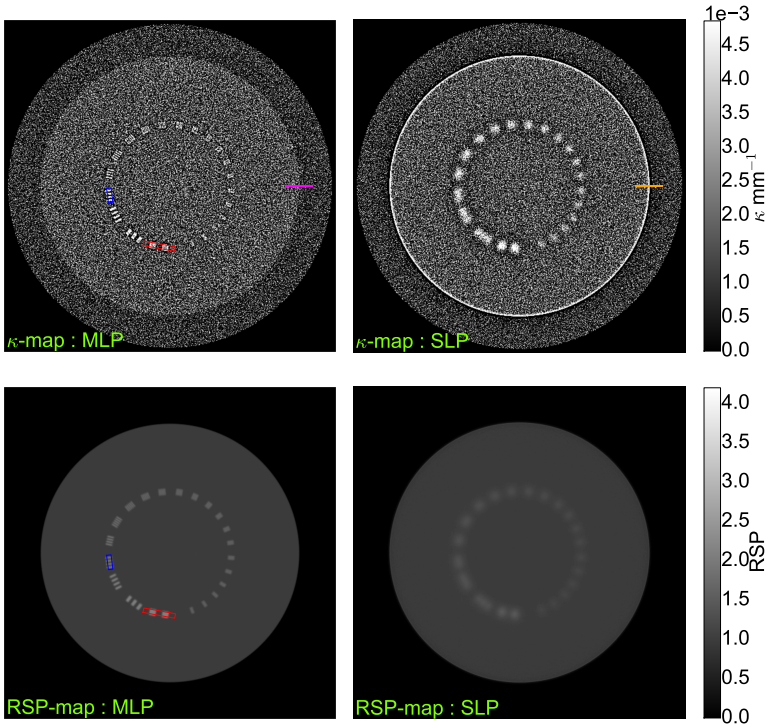

Figure 5.6: The pCT images reconstructed using the attenuation (κ-maps, top) and energy loss (RSP-maps, bottom). On the left column are reconstructions using the MLP while on the right column are reconstructions using SLP. Gray level parameters were set as described in Figure 5.4. The RSP and κ values of aluminum are 2.1 and 2.433 $\times 10^{-4}$ mm^{-1} respectively. The red and blue rectangles are the regions of interest to extract the average line profiles while the yellow and orange lines are the distances considered to extract the average radial line profiles which are shown in Figure 5.7.

5.5 Discussion

We have proposed and characterized an algorithm which integrates a curved most likely path estimate in pCT reconstructions exploiting proton attenuation. While the reconstruction algorithm is the same for both energy-loss and attenuation pCT, differences were observed because of the nature of the projection data.

First, the energy dependence on the accuracy was investigated using a homogeneous water cylindrical phantom. In pCT, the incident energy should be enough for protons to traverse the object to be imaged. For a 20 cm homogeneous water phantom, a 175 MeV proton beam is already sufficient to acquire data for pCT reconstructions. It has been shown in Schulte et al. (2008) for pCT reconstructions using energy loss, that a 175 MeV incident energy demonstrates a better precision than a 200 MeV incident proton beam. The difference between these energies is however not significant in attenuation pCT wherein the variation of κ between these energies is nearly negligible. However, an occurrence of a *capping* artifact has been observed for the κ map reconstructed using incident protons with lower momentum, e.g., for

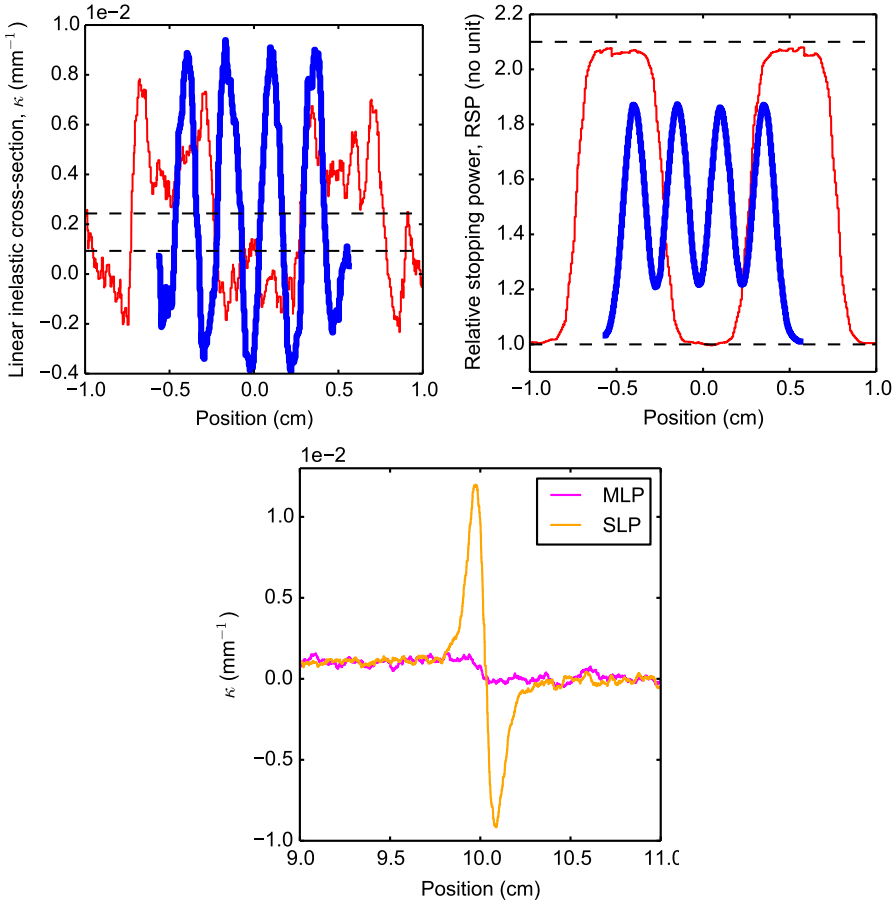

Figure 5.7: The top left and top right figures are the average line profiles of the 1st gauge (1 line pair/cm, red curve) and 4th gauge (4 line pairs/cm, blue curve) for the κ and RSP-maps respectively, for ROIs shown in Figure 5.6. The top and bottom vertical dashed lines are the expected CT values for aluminum and water, respectively. The bottom figure shows the average radial line profiles at the borders of both the MLP and SLP κ-maps.

175 MeV as shown in Figure 5.2. This is quite expected since lower momentum protons undergo more nuclear *inelastic* scattering (Figure 5.1) and in regions where more materials are traversed, such as the center, protons are more attenuated causing an overestimate of κ. The effect is therefore opposite to beam-hardening in xCT. This *capping* artifact is reduced by increasing the energy as shown in Figure 5.2 with a 200 MeV incident proton beam. Hence, for attenuation pCT, residual energies of at least 100 MeV are necessary to avoid inhomogeneity artifacts.

The accuracy of the pCT images is also influenced by the nature of proton interactions inside an object. Protons traversing a medium do not only undergo electromagnetic interactions but also nuclear scattering. During an *inelastic* scattering, the proton loses all its energy to the target nucleus causing the attenuation of the proton fluence. This interaction triggers breakup or excitation of the target nucleus causing the production of *secondaries* among which a majority of protons. A fraction of the attenuation is also due to *elastic* nuclear interaction in which a primary proton is

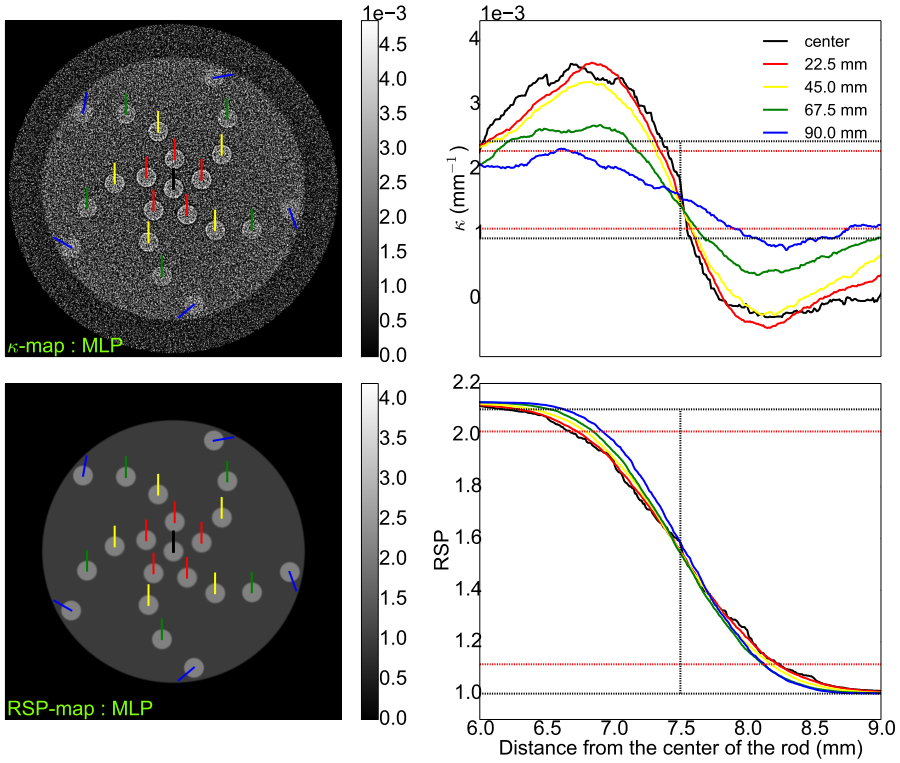

Figure 5.8: The left column shows the pCT images of the Spiral phantom binned using the MLP for κ map (top left) and RSP-map (bottom left) while the right column shows the corresponding average line profiles of the inserts at different distances from the center. The maps on the left column are color-marked accordingly which corresponds to the average radial line profiles on the right column. The black horizontal dashed lines are the theoretical CT values of aluminum (top) and water (bottom) while the red dashed lines are the 90% and 10% of the contrast of the CT values between aluminum and water. The vertical dashed lines mark the edge of the inserts. Gray level parameters were set as described in Figure 5.6.

scattered at large angles. In some events, protons with *elastic* nuclear interactions do not successfully come out of the object, e.g., 2% for 200 MeV and 1.13% for 300 MeV traversing a 20 cm water cylinder. The probability of these events also depends on the thickness of the material. The impact of the attenuation of *primaries* due to *elastic* scattering on the κ-maps partly explains the overestimate of the reconstructed values in Figure 5.5. Hence, aside from the *inelastic* cross-section, there is a thickness and energy dependent component of κ that is due to *elastic* events. In addition, the accuracy is better with RSP-maps compared with the κ-maps because some *elastic primaries* escape the phantom but are not measured by the detector and some *secondaries* are not cut out (Figure 3.3).

Another important aspect which influences the accuracy in pCT is data selection. For energy-loss pCT, a 3σ cut on both the energy and angular distributions has been a standard routine to remove *secondaries* and *primaries* with *elastic* scattering. This procedure is however based under the assumption of a homogeneous phantom. In the case of a heterogeneous phantom, the pixels where there are two or more

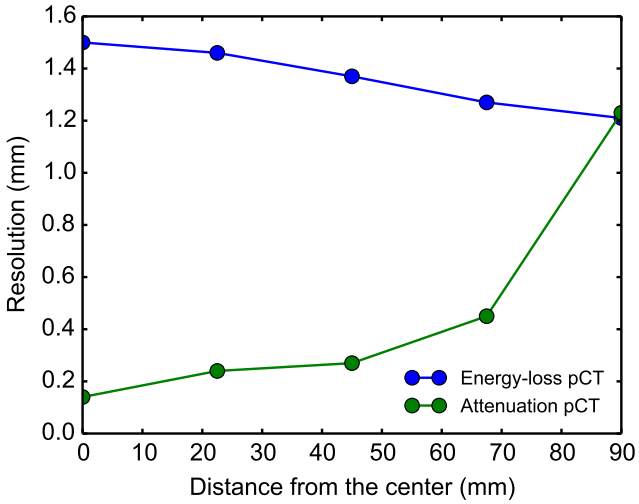

Figure 5.9: The resolution as a function of the distance from the center comparing both pCT modalities. The resolution is defined as the width of the edge response determined by the 10% to 90% distance shown by the figures on the right column of Figure 5.8.

materials, the energy distributions could be made of several overlapping Gaussian distributions (Krah et al., 2015) and the shape of the distributions depends on the densities of the materials involved. This in turn would make the imposed cuts to be inaccurate. In attenuation pCT, only the *secondaries* should be filtered out, hence the use of a 10σ cut. The sigma cut was only imposed on the angular distribution because the energy distribution is strongly influenced by the West-Sherwood effect caused by protons that traverse different materials and are detected in the same pixel. In attenuation pCT, the projection data are based on the counts per pixel and imposing sigma cuts on the energy distribution would influence the κ values near the edges. This is not observed in energy-loss pCT because the projection data are the average of the projection values. Even if larger cuts are used, the effect of the cuts imposed to these non-Gaussian distributions affects the reconstructed κ values. There is however a need to develop an algorithm that could determine appropriate cuts to filter out protons that do not conform to the reconstruction models used for each pCT modality. Solutions proposed in Plautz et al. (2014) involve averaging the modes of the distributions and "splitting" of pixels.

The precision of the CT images at varying doses was also investigated. A significantly better precision is observed for the RSP-maps than the κ-maps (Figure 5.3). Although energy straggling of protons when traversing a medium limits the precision for RSP-maps, lower momentum protons have a noise-dose advantage compared with high momentum protons. This is because the stopping power decreases with energy (Schulte et al., 2005). For attenuation pCT, the precision is influenced by the counting statistics of the incident protons. Since the Poisson noise improves with higher incident proton fluence, higher patient dose would be necessary to acquire an image which would be useful for treatment planning. A dose limit is not yet established for clinical pCT; however, Schulte et al. (2004) suggested a maximum dose of

50 mGy per scan. In the simulation experiments that were carried out, a 50 mGy dose was set to image the different phantoms and with that level of dose, the noise is dominant as shown by the CT images (Figure 5.4, Figure 5.6 and Figure 5.8).

The spatial resolution of the CT images reconstructed with different path estimates were also evaluated as shown in Figure 5.6. It is observed that images reconstructed with curved paths (MLP) demonstrate an improved spatial resolution compared to the CT images reconstructed with straight paths (SLP) for both energy-loss and attenuation pCT. Moreover, attenuation pCT images show enhanced material edges as more visibly shown in Figure 5.8. This interesting feature of the attenuation pCT is the occurrence of the West-Sherwood effect which causes undershoots and overshoots at the boundaries of two materials. This phenomenon has also been observed in experimental proton radiographs (West and Sherwood, 1973; Morris et al., 2011; Poludniowski, Allinson, Anaxagoras, Esposito, Green, Manolopoulos, Nieto-Camero, Parker, Price and Evans, 2014) and a correction technique for this effect has been carried out by Zygmanski et al. (2000). The effect was found to be caused by proton scattering along the boundaries of materials with high contrast in densities as in the case of water and aluminum. The West-Sherwood effect is caused by MCS and it is very strong in the κ-map binned using SLPs. It improves the resolution at the borders of the phantom (left figure of Figure 5.6 and the corresponding average radial line profiles at the bottom figure of Figure 5.7) but its interplay with the line patterns degrades their visibility in Figure 5.6). Furthermore, unlike the visibility of the RSP-map line profiles at high spatial frequency which is reduced, their amplitude is nearly invariant in the κ-map. Indeed, the MLP fully corrects for MCS at the edge of the phantom and, therefore, for the West-Sherwood effect (bottom figure of Figure 5.7) since the phantom was simulated in vacuum and the tracking detectors were perfect. There is, however, a residual error in the MLP estimate that increases with the depth in the phantom which leaves part of the West-Sherwood effect and improves spatial resolution in Figure 5.9. Another striking difference between the RSP-map and the κ map is the distance to periphery dependence of the spatial resolution. While the increasing residual uncertainty of the MLP with the distance to periphery limits the spatial resolution in energy-loss pCT, it can be observed that it behaves oppositely for attenuation pCT thanks to the West-Sherwood effect. This edge-enhancing effect is therefore an asset in probing small structures and resolving boundaries near organs at risk in combination with the RSP-map.

Reconstructions carried out in this study are based on a filtered-backprojection algorithm. While iterative pCT reconstructions have already been implemented in other energy-loss based pCT studies (Penfold et al., 2009; Hansen et al., 2014), it would also be worth exploring similar reconstruction methods for attenuation pCT. Improved modeling of the physics in an iterative reconstruction would certainly enhance the quality of both energy-loss and attenuation pCT as in other transmission CT modalities (Nuyts et al., 2013). Moreover, it is a common practice in imaging to balance the noise level and image resolution to achieve an optimal result. As predicted by Equation 5.11 and while considering the same imaging dose for both modalities, the noise in κ-maps is at least 250 times larger than that of RSP-maps. RSP-maps already demonstrate less than 1% precision even with less than 10 mGy of dose. Increasing the pixel size for κ map to achieve the same noise level as the RSP-

map reconstructed with lower pixel size would also compromise the spatial resolution of the CT image. For this reason, attenuation pCT with reasonable precision is not yet achievable at clinical doses with the proposed reconstruction method.

Proton therapy requires treatment planning protocols that reduce uncertainties in the estimate of the proton range. Satisfying clinical constraints, scientists have been actively developing not only pCT reconstruction algorithms but also particle detectors that maximize the overall performance of the imaging modality. One merit of attenuation pCT is the use of only a set of tracking detectors located downstream and upstream the object to acquire the raw data for reconstruction compared with the energy-loss pCT which needs an additional detector, e.g., a calorimeter, to measure the residual energy. While attenuation pCT could not be a stand-alone imaging modality for proton therapy due to the need of high dose to achieve an acceptable precision, it could, however, bring additional information. Reconstruction methods which involve both proton attenuation and energy-loss would be a promising research direction. Also, for non-medical applications, where high doses on the object would not be critical, *e.g.*, in nondestructive testing and evaluation of very thick materials, high-energy protons could be an ideal solution as they are highly penetrating unlike X-rays which can be easily attenuated. High-energy proton radiography and ultimately tomography has also been a subject of interest for the detection of microporosity in aeroengine turbine castings (Stafford et al., 1975) and advanced hydrotesting (Morris et al., 2011, 2013), among others.

5.6 Conclusions

We have presented a pCT reconstruction method using proton attenuation implementing the MLP estimate through distance driven binning. Results show that incorporating a curved path during reconstruction improves significantly the spatial resolution compared with straight line paths, not only for energy-loss pCT but also for attenuation pCT. It has also been observed that there is an occurrence of a *capping* artifact for reconstructions with proton residual energies below 100 MeV. We have derived and validated an analytical formula to quantify the precision in the proposed attenuation pCT reconstruction and the noise-dose relationship is at least 250 times better with RSP-maps than κ-maps. While this aspect is important in imaging for radiotherapy applications and is not in favor of attenuation pCT, spatial resolution plays a significant role as well. One merit of κ-maps over RSP-maps is its better spatial resolution in some situations thanks to the West-Sherwood effect, an interesting feature of the attenuation pCT in combination with energy-loss pCT.

Chapter 6

Scattering proton CT

Contents

In this chapter, we further exploit proton interactions aside from the proton energy-loss and attenuation by considering the variance of the small-angle MCS after traversing an object. We call this pCT modality *scattering pCT* and we adapt the same algorithm used in the previous pCT modalities to reconstruct the relative scattering power δ-map of the object. The results of scattering pCT were then compared with energy-loss pCT and attenuation pCT.

6.1 The inverse problem

The inverse problem for scattering pCT is similar with energy-loss pCT. Instead of converting the energy-loss to the energy-loss WEPL G^{e} detected per pixel (Equation 4.5), the variance of the exit angular distribution is converted to the scattering WEPL, which in the context of this study is denoted as G^{s}. The reconstructed value is the relative scattering power δ at the equivalent MCS angle.

From Equation 3.10, the scattering power T is the rate of increase of the angular variance $A = \sigma_\theta^2$ per unit path length defined by the MLP $\mathbf{\Gamma}(w)$, hence,

$$\frac{\mathrm{d}A(\mathbf{\Gamma}(w))}{\mathrm{d}\mathbf{\Gamma}(w)} = T(\mathbf{\Gamma}(w), E^{in}, E(\mathbf{\Gamma}(w))) \tag{6.1}$$

where E^{in} is the incident energy and $E(\mathbf{\Gamma}(w))$ is the energy at the position $\mathbf{\Gamma}(w)$. For a given material and E^{in}, there is a bijection between $E(\mathbf{\Gamma}(w))$ and $A(\mathbf{\Gamma}(w))$.

We then introduce a scattering power τ that depends on A, thus,

$$\tau(\mathbf{\Gamma}(w), E^{in}, A(\mathbf{\Gamma}(w))) = T(\mathbf{\Gamma}(w), E^{in}, E(\mathbf{\Gamma}(w))) \tag{6.2}$$

Therefore, we can express Equation 6.1 as,

$$\frac{\mathrm{d}A(\mathbf{\Gamma}(w))}{\mathrm{d}\mathbf{\Gamma}(w)} = \tau(\mathbf{\Gamma}(w), E^{in}, A(\mathbf{\Gamma}(w))). \tag{6.3}$$

By rearranging Equation 6.3 we get,

$$\mathrm{d}A(\mathbf{\Gamma}(w)) = \tau(\mathbf{\Gamma}(w), E^{in}, A(\mathbf{\Gamma}(w))\mathrm{d}\mathbf{\Gamma}(w). \tag{6.4}$$

We then divide both sides by the scattering power of water evaluated at the angular variance of the material, and then integrating leads to,

$$\int_0^{A^{out}} \frac{\mathrm{d}A(\mathbf{\Gamma}(w))}{\tau_{\text{water}}(A(\mathbf{\Gamma}(w)))} = \int_0^{l} \frac{\tau(\mathbf{\Gamma}(w), A(\mathbf{\Gamma}(w)))}{\tau_{\text{water}}(A(\mathbf{\Gamma}(w)))}\mathrm{d}\mathbf{\Gamma}(w) \tag{6.5}$$

where $A^{out} = \sigma^2_{\theta^{out}}$ is the variance of the angular distribution of the exit protons after traversing the material. Equation B.3 is therefore the inverse problem for scattering pCT. The left-hand side of the equation is material independent, thus we call it the scattering WEPL G^{s} and note it as,

$$G^{\text{s}}(A^{out}) = \int_0^{A^{out}} \frac{\mathrm{d}A(\mathbf{\Gamma}(w))}{\tau_{\text{water}}(\mathbf{\Gamma}(w), A(\mathbf{\Gamma}(w)))}. \tag{6.6}$$

Note that the MCS scattering in the lateral and vertical coordinates is considered an independent statistical process (Schulte et al., 2008), therefore, we can use both projected angles to sample the variance in a pixel. Since the angular distribution per pixel $\boldsymbol{j}$ is centered at zero, therefore, the distance-driven variance of the angular distribution $q_{\boldsymbol{j}}(w)$ is defined as,

$$q_{\boldsymbol{j}}(w) = \frac{\sum_{i\in I} h_{\boldsymbol{j}}(u_i(w), v_i(w))[(\Delta\theta_i^u)^2 + (\Delta\theta_i^v)^2]}{2\sum_{i\in I} h_{\boldsymbol{j}}(u_i(w), v_i(w))} \tag{6.7}$$

where

$$\Delta\theta_i^u = \theta_i^u - \theta_i^u \tag{6.8}$$

and

$$\Delta\theta_i^v = \theta_i^v - \theta_i^v. \tag{6.9}$$

The factor 2 in the denominator indicates that there are two data values per proton.

Finally, the distance-driven binned variances are converted into the scattering WEPL G^{s}, hence, the distance-driven binned projections are defined as,

$$g^{\text{s}}_{\boldsymbol{j}}(w) = G^{\text{s}}(q_{\boldsymbol{j}}(w)). \tag{6.10}$$

Similarly with the inverse problem for energy-loss, for Equation B.3 to be valid implies that the relative scattering power of the material δ_{mat}, i.e.

$$\delta_{\text{mat}} = \frac{\tau_{\text{mat}}(A)}{\tau_{\text{water}}(A)} \tag{6.11}$$

be a constant for all $A \in [0; A^{out}]$. Figure 6.1 (top) shows the scattering power τ as a function of the angular variance A for water and aluminum using 200 MeV and 300 MeV incident energies obtained from MC simulations. The graph shows that the scattering power τ increases with the angular variance A and $1/\beta^2 p^2$ which is the energy dependence of the scattering angle. Calculating δ from the fitted curves results to the bottom figure which shows how δ varies as a function of the angular distribution A. The figure shows that δ is not dependent on the incident energy but is strongly dependent on the MCS angle. The variation of δ with the angular variance A also translates to δ variations as a function of the material thickness. From Equation 3.8, the MCS angle not only depends on the energy loss but also with the radiation length X_0 of the material. As the radiation length X_0 depends on the square of the atomic number Z^2, the variation of δ for aluminum ($Z = 13$) is very pronounced. However, despite this dependency, since the tissues in the human body contain elements with less high atomic number Z, then this effect may not be prominent. Figure 6.2 (bottom) shows how δ varies as a function of the angular variance A for different materials of the Gammex 467 phantom. It is observed that the δ values of all the materials except cortical bone (CB2_50) and spine bone (SB3) are almost invariant, therefore, validating the proof of principle for the inverse problem of scattering pCT to work with biological tissues. The effect of the δ variation for bone will be explored in the following sections.

Considering Equation 3.8, evaluating δ_{mat} at the same energy is the ratio of the inverse of the radiation lengths of the material and water, thus,

$$\delta_{0,\text{mat}} = \frac{T_{\text{water}}(E)}{T_{\text{mat}}(E)} = \frac{X_{0,\text{water}}}{X_{0,\text{mat}}}. \tag{6.12}$$

Therefore, δ_0 is just the δ-value at the entrance of the material, wherein the energies between the two materials are almost the same. Table 6.1 shows the list of materials of the Gammex 467 phantom and the corresponding radiation lengths and δ_0-values obtained using Equation 6.12 and the value at the entrance position obtained from Figure 6.2. The results are in good agreement and we therefore use δ_0 as the reference value for scattering pCT.

6.2 Statistical limitations

Following the formalism in section 4.5, the noise in the center of the center-binned δ-map is given by,

$$\sigma_{\delta(\mathbf{c})} = \frac{1}{P} \sum_{p=1}^{P} f \sigma_{g^{\text{s}}_{\boldsymbol{j}}(w^c)} \tag{6.13}$$

The noise in the estimate of the projection $g^{\text{s}}_{\boldsymbol{j}}(w)$ is influenced by the statistical fluctuations in the measurement of the exit angle θ^{out}. Using a first-order error propagation to solve for the variance of $g^{\text{s}}_{\boldsymbol{j}}(w)$, hence,

$$\sigma^2_{g^{\text{s}}_{\boldsymbol{j}}(w^c)} = \sigma^2_{A^{out}} \left(\frac{\mathrm{d}G^{\text{s}}(A)}{\mathrm{d}A}\bigg|_{A=A^{out}} \right)^2. \tag{6.14}$$

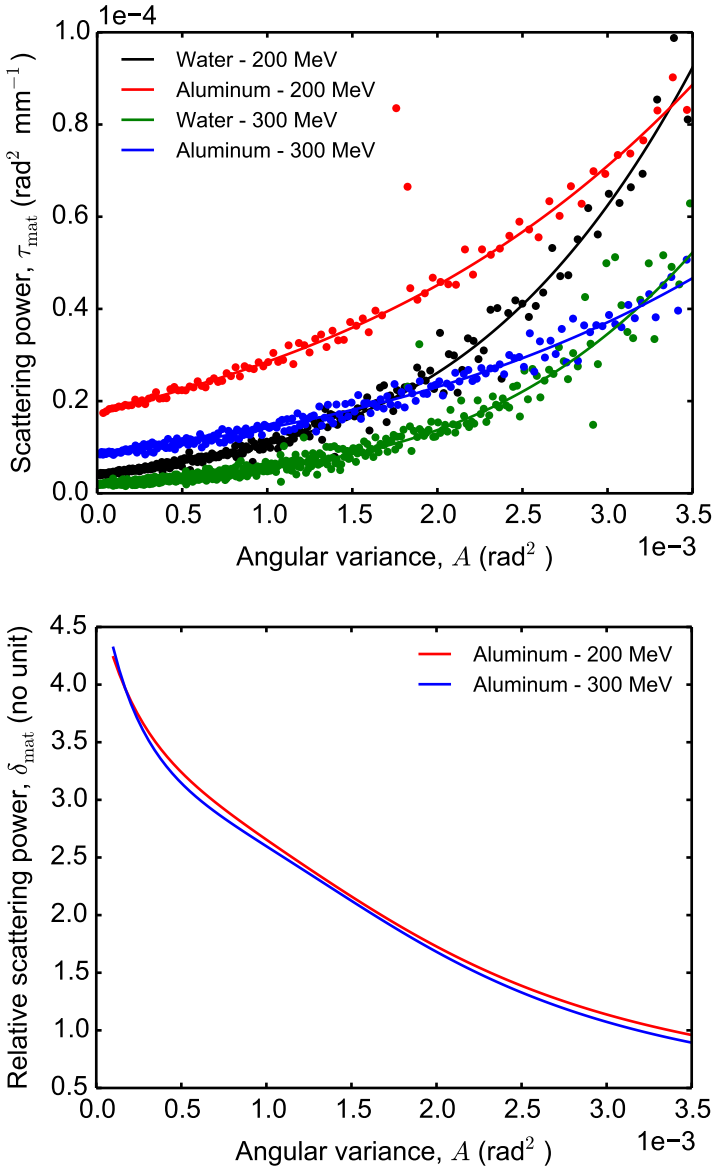

Figure 6.1: Top: Scattering power τ of water and aluminum as a function of exit angular distribution A^{out} using 200 MeV and 300 MeV incident energies fitted with a cubic spline. Bottom: The corresponding relative scattering power δ as a function of the exit angular variance A^{out}. Fitting of the data points was carried out only in the range of [0,A^{out}(thickness = 200 mm] in order not to bias the fit due to the noise of the derivative, i.e. the scattering power τ, beyond the considered range.

It is known that the angular distribution of the MCS angle is composed of a central part which follows a Gaussian distribution and a tail due to single-scattering (Gottschalk, 2010). Therefore the noise of the exit variance can be modeled as,

$$\sigma^2_{A^{out}} = m\left[\frac{2(A^{out})^2}{2N}\right] \tag{6.15}$$

where the term in brackets is the noise contribution of the Gaussian part (Gatti, 2004). The factor m is added to the equation to compensate for the noise contri-

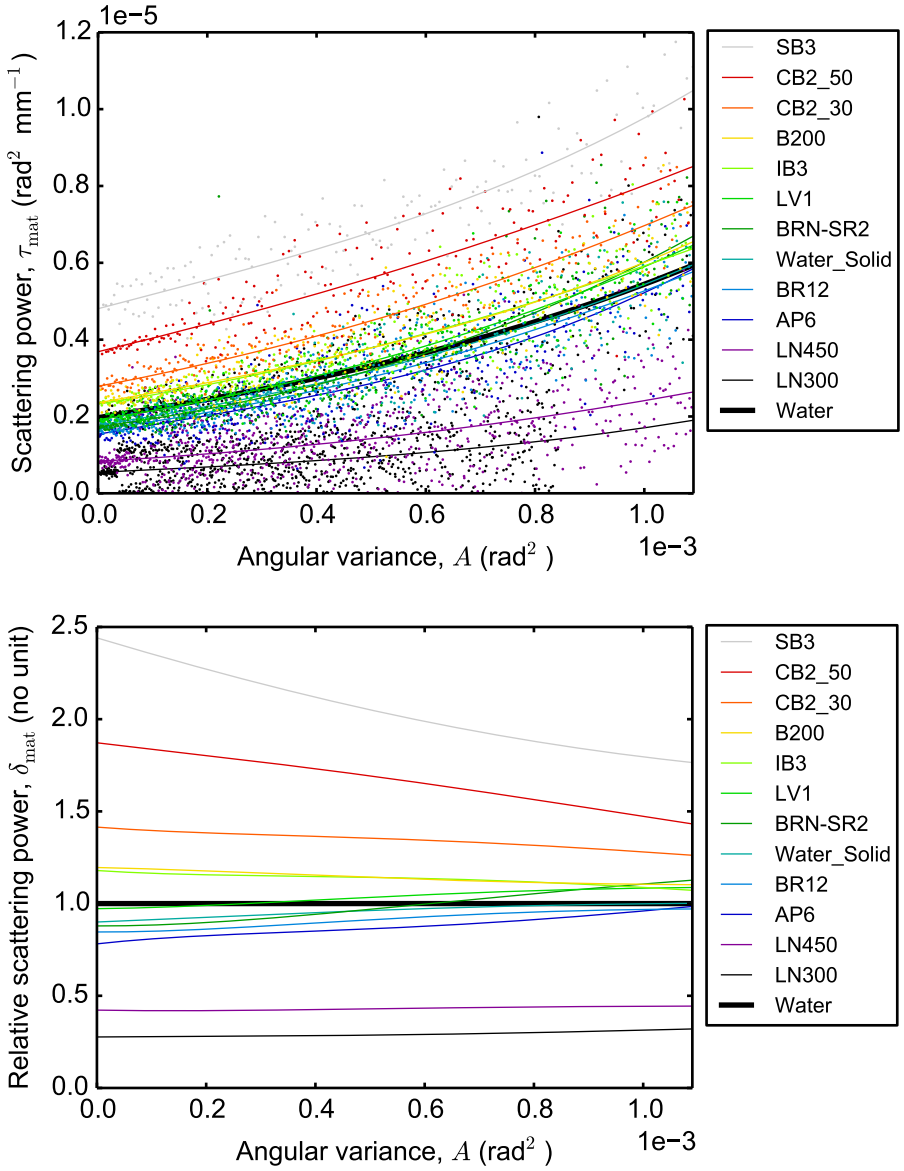

Figure 6.2: Top: Scattering power τ of the different inserts in the Gammex 467 phantom as a function of the exit angular distribution A^{out} fitted with a cubic spline. The discrete points are the derivative of A as a function of thickness, hence, the noise. Bottom: The corresponding relative scattering power δ as a function of the exit angular variance A^{out}. Fitting was considered only within the interval [0, A^{out}(thickness=330 mm)] for water in order not to bias the fit due to the noise of the data sets beyond the range.

bution of the non-Gaussian tail of the angular distribution. The factor 2 in the denominator is due to the use of both projected angles in the u and v directions to sample the variance per pixel for each proton pair.

From Equation 6.6, the term in parenthesis in Equation 6.14 is just $\tau_{\mathrm{water}}(A^{out})^{-2}$.

Table 6.1: The radiation length X_0 and the relative scattering power δ_0 values of the materials in the Gammex 467 calibration phantom.

Material name	Radiation length, X_0 (cm)	Relative scattering power, δ_0 (no unit) $X_{0,\text{water}}/X_{0,\text{mat}}$	Figure 6.2	Error (%)
LN300	128.498	0.28	0.28	-1.51
LN450	85.810	0.42	0.42	0.39
AP6	44.736	0.81	0.78	-3.12
BR12	42.030	0.86	0.85	-1.47
Water_Solid	39.270	0.92	0.90	-2.06
Water	36.089	1.00	1.00	0.00
BRN-SR2	40.473	0.89	0.88	-1.45
LV1	36.409	0.99	0.97	-1.90
IB3	30.734	1.17	1.18	0.43
B200	30.445	1.19	1.20	0.86
CB2_30	25.629	1.41	1.41	0.46
CB2_50	19.607	1.84	1.87	1.70
SB3	15.404	2.34	2.44	4.19

Therefore, the noise in the projection $\sigma^2_{g^s_j(w^c)}$ is given by,

$$\sigma_{g^s_{j,p}(w^c)} = \frac{A^{out}}{\tau(A^{out})}\sqrt{\frac{m}{N}}. \tag{6.16}$$

Equation 6.16 then translates to the noise in the center of a δ-map given by,

$$\sigma_{\delta(\boldsymbol{c})} = \frac{\sqrt{m}A^{out}}{\tau(A^{out})}\frac{\pi}{\sqrt{12a^4P\Phi^{out}_{(0,0)}(w^c)}} \tag{6.17}$$

where $\Phi^{out}_{(0,0)}(w^c) = N(w^c)/a^2$. Finally, the noise in the center of a center-binned δ-map in terms of the central dose is,

$$\sigma_{\delta(\boldsymbol{c})} = \frac{\sqrt{m}A^{out}}{\tau(A^{out})}\frac{\pi}{\sqrt{\dfrac{12a^4D^c\rho_{\text{mat}}\exp(-\kappa_{\text{mat}}r)}{S(E^c)+\kappa_{\text{mat}}\gamma E^c}}}. \tag{6.18}$$

6.3 Materials and methods

6.3.1 LUT for the scattering WEPL

An MC simulation was carried out to create a look-up-table (LUT) for the conversion of the distance-driven-binned angular variances $q_j(w)$ to the scattering WEPL G^s (Equation 6.10). The projection g^s_j is numerically calculated using a linearly interpolated lookup table of G^s. Proton pencil beams with incident energy of 200 MeV were sent to a water box of length equal to the range of the proton, wherein for a

200 MeV proton, the range is around 26 cm. Only primaries without nuclear interactions were considered. The projected angles orthogonal to the beam direction were recorded in 1 mm step interval. Since we only consider the small angle approximation of the MCS, only *primaries* without elastic nuclear interactions were considered in the data. The variance of the angular distribution was calculated using approximately 3.8 million protons. The same procedure was carried out for the LUT of 300 MeV incident protons with a CSDA range approximately at 50 cm.

6.3.2 Homogeneity tests

A standard pCT acquisition was carried out to test the homogeneity of the reconstructed δ-values. First, a 200 MeV proton fan beam incident onto a water cylindrical phantom with a diameter of 200 mm was considered. A perfect cut on the proton data was imposed for scattering pCT, i.e., only the *primaries* without nuclear interactions were used for the reconstruction. This was carried out by recording the nuclear histories of each proton, which include the type of nuclear interactions it underwent and the number of times it underwent such interactions. The nuclear process which creates the secondaries was also tracked and stored. This information could be utilized to exploit other means of proton imaging.

To check the δ variation of high-Z materials such as for aluminum (Figure 6.1), the second setup was with a 50-mm aluminum cylindrical phantom scanned with 200 MeV proton. A smaller diameter for the aluminum cylinder was considered such that the exit variance is within the range of the 200 MeV LUT. A total central dose of 50 mGy was considered and the projections were binned with 1 mm$\times$100 mm$\times$1 mm bin size. The 100 mm size was necessary to include as many protons in the v direction.

6.3.3 Image characterization tests

The same raw data sets as the simulation experiments presented in chapter 5 were used to characterize the accuracy, precision and spatial resolution of the δ-maps. A perfect cut was also imposed on the data selection.

6.4 Results

6.4.1 LUT for the scattering WEPL

Figure 6.3 shows how the variance of the angular distribution A varies as a function of the scattering WEPL G^{s} for incident energies 200 MeV and 300 MeV. The plots are used to evaluate Equation 6.10 for the distance-driven binned projections.

6.4.2 Homogeneity tests

The line profile across the center of the δ-map of the water cylinder shown in 6.4 (top) shows a homogeneity of the δ-values. The bottom figure on the other hand

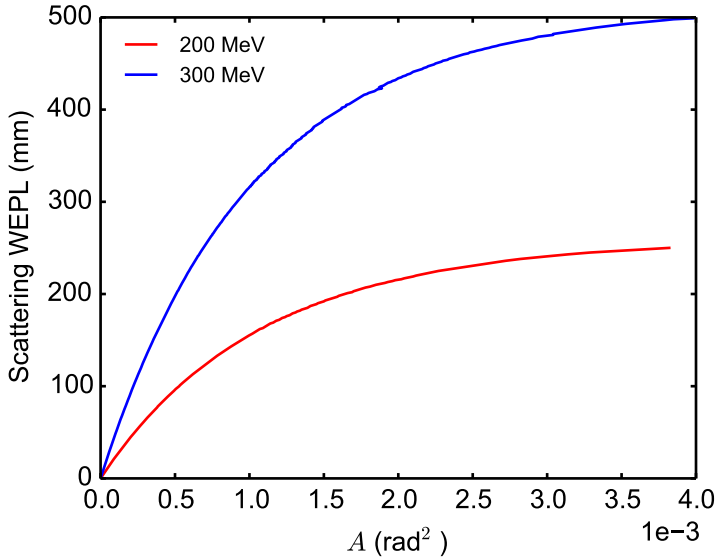

Figure 6.3: The scattering WEPL G^{s} as a function of the variance of the angular distribution A^{out} for 200 MeV and 300 MeV incident protons. The derivative of the function at A^{out} with respect to a discrete WEPL value is the scattering power $\tau(A^{\text{out}})$.

Table 6.2: The parameters used to evaluate Figure 6.5. The rest of the values are shown in Table 5.2.

Incident energy (MeV)	$A^{out}(\text{rad}^2)$	$T(A^{out})(\text{rad}^2\text{mm}^{-1})$	m
200	1.58E-3	1.76E-5	1.92
300	5.02E-4	3.32E-6	3.94

shows the δ-map of the 50 mm aluminum cylinder and indeed shows the variations of the δ-values with depth as depicted in Figure 6.1.

6.4.3 Image characterization tests

Experiment 1: water cylindrical phantom

A 200-mm water cylinder was used to evaluate the noise level in the center of the δ-map scanned with 200 MeV and 300 MeV incident protons. Figure 6.5 shows how the noise level varies with dose. The analytical formula given by Equation 6.18 and shown as solid (200 MeV) and dashed (300 MeV) lines in the graph was validated with 110 independent MC simulations per dose level, shown as discrete points. The factor m to compensate for the non-Gaussian distribution of the exit angles was determined by extracting the MC distance-driven binned variances at the center for 1080 projection samples for the highest dose level and then deducing the factor m for the equation to hold true. The scattering power at an exit angular variance $\tau(A^{\text{out}})$ is just the derivative of the curve in Figure 6.3.

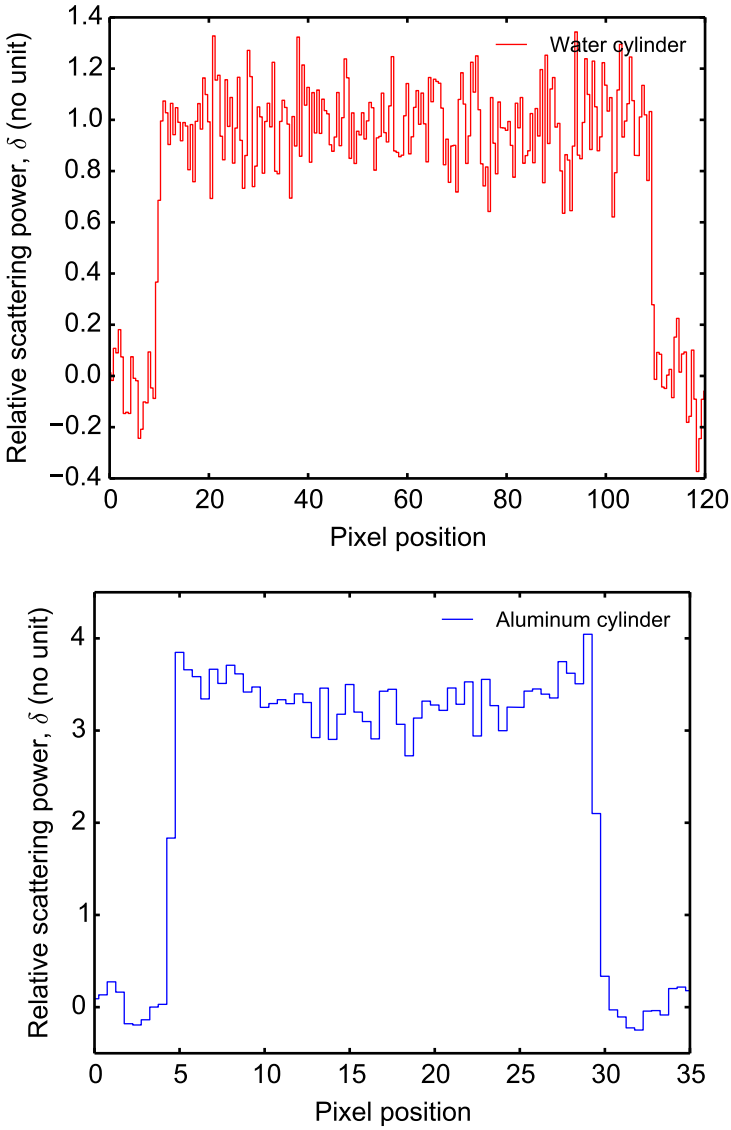

Figure 6.4: Line profile across the center of the scattering pCT image, δ map, of a 200 mm water cylinder (top) and 50 mm aluminum cylinder (bottom) using a 200 MeV incident proton beams for a total central dose of around 50 mGy.

Figure 6.5 shows a good agreement between the analytical noise and the MC simulations. Although there is less scattering with high momentum protons, the graph shows that lower momentum protons yield a better precision compared with higher momentum protons. This is because from Figure 6.1 (top), the curve for water at 200 MeV (black) varies faster than for the 300 MeV case (green). This can also be explained by looking at Figure 6.3, where the derivative of the curve at the same scattering WEPL G^{s}, which yields the scattering power τ is higher with 200 MeV than with the 300 MeV case which then translates to less noise in the image. The analytical formula and the MC are found to be in good agreement. Note, however, that the noise level seems to improve when considering all protons during reconstruction. This is due to the decrease in τ with increasing A, visible by looking at the slope of the curves in Figure 6.3. This, however, affects the accuracy of the

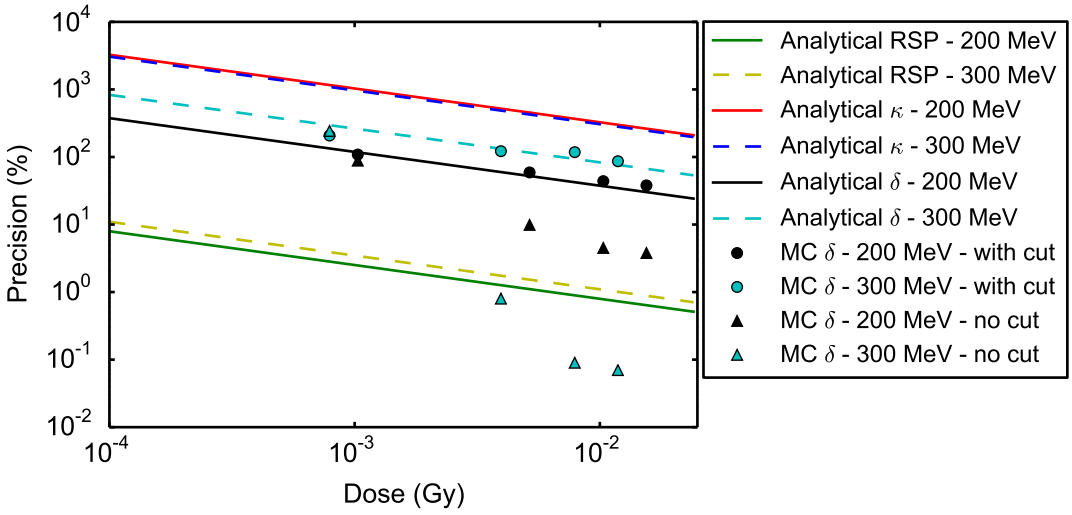

Figure 6.5: Comparison of the analytical estimate of the noise in the center predicted by Equations (5.10), (4.15) and (6.18)(solid and dashed lines) and the corresponding Monte Carlo simulations for validations (discrete points) for the RSP, κ and δ maps of a 20 cm water cylinder using incident energies of 200 MeV and 300 MeV. The sampling interval of the reconstructed images is $a = 1$.

δ-maps, in which, the large angle scattering of the *secondaries* and *primaries* bias the reconstruction of δ. It is also observed that the noise level for scattering pCT is significantly higher than energy-loss pCT but is relatively lower than attenuation pCT.

Experiment 2: Gammex 467 phantom

The reconstructed scattering pCT image of the Gammex 467 phantom is shown in Figure 6.6 (top). Because of the better signal-to-noise ratio of scattering pCT, the δ-map shows a good contrast for some materials, like bone, than the κ-map shown in Figure 5.4. The RSP-map still demonstrate the best signal-to-noise ratio among the three pCT modalities. The δ-map reconstructed without data filtering yielded an image with unrecognizable tissue inserts, and, thus not shown. The bottom figure of Figure 6.6 compares the expected and reconstructed δ-values for the different materials. A significant improvement on the accuracy of the δ-map shown in Figure 6.6 (bottom) was achieved by filtering out those secondaries and primaries which had nuclear interactions. It is also observed that the mean δ-value for the cortical bone CB_50 and spine bone SB3 inserts are underestimated and have the worst accuracy among the inserts. This is because the δ-values for these inserts strongly vary with A unlike the other tissues as shown in Figure 6.2. Moreover, the accuracy of the δ-value is dependent on the position of the insert in the phantom. The inserts in the inner circle are less accurate than the ones in the outer circle. This is because the increasing thickness of the material bias the reconstruction of δ away from δ_0.

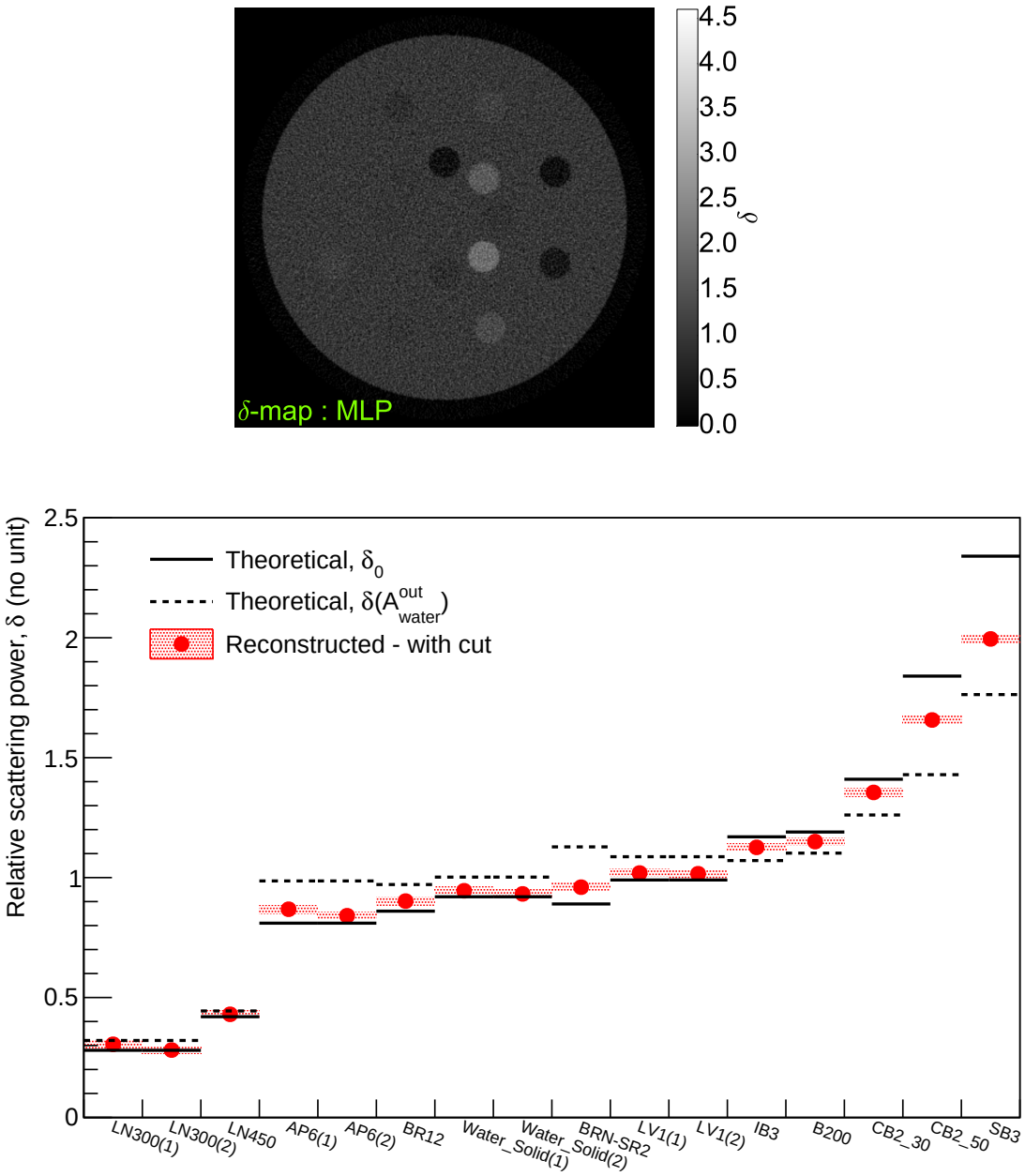

Figure 6.6: Top: The relative scattering power δ-map of the Gammex 467 phantom reconstructed using primaries with no nuclear interactions along the MLP. Bottom: The mean relative scattering power δ of the ROI for each tissue inserts. Inserts with symbol (1) are those found in the inner region while inserts indicated with (2) are in the outer region.

Experiment 3: Catphan 528 phantom

Figure 6.7 (top) shows the δ-maps of the Catphan 528 phantom reconstructed using the MLP (left) and SLP (right). The RSP-maps are also shown at the bottom for comparison. The images show that a significant improvement of the spatial resolution is achieved when using curved proton paths in the reconstructions compared with those reconstructed with straight paths. The average line profiles across the

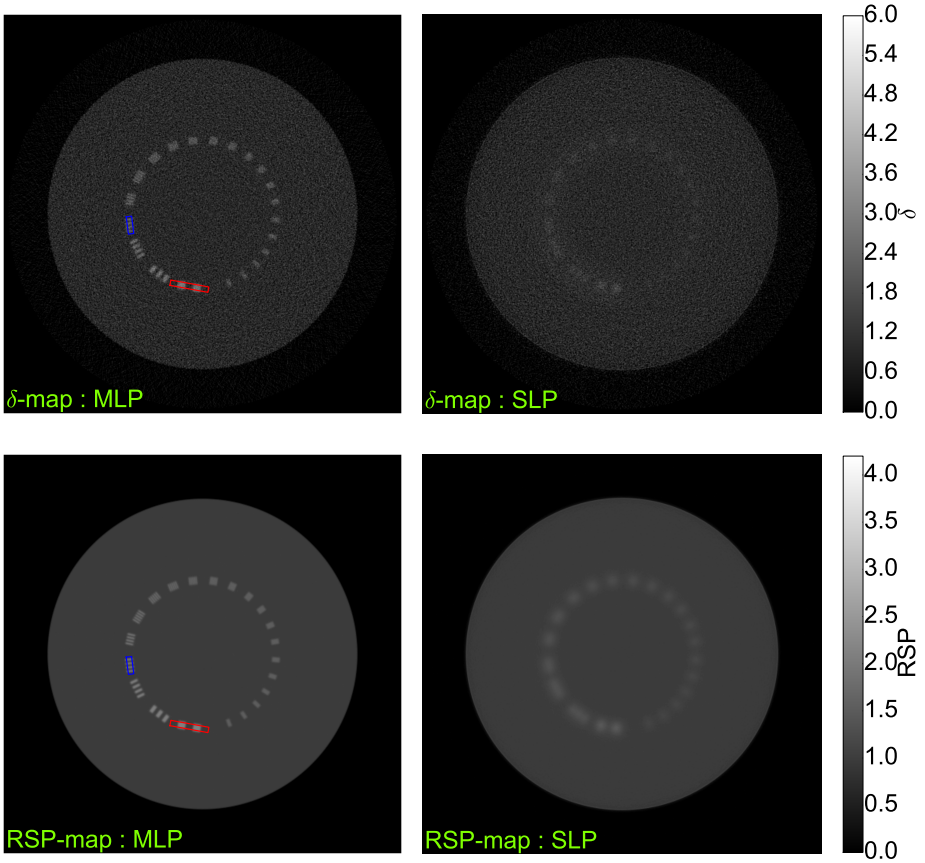

Figure 6.7: The pCT images reconstructed using scattering pCT (δ-maps, top) and energy loss pCT (RSP-maps, bottom). On the left column are reconstructions using the MLP while on the right column are reconstructions using SLP. Gray level parameters were set as described in Figure 5.4. The RSP and δ values of aluminum are 2.1 and 3.0 (based on Figure 6.8, left), respectively. The red and blue rectangles are the regions of interest to extract the average line profiles.

first (1 line pair/cm) and fourth (4 line pairs/cm) set of bar patterns for reconstructions using the MLP are shown in Figure 6.8. Even the aluminum bar patterns are very thin, it can be observed that the δ-values are lower than $\delta_{0,Al} = 4.06$ as observed in Figure 6.1. The spatial resolution of the δ-map and RSP-map reconstructed using the MLP were quantified using the MTF as shown in Figure 6.9. Despite the better accuracy and precision achieved with the RSP-map compared with the δ-map as shown by the line profiles in Figure 6.8, the MTF results shown in Figure 6.9 demonstrate that the spatial resolution of the δ-map is comparable with the RSP-map.

Experiment 4: Spiral phantom

Figure 6.10 (left) shows the reconstructed δ and RSP-maps of the Spiral phantom reconstructed with MLP. The average radial line profiles of the inserts at different distances from the center are shown in the corresponding figure on the right. The

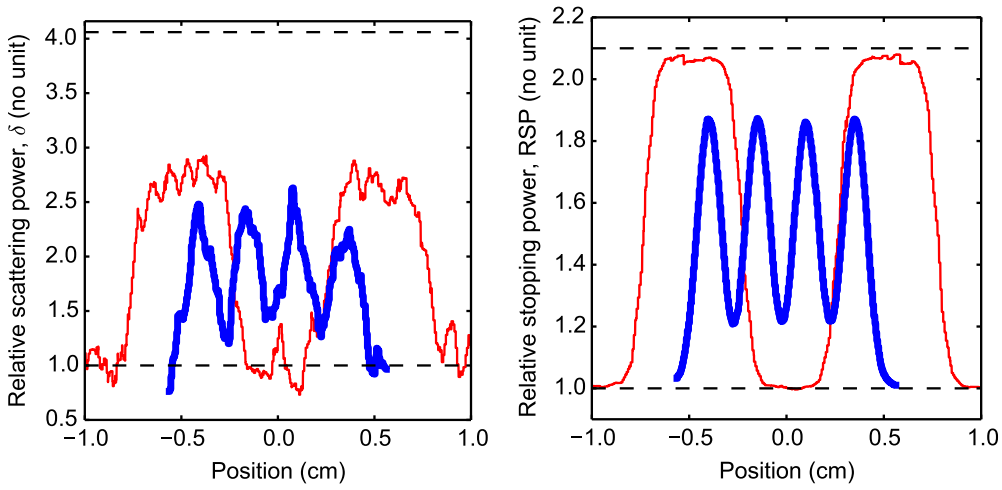

Figure 6.8: The average line profiles of the 1st gauge (1 line pair/cm, red curve) and 4th gauge (4 line pairs/cm, blue curve) for the δ-map (left) and RSP-map (right) respectively, for ROIs shown in Figure 6.7. The bottom dashed lines are $\delta_{\text{water}} = 1$ and $\text{RSP}_{\text{water}} = 1$ while the top dashed lines are $\delta_{0,\text{Al}} = 4.06$ and $\text{RSP}_{\text{water}} = 2.1$.

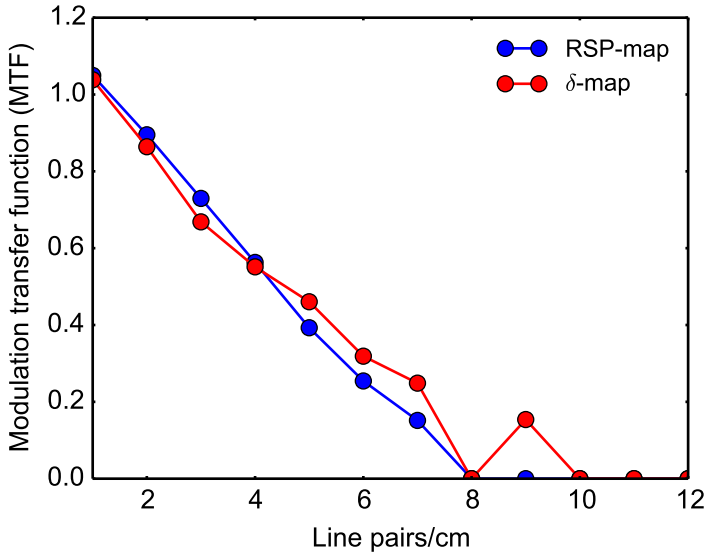

Figure 6.9: Modulation transfer function (MTF) as a measure of the spatial resolution at a specific distance from the center (50 mm) for the RSP and δ pCT images of the Catphan 528 phantom

position dependency of the δ-values for aluminum is clearly visible. The deviation of δ away from δ_0 is around 14% for the inserts at the periphery region and around 21% for the insert at the center.

The spatial resolution as a function of distance from the center of the δ map behaves similarly with the RSP map, i.e. the spatial resolution of the outermost inserts demonstrates a better spatial resolution than the insert at the center. To validate quantitatively the distance to periphery dependence of the spatial resolution,

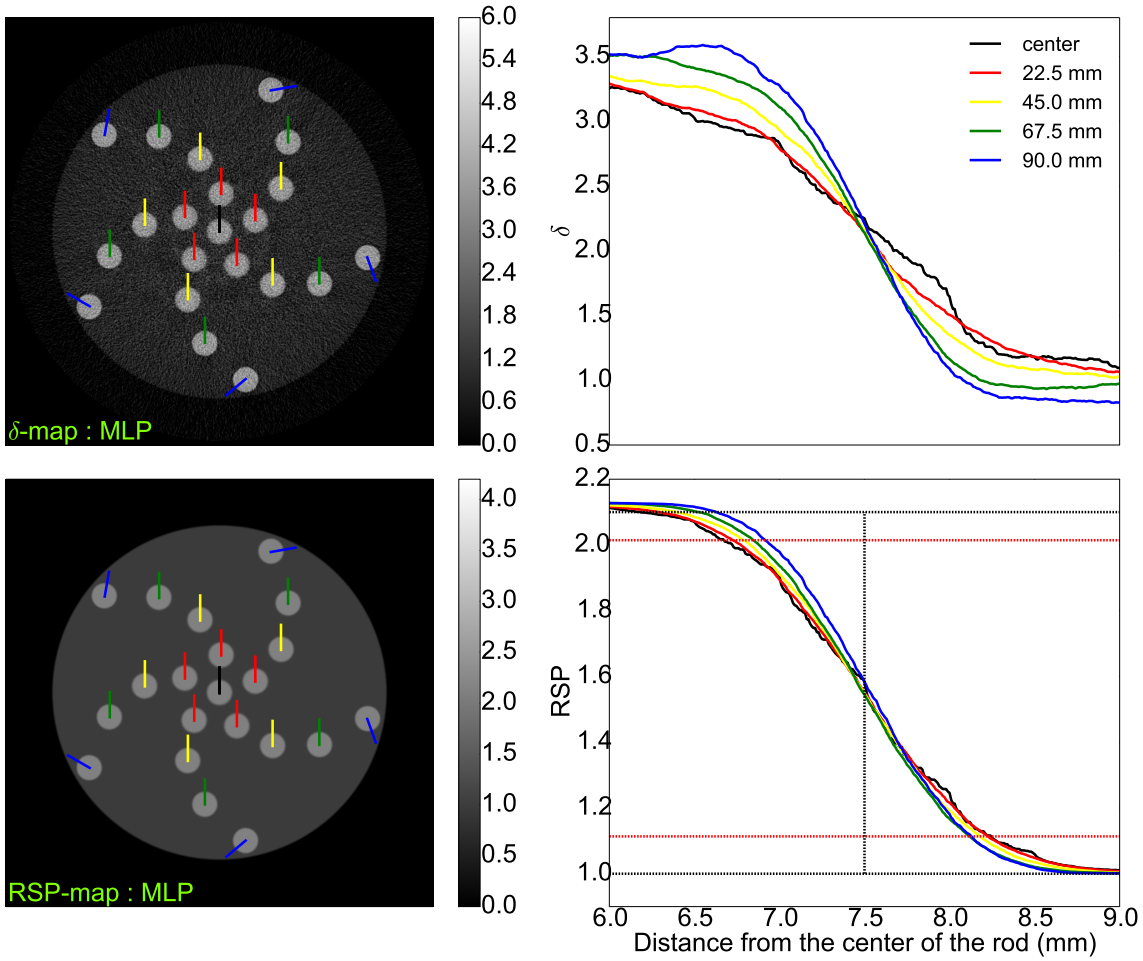

Figure 6.10: (Left) Scattering and energy loss pCT images of the Spiral phantom using a 300 MeV incident energy with a total central dose of around 50 mGy. The minimum image gray level is 0 and the maximum is the maximum CT value of aluminum. (Right) Average radial line profiles of the aluminum inserts. The pCT images on the left are color-marked accordingly as a function of distance from the center.

measured by the 10% to 90% distances at the edges are plotted in Figure 6.11. The spatial resolution of the δ-map indeed improves as a function of distance from the image center similarly with the RSP-map. Furthermore, the graph shows that the δ-map demonstrates a better spatial resolution than the RSP-map for the inserts near the periphery. This is because the contrast for aluminum and water is better with $\delta_{0,Al} = 4.06$ than $\mathrm{RSP}_{\mathrm{Al}} = 2.1$.

6.5 Discussion

We have proposed and characterized an algorithm which integrates a curved most likely path estimate in pCT reconstructions exploiting proton multiple Coulomb scattering. The same method of data processing and image reconstruction was carried out to reconstruct the relative scattering power δ-map of the material. The

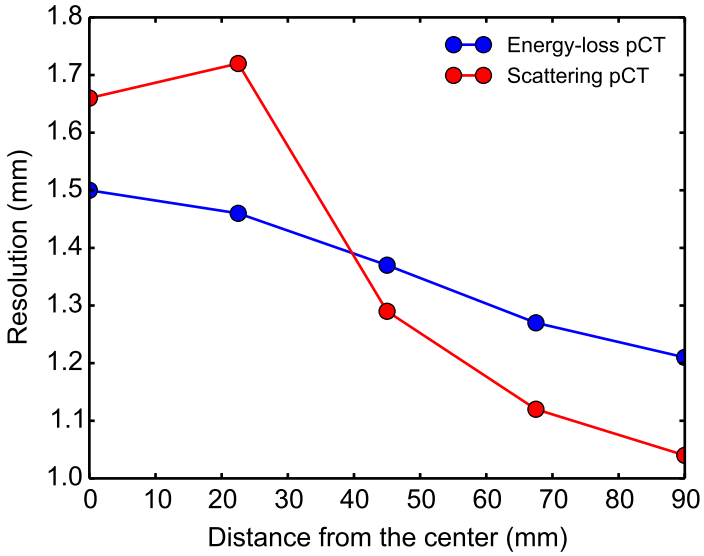

Figure 6.11: Spatial resolution calculated using the 10% - 90% distances of the edge response of the aluminum inserts as a function of distance from the center for pCT reconstructions using the MLP.

accuracy, precision and spatial resolution of the δ-maps were evaluated and compared with the RSP-maps acquired from energy loss pCT.

The accuracy of the reconstructed δ-values depends largely on the proton data used. In theory, both energy-loss and scattering pCT require only primaries without nuclear interactions such that the theory on small angle MCS is valid. In practice a 3-σ both on the angular and energy distributions are imposed for energy-loss pCT. The energy-loss WEPL is then calculated using the average of each WEPL in a given pixel. The imposed cut would improve the calculation of the mean because the secondary particles and primaries with elastic nuclear interactions shifts the distribution towards the low energy. On the other hand, applying the same 3-sigma cuts for proton data used for scattering pCT was found to underestimate the variance at the periphery region. Because of this, a perfect cut was imposed by directly removing those protons that do not conform to the reconstruction model used. There is a need, however, to have a robust way to filter out the protons for scattering pCT.

The strongly varying δ values for materials with high atomic number Z bias the information of the image. Although most of the tissues in the body are near water density, and that δ is almost constant, there are regions in the body containing bone such as in the skull where pCT would be most important. The high contrast that *delta*-maps would provide will supplement RSP-maps even in diagnosis. One solution to address the cupping artifact is by modeling the energy-loss dependence of the scattering angle as constraints and incorporating this model in the iterative reconstruction.

The noise-dose plot shows that the RSP-map demonstrate the best precision among the three pCT modalities. The spatial resolution of the δ is, however, comparable with the RSP-map and in some instances even better at the phantom pe-

riphery.

6.6 Conclusion

We have investigated the feasibility of using the information of proton scattering to reconstruct the δ-map of the object while taking into account a curved proton path. The δ-map is related to the radiation X_0 (or scattering X_s) length of the material and this quantity is also related to two intrinsic properties of the material, i.e. the atomic number (Z) and density (ρ). The preliminary results show that the scattering pCT images could provide an additional information about the material which could be used in combination with the conventional energy-loss proton CT specifically in the lateral dose calculations. The inherent cupping artifact still remains an issue and further treatment planning applications of the method have yet to be explored.

Chapter 7

Conclusion and future work

The need for a precise treatment plan in proton therapy especially in dosimetry triggered a renewed interest to improve proton imaging. The direct acquisition of the RSP with protons using energy loss measurements makes pCT a promising tool to improve dose conformation on the tumor compared with the conventional xCT. Unlike photons, proton interactions in matter are rather complicated and it is for this reason that early proton images failed to address the current clinical demands in treatment planning. One reason is the poor spatial resolution attributed to proton scattering in matter. However, it is also by this complexity that other information beyond the stopping power could be revealed about the material. Reconstructions using quantities other than energy loss has been carried out by (Bopp et al., 2013) and we also further investigated these pCT modalities exploiting the nuclear interactions and multiple Coulomb scattering MCS to reconstruct the nuclear inelastic cross-section (κ) map and the relative scattering power (δ) map of the material. The data used in energy-loss pCT could be reused for the other two pCT modalities. This means that three maps of different quantities could be generated in just a single scan.

Image characterization such as the accuracy, precision and spatial resolution has been investigated and the results were compared to the conventional energy-loss pCT. The results showed that although the RSP maps yield the best performance in terms of accuracy and precision, the spatial resolution of the other pCT was comparable and in some situations even better compared with the conventional RSP maps. Although, it is the RSP map that is needed in treatment planning for dose calculations, the κ and δ maps could supply additional information intrinsic about the material. For instance, tissues having the same RSP would be indistinguishable in the RSP-map, but could be differentiated with the other two maps. This could lead to the use of pCT not only as tool for dosimetry but also for diagnosis. Although the diagnostic application of proton imaging has already been conceived in the past, even before its potential in dosimetry, the amount of information that could be extracted from attenuation pCT and scattering pCT have yet to be explored and validated experimentally.

It has been mentioned that the poor spatial resolution of pCT images compared with xCT limits its potential as a tool that clinicians could use in the treatment planning. However, it has been demonstrated in the past that by modeling the

curved proton path and integrating it in the reconstruction would significantly improve the spatial resolution. We have demonstrated that indeed, by using the MLP a significant improvement has been achieved. One disadvantage of using the MLP is the slow computation time attributed to individual calculations of the path for each proton. Although this could be addressed by using powerful computers and running the reconstruction in parallel, one solution could be the use of a simple yet faster CSP. Trade-offs against accuracy and speed are necessary depending on the demands in the clinical environment.

Proton CT reconstructions are driven by the physics of the reconstruction models or inverse problems. We have derived a formalism to solve for the inverse problem to reconstruct the κ-map and the δ-map. The reconstruction technique used in this study to solve for the inverse problems is based on analytical methods, i.e. the FBP. Although this method is faster than iterative techniques, however, because of the need to integrate a curved proton path in the reconstructions, reconstructions with a curved proton path was limited only to the use of iterative techniques. It has been demonstrated by Rit et al. (2013) that curved proton paths could be integrated in FBP by binning the projection values at different positions from the source defined by the curved model of the path. This technique, also called distance-driven binning was first investigated in energy-loss pCT and we adapt the same algorithm for attenuation pCT and scattering pCT. The precision of the reconstructed maps not only depends on the noise in the measured data but also with the reconstruction algorithm used. For the FBP reconstructions currently implemented, a ramp filter was used. It has been reported in Zhang and Ning (2008) that different reconstruction filters yield different image noise and that the ramp filter gives the highest noise level. This means that the precision of the current reconstructions can still improve, for example by using Shepp-Logan and Cosine filters.

The accuracy and precision of the reconstructed pCT images can also be improved by using iterative techniques. Additional constraints in the forward model may not be possible to integrate in the analytical reconstructions but is possible with an iterative method. For example, the *cupping* artifact in scattering pCT due to the difference in the energy-loss between the material and water at a given angle could be corrected using appropriate models as constraints in the iterative method. This in term would improve the accuracy of the reconstructed values.

The different maps that could be generated in one scan which is an asset of pCT could lead to multivariate reconstructions. For instance, because of the capabilities of κ-maps to distinguish clearly the object boundaries, it could be used to improve or even correct the RSP-maps. A similar method as what is done in phase-contrast imaging could be a solution to make use of the boundary resolving capabilities of the fringes along the borders. While RSP maps will be used as an input for dose calculation, it is only limited to the longitudinal direction or direction of the beam path. The δ-maps could be used to supplement current protocol, by providing information, i.e. the radiation length of the material, for the lateral dose calculation. This would help in treatment planning especially for cases where bone and other dense materials is along the beam path. Lateral scattering of the beam has been a known issue because of the incomplete modeling of MCS in the beam path which also translates to range inaccuracy (Paganetti, 2012). By integrating appropriate dosimetric models, and by using both the RSP and δ maps as inputs, a more reliable

treatment plan would be achieved.

The accuracy of the reconstructed values mainly depends on the proton data used. The particles that are detected after traversing an object are composed of primaries without any nuclear interactions, primaries with elastic interactions, secondary protons and other particles. Different proton data is used depending on the reconstruction model used. For example, in energy loss pCT, a 3 σ cut both in the energy and angular distribution was imposed to cut out majority of the secondaries and primaries with elastic interactions. In theory, the same filtered data sets as with energy-loss pCT should be used for scattering pCT, however, it was found out that the σ cuts was found out to underestimate the variance at the periphery region. This was never an issue with energy-loss pCT as the average value of the energy-loss WEPL was used as the projection, therefore, limiting the width (improved precision) and better accuracy. For scattering pCT, since it is the variance of the angular distribution that is calculated, then an underestimate of the variance at the periphery due to the sigma cut limits the accuracy of the reconstructed δ. In addition, for attenuation pCT, a 10 σ cut was used to only cut out majority of the secondaries while keeping the primaries with nuclear interactions. The 10-σ cut was optimized for a water cylindrical phantom, therefore, inaccuracies could be introduced for inhomogeneous phantoms. Having these limitations, we suggest to improve data selection by implementing a more optimized and robust cut during reconstructions. Another way is to use theoretical models on nuclear interactions to select the protons based on the thickness traversed and the materials involved.

The three pCT modalities investigated make use of the transmitted primary protons. The use of secondary protons to reconstruct the hydrogen map of the material has already been demonstrated even experimentally in the past (Saudinos, 1987). Additional information of this map may help differentiate normal tissues from tumor and could help improve treatment plan.

The proposed methods of reconstruction make use of tracking the individual protons. This also translates to a need for detectors that could cater the demands of the reconstruction models. Various groups dedicated in proton imaging explored different hardware systems. The accuracy and precision of the pCT images would also depend on the electronic noise or systematic error of the hardware. Considering the physics of proton interactions, energy detectors should have a resolution that matches the resolution of the energy straggling as an ensemble of protons traverse a given thickness. This is also true with the spatial resolution of tracking detectors, i.e. it should match the spatial straggling of protons due to multiple Coulomb scattering. Currently, both criteria are still difficult to achieve due to the limitations in the hardware technology and the cost of such detectors.

Moreover, proton imaging is limited to the highest deliverable energy. A pCT acquisition of an average human head (200 cm) would require a 200 MeV incident energy and for an average pelvis (33 cm) would need at least 250 MeV. This may limit pCT to children and non obese people. However, hybrid techniques have been suggested to use xCT data in combination with protons where proton data acquisition is not possible (Hansen et al., 2014).

Although, in theory, the single-tracking approach would yield the best performance over the proton-integrating technique, because of the limitations in hardware

technology, it would also be worth investigating the potential gain in the accuracy and precision for the single-tracking approach in the clinical environment. Moreover, RSP-maps could be generated using DECT. Currently, there is no established accuracy threshold. If in clinical practice the RSP maps generated with non-proton means of RSP acquisition is already sufficient, then pCT imaging should be reconsidered.

Proton imaging is not only limited in the clinical environment. Attenuation based proton imaging has already been used in non-destructive testing. Because of the West-and-Sherwood effect, tiny cracks could be visualized without invasive intervention.

By and large, proton CT could potentially improve treatment planning both in dosimetry and diagnosis. However, it is currently not yet adapted in clinical practice due to constraints in the hardware. The merits it could bring compared with other treatment planning modalities have yet to be explored.

Appendix A

Particle therapy centers

Table A.1: Particle therapy facilities in operation (last update: 8-March-2016).

Country	Who, where	Particle	S/C/SC* Max. energy (MeV)	Beam directions	Start of Treatment
Canada	TRIUMF, Vancouver	p	C 72	1 horiz.	1995
Czech Republic	PTC Czech r.s.o., Prague	p	C 230	3 gantries**, 1 horiz.	2012
China	WPTC, Wanjie, Zi-Bo	p	C 230	2 gantries, 1 horiz.	2004
China	IMP-CAS, Lanzhou	C-ion	S 400/u	1 horiz.	2006
China	SPHIC, Shanghai	p	S 250	3 horiz.**	2014
China	SPHIC, Shanghai	C-ion	S 430/u	3 horiz.**	2014
England	Clatterbridge	p	C 62	1 horiz.	1989
France	CAL, Nice	p	C165	1 horiz.	1991
France	CPO, Orsay	p	S 250	1 gantry, 2 horiz.	1991
Germany	HZB, Berlin	p	C 250	1 horiz.	1998
Germany	RPTC, Munich	p	C 250	4 gantries**, 1 horiz.	2009
Germany	HIT, Heidelberg	p	S 250	2 horiz., 1 gantry**	2009, 2012
Germany	HIT, Heidelberg	C-ion	S 430/u	2 horiz., 1 gantry**	2009, 2012
Germany	WPE, Essen	p	C 230	4 gantries***, 1 horiz.	2013
Germany	PTC, Uniklinikum Dresden	p	C 230	1 gantry**	2014
Germany	MIT, Marburg	p	S 250	3 horiz., 1 45deg.**	2015
Germany	MIT, Marburg	C-ion	S 430/u	3 horiz., 1 45deg.**	2015
Italy	INFN-LNS, Catania	p	C 60	1 horiz.	2002
Italy	CNAO, Pavia	p	S 250	3 horiz., 1 vertical	2011
Italy	CNAO, Pavia	C-ion	S 480/u	3 horiz., 1 vertical	2012
Italy	APSS, Trento	p	C 230	2 gantries**, 1 horiz.	2014
Japan	HIMAC, Chiba	C-ion	S 800/u	horiz.***, vertical***	1994
Japan	NCC, Kashiwa	p	C 235	2 gantries***	1998
Japan	HIBMC, Hyogo	p	S 230	1 gantry	2001
Japan	HIBMC, Hyogo	C-ion	S 320/u	horiz.,vertical	2002
Japan	PMRC 2, Tsukuba	p	S 250	2 gantries***	2001
Japan	Shizuoka Cancer Center	p	S 235	3 gantries, 1 horiz.	2003
Japan	STPTC, Koriyama-City	p	S 235	2 gantries**, 1 horiz.	2008
Japan	GHMC, Gunma	C-ion	S 400/u	3 horiz., 1 vertical	2010
Japan	MPTRC, Ibusuki	p	S 250	3 gantries***	2011
Japan	Fukui Prefectural Hospital PTC, Fukui City	p	S 235	2 gantries***, 1 horiz.	2011
Japan	Nagoya PTC, Nagoya City, Aichi	p	S 250	2 gantries***, 1 horiz.	2013
Japan	SAGA-HIMAT, Tosu	C-ion	S 400/u	3 horiz., vertical, 45 deg.	2013
Japan	Aizawa Hospital PTC, Nagano	p	C 235	1 gantry	2014
Japan	i-Rock Kanagawa Cancer Center, Yokohama	C-ion	S 430/u	4 horiz., 2 vertical	2015

Table A.2

Poland	IFJ PAN, Krakow	p	C 60	1 horiz.	2011
Russia	ITEP, Moscow	p	S 250	1 horiz.	1969
Russia	St.Petersburg	p	S 1000	1 horiz.	1975
Russia	JINR 2, Dubna	p	C 200****	1 horiz.	1999
South Africa	NRF - iThemba Labs	p	C 200	1 horiz.	1993
South Korea	KNCC, IIsan	p	C 230	2 gantries, 1 horiz.	2007
Sweden	The Skandion Clinic,Uppsala	p	C 230	2 gantries**	2015
Switzerland	CPT, PSI, Villigen	p	C 250	2 gantries*****, 1 horiz.	1984, 1996, 2013
Taiwan	Chang Gung Memorial Hospital, Taipei	p	C 230	4 gantries***, 1 horiz. exp.	2015
USA, CA.	J. Slater PTC, Loma Linda	p	S 250	3 gantries, 1 horiz.	1990
USA, CA.	UCSF-CNL, San Francisco	p	C 60	1 horiz.	1994
USA, MA.	MGH Francis H. Burr PTC, Boston	p	C 235	2 gantries***, 1 horiz.	2001
USA, TX.	MD Anderson Cancer Center, Houston	p	S 250	3 gantries***, 1 horiz.	2006
USA, FL.	UFPTI, Jacksonville	p	C 230	3 gantries, 1 horiz.	2006
USA, OK.	ProCure PTC, Oklahoma City	p	C 230	1 gantry, 1 horiz, 2 horiz/60 deg.	2009
USA, PA.	Roberts PTC,UPenn, Philadelphia	p	C 230	4 gantries***, 1 horiz.	2010
USA, IL.	Chicago Proton Center, Warrenville	p	C 230	1 gantry, 1 horiz, 2 horiz/60 deg.	2010
USA, VA.	HUPTI, Hampton	p	C 230	4 gantries, 1 horiz.	2010
USA, NY.	ProCure Proton Therapy Center, New Jersey	p	C 230	4 gantries***	2012
USA, WA.	SCCA ProCure Proton Therapy Center, Seattle	p	C 230	4 gantries***	2013
USA, MO.	S. Lee Kling PTC, Barnes Jewish Hospital, St. Louis	p	SC 250	1 gantry	2013
USA, TN.	Provision Center for Proton Therapy, Knoxville	p	C 230	3 gantries**	2014
USA, CA.	Scripps Proton Therapy Center, San Diego	p	C 250	3 gantries**, 2 horiz.**	2014
USA, LA.	Willis Knighton Proton Therapy Cancer Center, Shreveport	p	C 230	1 gantry**	2014
USA, FL.	Ackerman Cancer Center, Jacksonville	p	SC 250	1 gantry	2015
USA, TX.	Texas Center for Proton Therapy, Irving	p	C 230	2 gantries**, 1 horiz.	2015
USA, TN.	St. Jude Red Frog Events Proton Therapy Center, Memphis	p	S 220	2 gantries**, 1 horiz.	2015
USA, MD.	Maryland Proton Treatment Center, Baltimore	p	C 250	3 gantries**, 2 horiz.**	2016

* S/C = Synchrotron (S) or Cyclotron (C) or SynchroCyclotron (SC)
** with beam scanning
*** with spread beam and beam scanning
**** degraded beam

Table A.3: Particle therapy facilities under construction.

Country	Who, where	particle	S/C/SC* Max. energy (MeV)	Beam directions	No. of treatment rooms	Planned start of treatment
Austria	Med-AUSTRON	p, C-ion	S 430/u	1 gantry (for protons), 1 horiz.fixed beam, 1 fixed beam 0 + 90 deg	3	2016
China	HITFil, Lanzhou	C-ion	S 400/u	4 horiz, vertical, oblique, fixed beams	4	2016
China	Rui Jin Hospital, Jiao Tong University, Shanghai	p	S 250	2 gantries, 1 horiz. fixed beam	3	2018
China	Beijing Proton Center, Beijing	p	C 230	3 gantries, 1 horiz. fixed beam	4	2018?
Denmark	DCPT, Aarhus	p	SC 250	3 gantries, 1 horiz. fixed beam	4	2018
France	Centre Antoine Lacassagne, Nice	p	SC 230	1 gantry	1	2016
India	Apollo Hospitals PTC, Chennai	p	C 230	2 gantries, 1 horiz. fixed beam	3	2018
Japan	PBTC, Hokkaido Univ. Hospital, Sapporo	p	S 220	1 gantry	1	2016
Japan	Hakuhokai Group Osaka Proton Therapy Clinic, Osaka	p	S 235	1 gantry	1	2016
Japan	Tsuyama Chuo Hospital PTC, Okayama	p	S 235	1 gantry	1	2016
Netherland	HollandPTC, Delft	p	SC 250	2 gantries, 1 horiz. fixed beam	3	2017
Netherland	UMC Groningen PTC, Groningen	p	SC 230	2 gantries	2	2017
Poland	IFJ PAN, Krakow	p	C 230	2 gantries, 1 horiz. fixed beam	3	2016
Russia	PMHPTC, Protvino	p	S 250	1 horiz. fixed beam	1	2017?
Saudi Arabia	King Fahad Medical City PTC, Riyahdt	p	SC 250	4 gantries	4	2016
Slovak Rep	CMHPTC, Ruzomberok	p	S 250	1 horiz. fixed beam	1	2017?
South Korea	Samsung Proton Center, Seoul	p	C 230	2 gantries	2	2016

S/C = Synchrotron (S) or Cyclotron (C) or SynchroCyclotron (SC)

Appendix B

Résumé éntendu

1 Introduction

L'utilisation de protons dans le traitement du cancer a été largement promue en raison du parcours fini (stopping range) des protons dans la matière. Dans la planification du traitement par proton thérapie, l'incertitude dans la détermination du parcours provient principalement de l'inexactitude dans la conversion des unités Hounsfield (HU) obtenues à partir de tomodensitométrie par rayons X (xCT) en pouvoir d'arrêt du proton. La tomographie proton (pCT) a été une solution prometteuse pour estimer directement le pouvoir d'arrêt relatif (RSP) de l'objet. La technique de pCT conventionnelle est basée sur des mesures de la perte d'énergie des protons pour reconstruire l'image du RSP de l'objet. En plus de la perte d'énergie, les protons subissent également la diffusion multiple de Coulomb (MCS) et des interactions nucléaires qui pourraient révéler d'autres propriétés intéressantes des matériaux, non visibles avec les cartes de RSP.

Ce travail de thèse a consisté à étudier les interactions de protons par simulations Monte Carlo (MC) par GATE et d'utiliser ces informations pour reconstruire une carte de l'objet par rétroprojection filtrée (filtered back-projection, FBP) sur des chemins de protons les plus probables (most likely paths, MLP). Mise à part la pCT conventionnelle par perte d'énergie, deux modalités de pCT ont été étudiées et réalisées. La première est appelée tomographie proton par atténuation qui est réalisée en utilisant l'atténuation des protons pour la reconstruction du coefficient d'atténuation linéique inélastique de l'objet. La seconde modalité est appelée tomographie proton par diffusion qui est réalisée en mesurant la variation angulaire de la diffusion de protons pour reconstruire le pouvoir de diffusion relatif qui est lié à la longueur de radiation de la matière. La justesse, la précision et la résolution spatiale des images reconstruites à partir des deux modalités de pCT ont été évaluées qualitativement et quantitativement et comparées avec la tomographie proton conventionnelle par perte d'énergie.

Le manuscrit est structuré comme suit: le chapitre 1 et le chapitre 2 sont des revues approfondies de la littérature sur la proton-thérapie et sur l'imagerie du proton qui a conduit au travail réel ; le chapitre 3 se concentre sur l'étude des processus physiques des interactions des protons dans la matière ainsi que sur la validation Monte Carlo (MC) des processus ; le chapitre 4 décrit la technique de pCT

par perte d'énergie pour reconstruire la carte de RSP ; le chapitre 5 décrit la pCT par atténuation pour reconstruire l'image de section efficace nucléaire inélastique ; le chapitre 6 décrit les méthodes de pCT par diffusion pour reconstruire le pouvoir de diffusion relatif et enfin le chapitre 7 présente la conclusion et les perspectives de l'étude.

2 Protons pour le traitement du cancer

La radiothérapie ou le traitement par radiothérapie est une procédure non invasive dans le traitement du cancer. L'objectif de la radiothérapie est de transmettre une dose efficace maximale au volume de la tumeur tandis que les tissus sains environnants devraient recevoir une dose minimale. Les différentes sources de rayonnement interagissent différemment dans les tissus humains et affectent par conséquent l'efficacité du traitement. La radiothérapie conventionnelle utilise des faisceaux de rayons x de hautes énergies pour endommager les cellules cancéreuses. Le potentiel de l'utilisation des protons et des ions lourds en radiothérapie a été proposée par Wilson (1946) après avoir découvert que les protons et les ions lourds déposent une dose maximale, aussi appelé le pic de Bragg, à une profondeur précise dans un tissu. Non seulement le volume de la tumeur reçoit la dose maximale, mais surtout, les tissus sains environnants reçoivent une quantité minimale de la dose. Le traitement conformationnel est obtenu en positionnant le pic de Bragg de telle sorte qu'il touche le volume de la tumeur, soit en faisant varier l'énergie des protons incident soit en plaçant devant le patient des modulateurs de parcours le long du faisceau.

Les expériences sur les propriétés physiques et radiobiologiques des faisceaux de protons ont été étudiées dès 1948 au Lawrence Berkeley Laboratory aux États-Unis en 1946 et leurs premiers patients atteints de cancer ont finalement été traités avec des faisceaux de protons en 1955 (Tobias et al., 1958). En dépit du potentiel prometteur de la thérapie par particules dans le traitement du cancer, les avantages ne pouvaient pas être utilisés efficacement dès le départ en raison des limites de l'imagerie du patient et de la délivrance de faisceau. Le coût pour construire des accélérateurs de protons quand il a été proposé a entravé ses vastes applications cliniques. Cependant, au cours des quinze dernières années, avec les progrès en technologie d'accélérateur combinés à la réduction des coûts opérationnels, les hôpitaux du monde entier adoptent cette technologie pour traiter les patients atteints de cancer qui bénéficient le plus de l'avantage de la dose en profondeur en proton-thérapie.

Les incertitudes inhérentes à la radiothérapie conventionnelle, qui comprennent des variations géométriques, le positionnement du patient et le mouvement d'organes, sont également présentes dans la proton-thérapie. Cependant, il existe une importante source d'incertitude spécifique à la proton-thérapie, c'est-à-dire l'estimation du parcours de protons. Actuellement, les images tomographiques de RSP sont réalisées à l'aide de tomodensitométrie par rayons X (xCT) pour générer une carte d'atténuation de l'objet. La carte d'atténuation des photons est ensuite convertie en RSP proton en utilisant une courbe de calibrage stœchiométrique basée sur des mesures en utilisant des matériaux équivalents tissus (Schneider et al., 1996). Toute-

fois, cette procédure s'est révélée inexacte car elle conduit à une erreur d'environ 0,8% (Matsufuji et al., 1998; Chvetsov and Paige, 2010) et à 3% du parcours du proton (Schaffner and Pedroni, 1998; Paganetti, 2012; Yang et al., 2012). Idéalement, pour un plan de traitement précis, on devrait avoir une modalité d'imagerie qui soit en mesure d'acquérir directement une carte de pouvoir d'arrêt de l'objet. C'est pour cette raison que l'imagerie proton a été une solution intéressante pour réduire les incertitudes dans la détermination du RSP.

3 Protons pour l'imagerie médicale

L'idée d'utiliser des faisceaux de protons pour l'imagerie a été proposée dès 1963 (Cormack, 1963). Les algorithmes conventionnels de reconstruction pCT exploitent la perte d'énergie des protons pour reconstruire directement la carte de RSP de l'objet. Cependant, les premières images pCT ont une faible résolution spatiale en raison de la diffusion inhérente des protons en traversant un milieu (Schneider and Pedroni, 1994). À cause de cela et du coût élevé dans la construction de détecteurs de protons, les activités de recherche sur la pCT ont presque cessé pendant un certain temps en faveur de la xCT. Ce n'est qu'au début 1990 que la nécessité d'un plan de traitement précis, stimulée par l'intérêt croissant pour la proton-thérapie, a déclenché une forte volonté d'améliorer la vérification du parcours et du positionnement du patient pour une utilisation dans la pratique clinique. En raison des exigences pour une dosimétrie précise, les travaux de recherche sur l'imagerie par protons ont été axés sur l'exploitation de la technique par perte d'énergie.

Une solution pour répondre à la faible résolution spatiale des images de pCT est d'utiliser un trajet de protons courbe au lieu de l'approcher comme un trajet en ligne droite (SLP) lors de la reconstruction. Une estimation du trajet le plus probable (MLP) en utilisant des détecteurs de passage de particules avant et après que l'objet a été étudié (Williams, 2004; Schulte et al., 2008; Erdelyi, 2009) pour modéliser la trajectoire courbe des protons dans un milieu homogène. Il a été découvert que l'incorporation d'un trajet courbe de protons a montré une amélioration significative de la résolution spatiale des images pCT Li et al. (2006).

4 Physique des interactions de protons dans la matière

L'interaction du proton à l'intérieur d'un objet implique deux processus: électromagnétique et nucléaire. Quand une particule chargée, comme un proton, traverse la matière, il interagit avec les électrons du milieu par l'intermédiaire de collisions. Les interactions électromagnétiques (EM) induisent le MCS sur le proton au moyen duquel les protons perdent de l'énergie en continu et sont diffusés dans des directions stochastiques (Gottschalk et al., 1993). La variation de la perte d'énergie du proton par unité de longueur, c'est-à-dire le pouvoir d'arrêt, augmente à mesure que le proton ralentit et dépend de l'énergie cinétique et du matériau. Par conséquent, pour les applications pCT, l'énergie cinétique incidente des protons doit être assez grande pour que les protons puissent traverser l'objet. Le pouvoir d'arrêt peut alors être

utilisé pour calculer le parcours des protons. Une bonne estimation du parcours des protons à partir de différentes modalités d'imagerie a été un sujet d'intérêt pour améliorer la planification du traitement en proton-thérapie (Arbor et al., 2015).

Mises à part les interactions EM, les protons sont également soumis à des interactions avec les noyaux atomiques du milieu. Les interactions nucléaires sont de deux types, élastiques et inélastiques (ICRU63). Puisque les deux types d'interactions peuvent forcer les protons à diffuser aux grands angles, ils peuvent aussi être appelés diffusion nucléaire. La diffusion élastique est une réaction dans laquelle le projectile d'impact continue sa course hors du noyau cible, avec l'énergie cinétique totale conservée. D'autre part, la diffusion inélastique se produit lorsqu'un proton est absorbé puis à nouveau émis (le noyau cible absorbe de l'énergie à l'intérieur et il est laissé dans un état excité).

5 Tomographie proton par perte d'énergie

Nous commençons par explorer la méthode pCT par perte d'énergie de Rit et al. (2013) incorporant le chemin le plus probable $\mathbf{\Gamma}(w)$ à une distance de la source à travers un regroupement de pixels modulé par la distance. Le problème inverse pour la pCT par perte d'énergie est donné par,

$$-\int_{E^{in}}^{E^{out}} \frac{\mathrm{d}E(\mathbf{\Gamma}(w))}{S_{\text{water}}(E(\mathbf{\Gamma}(w)))} = \int_0^l \frac{S(\mathbf{\Gamma}(w), E(\mathbf{\Gamma}(w)))}{S_{\text{water}}(E(\mathbf{\Gamma}(w)))} \mathrm{d}\mathbf{\Gamma}\,(w) \tag{B.1}$$

où S_{water} est le pouvoir d'arrêt (dépendant de l'énergie) du proton dans l'eau, E^{in} et E^{out} sont les énergies d'entrée et de sortie, respectivement, et l est l'épaisseur du matériau. Le côté gauche de l'équation 1 est la longueur équivalente dans l'eau (WEPL) tandis que le côté droit est l'intégrale du RSP $= S_{\text{mat}}/S_{\text{water}}$ le long du chemin des protons.

À partir de ces chemins, chaque WEPL par paire de proton est rééchantillonné en radiographies virtuelles à des distances différentes w à partir de la source en utilisant l'algorithme de regroupement piloté par la distance de Rit et al. (2013). Les valeurs finales de projection sont les valeurs moyennes du WEPL par pixel. La projection pilotée par la distance est ensuite calculée pour chaque position de source et la reconstruction de l'image de RSP est alors réalisée en utilisant le même algorithme de reconstruction que Rit et al. (2013), c'est-à-dire l'algorithme FDK (Feldkamp et al., 1984) adapté avec une rétroprojection spécifique à chaque voxel en sélectionnant la distance w en fonction de la distance entre le voxel et le détecteur de sortie pour chaque position de source.

La relation dose-bruit a également été étudiée suivant les travaux de Schulte et al. (2005).

6 Tomographie proton par atténuation

Mise à part la perte d'énergie en traversant un objet, les protons sont également soumis à des interactions nucléaires provoquant une atténuation de la fluence des

protons incidents. Malheureusement, seules quelques études exploitant l'atténuation des protons dans la gamme d'énergie pour l'imagerie médicale ont été menées dans le passé. Une raison pourrait être le taux de transmission élevé de protons à travers les tissus humains et, par conséquent, le faible rapport signal/bruit (SNR) d'atténuation pCT (Bopp et al., 2013). En outre, bien qu'il y ait eu des études exploitant l'atténuation de proton en radiographie (Plautz et al., 2014) et tomographie (Bopp et al., 2013), il n'y a eu aucune tentative encore d'intégrer le chemin de protons courbe en utilisant le modèle MLP lors de la reconstruction. Dans ce chapitre, nous présentons une méthode d'atténuation pCT intégrant le MLP au sein de l'algorithme FBP par l'échantillonnage des projections piloté par la distance proposé par Rit et al. (2013) tel que décrit dans le chapitre 4.

6.1 Théorie

Un faisceau de protons peut être caractérisé par sa fluence Φ définie comme étant le nombre de protons $\mathrm{d}N$, lors d'une exposition ou d'un traitement donné, traversant un élément infinitésimal de la zone $\mathrm{d}A$ perpendiculaire à la direction du faisceau $\Phi = \mathrm{d}N/\mathrm{d}A$. Nous supposons que seules les interactions nucléaires inélastiques suppriment les primaires du faisceau incident, par conséquent, l'atténuation de la fluence primaire. Quand un faisceau de protons avec une fluence initiale Φ^{in} au niveau du détecteur d'entrée traverse un objet et en supposant que tous les protons suivent le même chemin $\mathbf{\Gamma}$ et que la section transversale nucléaire inélastique est indépendante de l'énergie des protons, la fluence primaire diminue de façon exponentielle en fonction de la loi exponentielle décrite par

$$\Phi^{out} = \Phi^{in} \exp\left(- \int_{w^{in}}^{w^{out}} \kappa(\mathbf{\Gamma}(w)) \mathrm{d}\mathbf{\Gamma}(w) \right) \tag{B.2}$$

où κ est l'image 3D du coefficient d'atténuation linéique macroscopique des interactions inélastiques nucléaires des protons dans un matériau (Schulte et al., 2005; Bopp et al., 2013) et Φ^{out} est la fluence de protons détectée par le détecteur du passage de particule en position w^{out}.

En utilisant l'algorithme d'échantillonnage des projections piloté par la distance, la valeur de chacune des projections pour une paire de protons est indexée par rapport à des positions différentes dans l'espace défini par le MLP. La même technique a été appliquée ici sauf que les protons ont été comptés au cours de leur regroupement piloté par la distance au lieu de faire la moyenne des WEPL par perte d'énergie. Comme la diffusion de protons est tridimensionnelle par nature, la fluence est calculée en considérant les protons qui sont passés par la même position 3D dans l'espace pour une distance donnée w.

Nous avons également exploré la relation dose-bruit de la méthode pCT par atténuation suivant le formalisme de Gore and Tofts (1978) et Schulte et al. (2005).

6.2 Des expériences de simulation

Un système pCT a été simulé à l'aide de GATE v7.1 (Jan et al., 2011) pour évaluer la précision de la nouvelle méthode de pCT par atténuation incorporant le

MLP. La configuration est composée d'une source de rayonnement, d'un fantôme et de deux détecteurs idéaux de passage de particule. Un total de 360 angles de projection à intervalles réguliers a été simulé. La liste physique QGSP_BIC de Geant4.10.01.p02 et une limite de taille de pas de protons de 1 mm ont été utilisées à des fins de simulation MC tout au long de cette étude.

Pour valider la relation dose-bruit des approches par perte d'énergie et par atténuation, nous avons utilisé un fantôme cylindrique avec un diamètre de 20 cm rempli d'eau. Les énergies utilisées pour les protons incidents étaient de 200 MeV et de 300 MeV, ce qui permet de traverser facilement 20 cm d'eau homogène. Deux acquisitions pCT ont été réalisées (1) en utilisant la perte d'énergie pour générer une image de RSP et (2) en utilisant l'atténuation pour générer une image d'atténuation.

La précision de la méthode de reconstruction a été évaluée en utilisant le Gammex® 467 qui a un diamètre de 33 cm approchant la taille d'un bassin humain moyen et consistant en une matrice de seize trous de 2,8 cm de diamètre de divers matériaux équivalent tissus et eau. Une dose totale d'environ 50 mGy au centre du fantôme a été considérée.

Afin d'évaluer qualitativement la résolution spatiale de la méthode d'imagerie, le fantôme haute résolution Catphan® 528 a été utilisé, lequel est constitué d'un cylindre d'eau de 20 cm avec 21 motifs de ligne de plaques d'aluminium de 22 mm d'épaisseur. Un faisceau incident de protons de 200 MeV et une dose d'environ 50 mGy au centre ont été considérés. Deux voies ont été envisagées lors de la reconstruction: (1) le MLP utilisant les projections avec un échantillonnage piloté par la distance et (2) le SLP en utilisant uniquement les projections de sortie.

La résolution spatiale de la méthode d'imagerie a été étudiée en fonction de la distance au centre de l'image reconstruite. Cette étude a été menée sur un fantôme cylindrique de 20 cm de diamètre de matériau équivalent eau avec 21 inserts en aluminium de 15 mm de diamètre et disposés régulièrement sur des branches en spirales.

6.3 Résultats et discussion

Nous avons proposé et caractérisé un algorithme qui intègre le chemin courbe le plus probable dans les reconstructions pCT en exploitant l'atténuation de proton. Alors que l'algorithme de reconstruction est le même pour la tomographie par perte d'énergie et la tomographie par atténuation, des différences ont été observées en raison de la nature des données de projection.

Premièrement, la dépendance énergétique de la précision a été étudiée en utilisant un fantôme d'eau cylindrique homogène. Il a été démontré par Schulte et al. (2008) pour les reconstructions pCT en utilisant la perte d'énergie qu'une énergie incidente de 175 MeV montre une meilleure précision qu'un faisceau incident de protons de 200 MeV. La différence entre ces énergies n'est toutefois pas significative en pCT par atténuation, dans laquelle la variation de κ entre ces énergies est presque négligeable. Cependant, l'apparition d'un artefact dit de cape a été observé pour l'image reconstruite d'atténuation κ en utilisant des protons incidents avec une énergie cinétique plus faible, comme par exemple 175 MeV. Ceci est tout à fait attendu puisque les protons d'énergie inférieure subissent une plus grande diffu-

sion inélastique nucléaire dans les régions où de larges épaisseurs de matériaux sont traversées, telles que le centre ; les protons sont ainsi plus atténués, provoquant une surestimation de κ. L'effet est donc opposé au durcissement de faisceau en xCT (effet dit de coupe). Cet artefact de cape est réduit en augmentant l'énergie incidente. Par conséquent, pour la tomographie par atténuation, les énergies résiduelles d'au moins 100 MeV sont nécessaires pour éviter des artefacts d'inhomogénéité.

La précision des images pCT est également influencée par la nature des interactions de protons à l'intérieur d'un objet. Au cours d'une diffusion inélastique, le proton perd toute son énergie au noyau cible, ce qui donc induit une atténuation de fluence de protons. Cette interaction provoque la fragmentation ou l'excitation du noyau cible induisant la production de secondaires parmi lesquels une majorité de protons. Une fraction de l'atténuation est due à l'interaction nucléaire élastique dans laquelle un proton primaire est diffusé aux grands angles. Dans certains cas, des protons avec des interactions nucléaires élastiques ne sortent pas avec succès de l'objet. La probabilité de ces événements dépend aussi de l'épaisseur du matériau. L'impact de l'atténuation des primaires due à la diffusion élastique sur les images d'atténuation κ explique en partie la surestimation des valeurs reconstruites. Par conséquent, en plus de la composante inélastique dans l'atténuation κ, il existe une composante due à des événements nucléaires élastiques qui est dépendante de l'épaisseur et de l'énergie des protons. En outre, la précision est meilleure avec images de RSP par rapport aux images de κ parce que certains primaires élastiques échappent au fantôme, mais ne sont pas mesurés par le détecteur et certains secondaires ne sont pas éliminés.

Un autre aspect important qui influe sur la précision en pCT est la sélection des données. Pour la tomographie proton par perte d'énergie, une coupe de trois écarts-types à la fois sur l'énergie et sur les distributions angulaires a été appliquée en routine standard pour éliminer les secondaires et les primaires ayant subi une diffusion élastique. Cette procédure est cependant basée sur l'hypothèse d'un fantôme homogène. Dans le cas d'un fantôme hétérogène, les pixels où il y a deux ou plusieurs matériaux, les distributions d'énergie pourraient être représentées par le chevauchement de plusieurs distributions gaussiennes (Krah et al., 2015) et la forme des distributions dépend des densités des matériaux impliqués. Cela rendrait inexactes les hypothèses qui ont été formulées pour la simplification du problème de reconstruction. Dans la pCT par atténuation, seuls les secondaires doivent être filtrés, ce qui nous a amené à l'utilisation d'une coupe à 10 écarts-types. Cette coupe n'a été imposée qu'à la distribution angulaire parce que la distribution d'énergie est fortement influencée par l'effet de West-Sherwood causé par des protons qui traversent des matériaux différents et qui sont détectés dans le même pixel. Dans la pCT par atténuation, les données de projection sont basées sur les comptages par pixel et les coupes en écart-type imposantes sur la distribution d'énergie pourraient influencer les valeurs d'atténuation κ près des bords. Ceci n'est pas observé dans la pCT par perte d'énergie parce que les données de projection sont la moyenne des valeurs de projection. Même si des coupure plus importantes sont utilisées, l'effet des coupures imposées à ces distributions non gaussiennes affecte les valeurs κ reconstruites. Il est toutefois nécessaire de développer un algorithme qui pourrait déterminer les coupes appropriées pour filtrer les protons qui ne sont pas conformes aux modèles de reconstruction utilisés pour chaque modalité pCT.

La précision des images pCT à des doses variables a également été étudiée. Une précision considérablement meilleure est observée pour les images de RSP que les images κ. Bien que le dispersion énergétique des protons lors de la traversée d'un milieu limite la précision des images de RSP, les protons d'énergie inférieure ont un avantage bruit-dose par rapport aux protons de grande énergie. Pour la pCT par atténuation, la précision est influencée par les statistiques de comptage des protons incidents.

Étant donné que le bruit de Poisson s'améliore avec la fluence en protons incidents, une dose plus élevée serait nécessaire pour acquérir une image qui serait utile pour la planification du traitement. Une limite de dose n'a pas encore été établie pour la pCT clinique ; toutefois, Schulte et al. (2004) ont suggéré une dose maximale de 50 mGy par examen. Dans les expériences de simulation qui ont été réalisées, une dose de 50 mGy a été fixée pour les protocoles d'acquisition des différents fantômes et avec ce niveau de dose, le bruit est dominant.

La résolution spatiale des images CT reconstruites avec différentes estimations de chemin a également été évaluée. Il est constaté que les images reconstruites avec des trajectoires courbes (MLP) montrent une résolution spatiale améliorée par rapport aux images CT reconstruites avec des chemins droits, à la fois pour la tomographie par perte d'énergie et la tomographie par atténuation. De plus, les images de pCT par atténuation montrent une amélioration dans la visibilité des bords des inserts. Cette caractéristique intéressante de l'atténuation pCT est l'occurrence de l'effet West-Sherwood ce qui cause des sous-évaluations et des sur-évaluations aux limites entre deux matériaux. L'effet constaté est causé par la différence de diffusion des protons le long des limites entre des matériaux ayant un contraste élevé en densité. L'effet West-Sherwood est très fort dans l'image d'atténuation κ reconstruite en utilisant le modèle de SLP. Il améliore la résolution aux bords du fantôme, mais son interaction avec les motifs de ligne dégrade fortement leur visibilité. De plus, contrairement à la réduction de visibilité des motifs de lignes dans les images de RSP à haute fréquence spatiale, leur amplitude est presque invariant dans l'image d'atténuation κ. En effet, le modèle de MLP corrige entièrement la diffusion multiple de Coulomb (MCS) au bord du fantôme et par conséquent corrige l'effet West-Sherwood puisque le fantôme a été simulé dans le vide et que les détecteurs de suivi étaient considérés comme parfaits. Il existe cependant une erreur résiduelle dans l'estimation du MLP qui augmente avec la profondeur dans le fantôme ce qui laisse une partie de l'effet West-Sherwood et améliore la résolution spatiale. Une autre différence remarquable entre l'image de RSP et l'image d'atténuation κ est la dépendance de la résolution spatiale à la distance au centre du fantôme. Alors que l'incertitude résiduelle croissante du MLP avec la distance à la périphérie limite la résolution spatiale de la tomographie par perte d'énergie, on peut observer qu'il se comporte à l'inverse de la tomographie par atténuation grâce à l'effet West-Sherwood. Cet effet d'amélioration de bord est donc un atout pour sonder les petites structures et résoudre les limites près des organes à risque en combinaison avec l'image de pouvoir d'arrêt relatif RSP.

6.4 Conclusions

Nous avons présenté une méthode de reconstruction pCT en utilisant l'atténuation des protons en implémentant l'estimation de MLP par l'échantillonnage des projections piloté par la distance. Les résultats montrent que l'incorporation d'une trajectoire courbe lors de la reconstruction améliore de manière significative la résolution spatiale par rapport aux trajectoires rectilignes, non seulement pour la pCT par perte d'énergie mais aussi pour la CT par atténuation. Il a également été observé qu'il existe une occurrence d'un artefact dit de cape pour les reconstructions présentant des énergies résiduelles de protons inférieures à 100 MeV. Nous avons dérivé et validé une formule analytique pour quantifier la précision dans la reconstruction de CT par atténuation et la relation dose-bruit est au moins 250 fois mieux avec les images de RSP qu'avec les images de κ. Bien que cet aspect soit important dans l'imagerie pour les applications en radiothérapie et que cela ne soit pas en faveur de la pCT par atténuation, l'amélioration en résolution spatiale peut jouer un rôle important. Un mérite des images κ sur les images RSP est la meilleure résolution spatiale dans certaines situations grâce à l'effet West-Sherwood, une caractéristique intéressante pourrait ainsi être de combiner la pCT par atténuation avec la pCT par perte d'énergie.

7 Tomographie proton par diffusion

Dans ce chapitre, nous poursuivons plus profondément l'utilisation d'autres informations issues des interactions proton que la perte d'énergie et l'atténuation en considérant la variance de l'angle de diffusion MCS après avoir traversé un objet. Nous appelons cette modalité d'imagerie pCT par diffusion et nous adaptons le même algorithme utilisé dans les modalités pCT précédentes pour reconstruire l'image du pouvoir de diffusion relative δ de l'objet. Les résultats de la pCT par diffusion ont ensuite été comparés avec ceux des pCT par perte d'énergie et par atténuation.

7.1 Theory

Le problème inverse pour la pCT par diffusion est similaire à celui de la pCT par perte d'énergie. Au lieu de convertir la perte totale d'énergie détectée par pixel en longueur-équivalente-eau (WEPL) au sens de la perte d'énergie, la variance de la distribution angulaire de sortie est convertie WEPL au sens de la diffusion. Par conséquent, le problème inverse est donné par,

$$\int_0^{A^{out}} \frac{\mathrm{d}A(\mathbf{\Gamma}(w))}{\tau_{\text{water}}(A(\mathbf{\Gamma}(w)))} = \int_0^{l} \frac{\tau(\mathbf{\Gamma}(w), A(\mathbf{\Gamma}(w)))}{\tau_{\text{water}}(A(\mathbf{\Gamma}(w)))} \mathrm{d}\mathbf{\Gamma}(w) \tag{B.3}$$

où $A^{out} = \sigma^2_{\theta^{out}}$ est la variance A de la distribution angulaire des protons de sortie après avoir traversé le matériau et τ est le pouvoir de diffusion du matériau.

La déviation angulaire dans les deux directions perpendiculaires à la direction du faisceau ont été regroupées à différentes distances de la source définie par le MLP. La variance de la distribution angulaire échantillonnée a ensuite été calculée à la fin de chaque acquisition. Les projections à échantillonnage piloté par la distance sont les

WEPL (au sens de la diffusion) de la variance angulaire calculée. La reconstruction d'image a ensuite été réalisée à l'aide de FDK.

Nous avons également exploré le bruit au centre d'une image de pouvoir de diffusion relative δ en fonction de la dose au centre.

7.2 Des expériences de simulation

Les mêmes ensembles de données brutes que ceux des expériences de simulation présentés au chapitre 5 ont été utilisés pour décrire la justesse, la précision et la résolution spatiale des images de δ. Une coupure parfaite a également été imposée à la sélection des données.

7.3 Résultats et discussion

Nous avons proposé et caractérisé un algorithme qui intègre une estimation de trajectoire courbe dans les reconstructions pCT en exploitant la diffusion multiple de Coulomb. Les mêmes méthodes de traitement de données et de reconstruction d'image ont été utilisées pour estimer l'image du pouvoir relatif de diffusion δ du matériau. La justesse, la précision et la résolution spatiale des cartes δ ont été évaluées et comparées avec les images de RSP acquises en pCT par perte d'énergie.

La précision des valeurs de δ reconstruites dépend en grande partie des données des protons utilisées. En théorie, les tomographies par perte d'énergie et par diffusion ne nécessitent que des protons primaires sans interaction nucléaire de telle sorte que la théorie MCS sur la diffusion aux petits angles reste valide. Dans la pratique, une coupure à trois écarts-types à la fois sur les distributions angulaires et sur l'énergie est imposée pour la tomographie proton par perte d'énergie. La WEPL au sens de la perte d'énergie est ensuite calculée en utilisant la moyenne de chaque WEPL dans un pixel donné. La coupure imposée permet d'améliorer le calcul de la moyenne parce que les particules secondaires et primaires avec des interactions nucléaires élastiques biaise la distribution vers les faibles énergies. D'autre part, le fait d'appliquer les mêmes coupures pour les données de protons utilisées pour la pCT par diffusion a tendance à sous-estimer la variance dans la région de la périphérie. À cause de cela, une coupure parfaite a été imposée en supprimant directement les protons qui ne sont pas conformes au modèle de reconstruction utilisé. Il est nécessaire, cependant, d'avoir un moyen robuste pour filtrer les protons pour la pCT par diffusion.

Les valeurs de δ très variables pour les matériaux avec un numéro atomique élevé Z influencent les informations de l'image. Bien que la plupart des tissus dans le corps soient proches de la densité de l'eau, et que δ soit presque constante, il existe des régions dans le corps contenant de l'os comme dans le crâne où la variation de δ est plus importante. Le contraste élevé que les images de δ fournissent peut compléter avantageusement les images de RSP, même en imagerie diagnostique. Une solution pour résoudre les artefacts de reconstruction de l'imagerie de δ est de modéliser la dépendance de la perte d'énergie de l'angle de dispersion comme des contraintes et en incorporant ce modèle dans la reconstruction itérative.

Le diagramme bruit-dose montre que la carte RSP démontre la meilleure précision entre les trois modalités de pCT. La résolution spatiale de la δ est, toutefois, com-

parable à la carte RSP et, dans certains cas, semble encore mieux à la périphérie du fantôme.

7.4 Conclusion

Nous avons étudié la possibilité d'utiliser les informations de diffusion de protons pour la reconstruction de l'image du pouvoir de diffusion relatif δ de l'objet tout en tenant compte d'une trajectoire courbe de protons. L'image de δ est reliée à la longueur de radiation X_0 (ou de diffusion X_S) du matériau, et cette quantité est également liée à deux propriétés intrinsèques du matériau, le numéro atomique (Z) et la densité (ρ). Les résultats préliminaires montrent que les images pCT par diffusion pourraient fournir un complément d'information sur le matériel qui pourrait être utilisé en combinaison avec la tomographie proton conventionnelle par perte d'énergie spécifiquement dans les calculs de dose latérale. L'artefact inhérent de cape ou coupe (selon le signe de la variation de δ) reste encore un problème et d'autres applications de la méthode que la planification de traitement doivent encore être explorées.

8 Conclusion et travaux futurs

La nécessité d'un plan de traitement précis en proton-thérapie en particulier pour une dosimétrie plus conformationnelle a déclenché un regain d'intérêt pour améliorer l'imagerie du proton. L'acquisition directe du pouvoir d'arrêt relatif (RSP) avec des protons en utilisant des mesures de la perte d'énergie rend la pCT un outil prometteur pour améliorer la conformation de la dose sur la tumeur par rapport à la xCT conventionnelle. Contrairement aux photons, les interactions des protons dans la matière sont très nombreuses et assez complexes, et c'est pour cette raison que les premières images proton n'ont pas réussi à répondre aux exigences cliniques actuelles dans la planification du traitement. L'une des raisons est la faible résolution spatiale attribuée à la diffusion des protons dans la matière. D'autre part, c'est également cette complexité de modélisation des interactions proton qui fait que les informations au delà du pouvoir d'arrêt ne peuvent pas être facilement estimées. Les reconstructions utilisant des quantités autres que la perte d'énergie ont été réalisées par Bopp et al. (2013) et nous avons également étudié plus profondément ces modalités pCT utilisant les interactions nucléaires et la diffusion multiple pour reconstruire le coefficient d'atténuation linéique des interactions nucléaires inélastiques (κ) et le pouvoir relatif de diffusion (δ) de la matière. Les données utilisées dans la pCT par perte d'énergie pourraient être réutilisées pour les deux autres modalités de pCT. Cela signifie que trois cartes de différentes quantités pourraient être générées en une seule acquisition.

La caractérisation de l'image par des figures de mérites telles que la justesse, la précision et la résolution spatiale a été étudiée et les résultats ont été comparés à la pCT conventionnelle par perte d'énergie. Les résultats ont montré que, bien que les images de RSP donnent les meilleures performances en termes de justesse et de précision, la résolution spatiale des autres modalités pCT était comparable et dans certaines situations encore mieux par rapport aux images RSP conventionnelles.

Bien que le RSP soit nécessaire pour la planification du traitement des calculs de dose, les images de κ et de δ pourraient fournir des informations supplémentaires intrinsèques de la matière. Par exemple, les tissus ayant le même RSP seraient impossibles à distinguer en RSP, mais pourraient être différenciés avec les deux autres cartes. Cela pourrait conduire à l'utilisation de pCT non seulement comme outil pour la dosimétrie, mais aussi pour le diagnostic. Bien que l'application diagnostic de l'imagerie proton ait déjà été envisagée par le passé, avant même d'ailleurs que son potentiel ne soit évalué pour la dosimétrie, la quantité d'informations qui pourrait être extraite des pCT par atténuation et par diffusion n'a pas encore été ni explorée et ni validée expérimentalement.

Il a été mentionné que la faible résolution spatiale des images pCT par rapport à celles xCT limite son potentiel comme outil que les cliniciens pourraient utiliser dans la planification du traitement. Cependant, il a été démontré dans le passé que, par la modélisation de la trajectoire de protons courbe et son intégration dans la reconstruction améliorerait considérablement la résolution spatiale. Nous avons démontré qu'en effet, à l'aide du MLP, une amélioration significative a été obtenue pour les différentes modalités de pCT. L'inconvénient de l'utilisation du MLP est le temps de calcul lent attribué à des calculs individuels de la trajectoire pour chaque paire de protons. Cela peut être facilement résolu en utilisant des ordinateurs puissants et en exécutant la reconstruction en parallèle (sur architecture GPU par exemple).

Les reconstructions d'images pCT sont liées à la physique des modèles de reconstruction. Nous avons développé le problème inverse pour reconstruire les valeurs de κ et de δ. La technique de reconstruction utilisée dans cette étude pour résoudre ces problèmes inverses est fondée sur des méthodes analytiques en xCT, à savoir la rétroprojection filtrée (FBP). Cette méthode est plus rapide que les techniques itératives, toutefois, en raison de la nécessité d'intégrer une trajectoire courbe (MLP) de protons dans les reconstructions, les reconstructions avec MLP se limitaient à l'utilisation de techniques itératives. Il a été démontré par Rit et al. (2013) que les trajectoires courbes de protons pouvaient être intégrées dans la FBP par l'échantillonnage des projection pilotée par la distance pour chacune des différentes positions de la source définie par le modèle courbe de la trajectoire. Cette technique a été étudiée d'abord dans la pCT par perte d'énergie et nous avons adapté le même algorithme pour les pCT par atténuation et par diffusion.

La justesse et la précision des images pCT reconstruites peuvent également être améliorées en utilisant des techniques itératives. Des contraintes supplémentaires dans le modèle direct ne peuvent pas être intégrées facilement dans les reconstructions analytiques contrairement aux méthodes itératives. Par exemple, les artefacts en pCT par diffusion dus à la variation du pouvoir relatif de diffusion peuvent être corrigés à l'aide de modèles appropriés comme des contraintes dans la méthode itérative.

Les différentes images pourraient être générées par une seule acquisition, ce qui est un atout de l'imagerie pCT et pourrait conduire à des reconstructions multivariées. Par exemple, en raison des possibilités de distinguer plus clairement les limites de l'objet dans les images d'atténuation κ, il serait possible d'améliorer ou même de corriger les images de RSP. Une méthode similaire à ce qui se fait dans l'imagerie en contraste de phase (rayons X) pourrait être une solution pour permettre

de résoudre la limite des marges le long des discontinuités de matériaux. Tandis que les images de pouvoir d'arrêt relatif RSP seront utilisées comme entrées pour le calcul de la dose, le RSP n'est réellement approprié que pour la direction longitudinale, c'est à dire la direction du trajet du faisceau de traitement. Les images de pouvoir de diffusion relatif δ pourraient être utilisées pour compléter le protocole actuel, en fournissant des informations telles que la longueur de radiation de la matière pour le calcul de la dose latérale. Cela pourrait compléter la planification du traitement, en particulier pour les cas où l'os et d'autres matériaux denses sont le long de la trajectoire du faisceau. La diffusion latérale du faisceau a été un problème connu en raison de la modélisation incomplète du MCS dans la trajectoire du faisceau qui se traduit également à par une imprécision sur la longueur de parcours (Paganetti, 2012). En intégrant des modèles dosimétriques appropriés, et en utilisant à la fois le RSP et des images de δ comme apports, un plan de traitement plus fiable serait atteint.

La précision des valeurs reconstruites dépend principalement des données protons utilisées. Les particules qui sont détectées après avoir traversé un objet sont composées de primaires sans interaction nucléaire, de primaires avec des interactions élastiques, de protons secondaires et d'autres particules. Différentes données proton sont utilisées en fonction du modèle de reconstruction utilisé. Par exemple, dans la pCT par perte d'énergie, une coupe à la fois en énergie et en distribution angulaire a été imposée pour écarter la majorité des secondaires et des primaires ayant eu une interaction élastique. En théorie, les mêmes données filtrées que dans la pCT par perte d'énergie doivent être utilisées pour la pCT par diffusion. Cependant, il a été constaté que les coupures sous-estiment la variance dans la région périphérique. Cela n'a jamais été un problème avec la pCT par perte d'énergie puisque la valeur moyenne de la WEPL (au sens de la perte d'énergie) a été utilisée comme projection, par conséquent, ce qui limite la largeur (meilleure précision) et donne une meilleure justesse. Pour la pCT par dispersion, puisque c'est la variance de la distribution angulaire qui est calculée, une sous-estimation de la variance à la périphérie due à la coupure limite la précision de la valeur de δ reconstruite. En outre, pour la pCT par atténuation, une coupure plus grande a été utilisée pour réduire la majorité des secondaires tout en gardant les primaires avec des interactions nucléaires. La coupure de dix écarts-types a été optimisée pour un fantôme d'eau cylindrique, par conséquent, des inexactitudes pourraient être introduites pour des fantômes inhomogènes. Connaissant ces limitations, nous suggérons d'investiguer une amélioration la sélection des données en implémentant une coupure plus optimisée et plus robuste au cours des reconstructions. Une autre façon serait d'utiliser des modèles théoriques sur les interactions nucléaires pour sélectionner les protons en fonction de l'épaisseur traversée et des matériaux impliqués.

Les trois modalités de pCT étudiées font l'usage de protons primaires transmis. L'utilisation de protons secondaires pour la reconstruction de la carte d'hydrogène de la matière a déjà été démontré expérimentalement dans le passé (Saudinos, 1987). Les informations supplémentaires de cette carte peut aider à différencier les tissus normaux de la tumeur et pourrait contribuer à améliorer le plan de traitement.

Les méthodes de reconstruction proposées font l'usage d'un suivi individuel des protons (mode-liste). Cela se traduit aussi par des contraintes sur les détecteurs pour répondre aux exigences des modèles de reconstruction. Divers groupes dédiés

à l'imagerie proton ont exploré différents systèmes matériels. La justesse et la précision des images pCT dépendent également du bruit électronique ou d'une erreur systématique du matériel. Compte tenu de la physique des interactions des protons, des détecteurs d'énergie devraient avoir une résolution qui correspond à la dispersion en énergie des protons pour une épaisseur donnée. Ceci est également vrai avec la résolution spatiale des détecteurs de passage, i.e. il doit correspondre à la dispersion spatiale des protons dus à la diffusion multiple. Actuellement, les deux critères sont encore difficiles à réaliser en raison des limitations de la technologie du matériel et du coût de ces détecteurs.

De plus, l'imagerie du proton est limitée à l'énergie la plus élevée qu'il est possible de délivrer. Une acquisition de pCT d'une tête humaine moyenne (20 cm) nécessiterait une énergie incidente de 200 MeV et un bassin moyen (33 cm) aurait besoin d'au moins 250 MeV. Cela peut limiter la pCT aux enfants et aux personnes non obèses. Cependant, des techniques hybrides ont été proposées pour utiliser les données de xCT combinées aux données proton, là où l'acquisition de données de protons est impossible (Hansen et al., 2014).

Bien qu'en théorie l'approche de suivi individuel des protons donne de meilleures performances par rapport à la technique par intégration, il serait utile d'examiner quantitativement le gain potentiel en justesse et en précision de l'approche suivi individuel dans l'environnement clinique. De plus, des images de pouvoir d'arrêt relatif pourraient être générées en utilisant l'imagerie bi-énergie par rayons X (DECT). Actuellement, il n'y a pas de seuil de précision établie. Si en pratique clinique la qualité fournie des images RSP générées par imagerie X semble suffisante, l'apport de l'imagerie pCT doit être réexaminé.

L'imagerie proton n'est pas seulement limitée à l'environnement clinique. L'imagerie proton par atténuation a déjà été utilisée en contrôle non destructif. En raison de l'effet West-Sherwood, de minuscules fissures peuvent être visualisées sans intervention invasive.

Pour conclure, l'imagerie pCT pourrait améliorer la planification du traitement en proton-thérapie, à la fois en dosimétrie et en diagnostic. Cependant, sa translation à la pratique clinique reste difficile en raison des contraintes matérielles. Les mérites que cette modalité d'imagerie pourrait apporter par rapport aux autres modalités de planification de traitement doivent encore être explorées.

References

Ainsley C and Yeager C 2014 Practical considerations in the calibration of CT scanners for proton therapy *Journal of Applied Clinical Medical Physics* **15**(3), 202–220.

Allison J, Amako K, Apostolakis J, Araujo H, Dubois P A, Asai M, Barrand G, Capra R, Chauvie S, Chytracek R, Cirrone G A P, Cooperman G, Cosmo G, Cuttone G, Daquino G G, Donszelmann M, Dressel M, Folger G, Foppiano F, Generowicz J, Grichine V, Guatelli S, Gumplinger P, Heikkinen A, Hrivnacova I, Howard A, Incerti S, Ivanchenko V, Johnson T, Jones F, Koi T, Kokoulin R, Kossov M, Kurashige H, Lara V, Larsson S, Lei F, Link O, Longo F, Maire M, Mantero A, Mascialino B, McLaren I, Lorenzo P M, Minamimoto K, Murakami K, Nieminen P, Pandola L, Parlati S, Peralta L, Perl J, Pfeiffer A, Pia M G, Ribon A, Rodrigues P, Russo G, Sadilov S, Santin G, Sasaki T, Smith D, Starkov N, Tanaka S, Tcherniaev E, Tome B, Trindade A, Truscott P, Urban L, Verderi M, Walkden A, Wellisch J P, Williams D C, Wright D and Yoshida H 2006 Geant4 developments and applications *IEEE Transactions on Nuclear Science* **53**(1), 270–278.

Amaldi U, Bianchi A, Chang Y H, Go A, Hajdas W, Malakhov N, Samarati J, Sauli F and Watts D 2011 Construction, test and operation of a proton range radiography system *Nuclear Instruments and Methods in Physics Research Section A: Accelerators, Spectrometers, Detectors and Associated Equipment* **629**(1), 337 – 344.

Andreo P 2009 On the clinical spatial resolution achievable with protons and heavier charged particle radiotherapy beams *Physics in Medicine and Biology* **54**(11), N205–N215.

Arbor N, Dauvergne D, Dedes G, Letang J M, Parodi K, Quinones C T, Testa E and Rit S 2015 Monte Carlo comparison of x-ray and proton CT for range calculations of proton therapy beams *Physics in Medicine and Biology* **60**(19), 7585–7599.

Bashkirov V A, Schulte R W, Hurley R F, Johnson R P, Sadrozinski H F W, Zatserklyaniy A, Plautz T and Giacometti V 2016 Novel scintillation detector design and performance for proton radiography and computed tomography *Medical Physics* **43**(2), 664–674.

Berger J, Duchazeaubeneix J C, Faivre J C, Garreta D, Legrand D, Rouger M, Saudinos J, Charpak G, Guillerminet B, Santiard J C, Sauli F, Lecaque G, Palmieri P,

Raybaud C and Salamon G 1978 Reconstruction tomography by nuclear scattering radiography *Neuroradiology* **16**, 576–578.

Besemer A, Paganetti H and Bednarz B 2013 The clinical impact of uncertainties in the mean excitation energy of human tissues during proton therapy *Physics in Medicine and Biology* **58**(4), 887–902.

Bethe H 1930 Zur Theorie des durchgangs schneller Korpuskularstrahlen durch materie *Annalen der Physik* **397**(3), 325–400.

Bethe H 1953 Molière's theory of multiple scattering *Phys. Rev.* **89**(6), 1256–1266.

Bloch F 1933 Zur Bremsung rasch bewegter Teilchen beim Durchgang durch Materie *Annalen der Physik* **408**, 285–320.

Bopp C, Colin J, Cussol D, Finck C, Labalme M, Rousseau M and Brasse D 2013 Proton computed tomography from multiple physics processes *Physics in Medicine and Biology* **58**(20), 7261—-7276.

Bopp C, Rescigno R, Rousseau M and Brasse D 2015 Quantitative proton imaging from multiple physics processes: a proof of concept *Physics in Medicine and Biology* **60**(13), 5325—5341.

Bortfeld T 1997 An analytical approximation of the Bragg curve for therapeutic proton beams *Medical Physics* **24**(12), 2024–2033.

Braccini S, Ereditato a, Kreslo I, Moser U, Pistillo C, Studer S, Scampoli P, Coray a and Pedroni E 2010 First results on proton radiography with nuclear emulsion detectors *Journal of Instrumentation* **5**(09), P09001.

Bragg W H and Kleeman R 1905 On the alpha particles of radium, and their loss of range in passing through various atoms and molecules *Philosophical Magazine Series 6* **10**(57), 318–340.

Bruzzi M, Civinini C, Scaringella M, Bonanno D, Brianzi M, Carpinelli M, Cirrone G, Cuttone G, Presti D L, Maccioni G, Pallotta S, Randazzo N, Romano F, Sipala V, Talamonti C and Vanzi E 2016 Proton computed tomography images with algebraic reconstruction *In Press: Nuclear Instruments and Methods in Physics Research Section A: Accelerators, Spectrometers, Detectors and Associated Equipment* .

Bucciantonio M, Amaldi U, Kieffer R, Sauli F and Watts D 2013 Development of a fast proton range radiography system for quality assurance in hadrontherapy *Nuclear Instruments and Methods in Physics Research Section A: Accelerators, Spectrometers, Detectors and Associated Equipment* **732**, 564–567.

Calvel P, Barillot C, Porte A, Auriel G, Chatry C, Peyrard P F, Santin G, Ecoffet R and Jordan T M 2008 Review of deposited dose calculation methods using ray tracing approximations *IEEE Transactions on Nuclear Science* **55**(6), 3106–3113.

Chadwick M 1997 Calculation of nuclear data for fast neutron and proton radiotherapy: A new ICRU report.

Charpak G, Majewski S, Perrin Y, Saudinos J, Sauli F, Townsend D and Vinciarelli J 1976 Further results in nuclear scattering radiography *Physics in Medicine and Biology* **21**(6), 941–948.

Chu W T, Ludewigt B A and Renner T R 1993 Instrumentation for treatment of cancer using proton and light-ion beams *Review of Scientific Instruments* **64**(8), 2055–2122.

Chvetsov A V and Paige S L 2010 The influence of CT image noise on proton range calculation in radiotherapy planning. *Physics in Medicine and Biology* **55**(6), N141–N149.

Ciangaru G, Polf J C, Bues M and Smith A R 2005 Benchmarking analytical calculations of proton doses in heterogeneous matter *Medical Physics* **32**(12), 3511–3523.

Cirrone G a P, Bucciolini M, Bruzzi M, Candiano G, Civinini C, Cuttone G, Guarino P, Lo Presti D, Mazzaglia S E, Pallotta S, Randazzo N, Sipala V, Stancampiano C and Talamonti C 2011 Monte Carlo evaluation of the filtered back projection method for image reconstruction in proton computed tomography *Nuclear Instruments and Methods in Physics Research, Section A: Accelerators, Spectrometers, Detectors and Associated Equipment* **658**(1), 78–83.

Cirrone G, Candiano G, Cuttone G, Nigro S L, Presti D L, Randazzo N, Sipala V, Russo M, Aiello S, Bruzzi M, Menichelli D, Scaringella M, Miglio S, Bucciolini M, Talamonti C and Pallotta S 2007 The Italian project for a proton imaging device *Nuclear Instruments and Methods in Physics Research Section A: Accelerators, Spectrometers, Detectors and Associated Equipment* **576**(1), 194–197. Proceedings of the 8th International Workshop on Radiation Imaging Detectors.

Civinini C, Brianzi M, Bruzzi M, Bucciolini M, Candiano G, Capineri L, Cirrone G a P, Cuttone G, Lo Presti D, Marrazzo L, Mazzaglia E, Menichelli D, Pieri S, Randazzo N, Sipala V, Stancampiano C, Talamonti C, Tesi M and Valentini S 2010 Towards a proton imaging system *Nuclear Instruments and Methods in Physics Research, Section A: Accelerators, Spectrometers, Detectors and Associated Equipment* **623**(1), 588–590.

Civinini C, Bruzzi M, Bucciolini M, Carpinelli M, Cirrone G, Cuttone G, Lo Presti D, Pallotta S, Pugliatti C, Randazzo N, Romano F, Scaringella M, Sipala V, Stancampiano C, Talamonti C, Vanzi E and Zani M 2013 Recent results on the development of a proton computed tomography system *Nucl Instr Meth Phys Res, Sect A* **732**, 573–576.

Collins Fekete C A, Doolan P, Dias M, Beaulieu L and Seco J 2015 Developing a phenomenological model of the proton trajectory within a heterogeneous medium required for proton imaging *Physics in Medicine and Biology* **60**(13), 5071–5082.

Cookson J 1974 Radiography with protons *Naturwissenschaften* **61**(5), 184–191.

Cormack A M 1963 Representation of a function by its line integrals, with some radiological applications *Journal of Applied Physics* **34**(9), 2722–2727.

Cormack A M and Koehler A M 1976 Quantitative proton tomography: preliminary experiments *Physics in Medicine and Biology* **21**(4), 560–569.

Crowe K M, Budinger T F, Cahoon J L, Elischer V P, Huesman R H and Kanstein L L 1975 Axial scanning with 900 MeV alpha particles (LBL-3812), 1–3.

Curry J and Steward V W 1978 Establishment of a beam line at the Fermi National Accelerator Laboratory for proton radiography *Medical Physics* **5**(3), 188–194.

Duchazeaubeneix 1980 Nuclear scattering radiography *J Comput Assist Tomogr* .

Erdelyi B 2009 A comprehensive study of the most likely path formalism for proton-computed tomography *Physics in Medicine and Biology* **54**(20), 6095–6122.

Esposito M, Anaxagoras T, Evans P, Green S, Manolopoulos S, Nieto-Camero J, Parker D, Poludniowski G, Price T, Waltham C and Allinson N 2015 CMOS active pixel sensors as energy-range detectors for proton computed tomography *Journal of Instrumentation* **10**(06), C06001–C06001.

Feldkamp L A, Davis L C, Kress J W, L. A. Feldkamp L. C. Davis and Kress J W 1984 Practical cone-beam algorithm *J. Opt. Soc. Am. A* **1**(6), 612–619.

Frey E C and Tsui B M W 1993 A practical method for incorporating scatter in a projector-backprojector for accurate scatter compensation in SPECT *IEEE Transactions on Nuclear Science* **40**(4), 1107–1116.

Frey E C and Tsui B M W 1994 Modeling the scatter response function in inhomogeneous scattering media for SPECT *IEEE Transactions on Nuclear Science* **41**(4), 1585–1593.

Fu J, Schleede S, Tan R, Chen L, Bech M, Achterhold K, Gifford M, Loewen R, Ruth R and Pfeiffer F 2013 An algebraic iterative reconstruction technique for differential x-ray phase-contrast computed tomography *Zeitschrift für Medizinische Physik* **23**(3), 186–193. Schwerpunkt: Röntgenbasierte Phasenkontrast Bildgebung.

Gatti P 2004 *Probability Theory and Mathematical Statistics for Engineers* Structural Engineering: Mechanics and Design Taylor & Francis.

Goitein M 1972 Three-dimensional density reconstruction from a series of two-dimensional projections *Nuclear Instruments and Methods* **101**(3), 509–518.

Gore J C and Tofts P S 1978 Statistical limitations in computed tomography *Physics in Medicine and Biology* **23**(6), 1176–1182.

Gottschalk B 2010 On the scattering power of radiotherapy protons *Medical Physics* **37**(1), 352–367.

Gottschalk B, Koehler A, Schneider R, Sisterson J and Wagner M 1993 Multiple coulomb scattering of 160 MeV protons *Nuclear Instruments and Methods in Physics Research Section B: Beam Interactions with Materials and Atoms* **74**(4), 467–490.

Grevillot L, Frisson T, Zahra N, Bertrand D, Stichelbaut F, Freud N and Sarrut D 2010 Optimization of GEANT4 settings for proton pencil beam scanning simulations using GATE *Nucl Instr Meth Phys Res, Sect B* **268**(20), 3295–3305.

Hansen D, Petersen J, Bassler N and Sörensen T S 2014 Improved proton computed tomography by dual modality image reconstruction. *Medical Physics* **41**(3), 031904.

Hanson K M 1979 Proton computed tomography *IEEE Transactions on Nuclear Science* **26**(1), 1635–1640.

Hanson K M, Bradbury J N, Cannon T M, Hutson R L, Laubacher D B, Macek R J, Paciotti M A and Taylor C A 1981 Computed tomography using proton energy loss *Physics in Medicine and Biology* **26**(6), 965–983.

Hanson K M, Bradbury J N, Cannon T M, Hutson R L, Laubacher D B, Macek R, Paciotti M A and Taylor C A 1978 The application of protons to computed tomography *IEEE Transactions on Nuclear Science* **25**(1), 657–660.

Hanson K M, Bradbury J N, Koeppe R a, Macek R J, Machen D R, Morgado R, Paciotti M a, Sandford S a and Steward V W 1982 Proton computed tomography of human specimens. *Physics in Medicine and Biology* **27**(1), 25–36.

Held K D, Kawamura H, Kaminuma T, Paz A E S, Yoshida Y, Liu Q, Willers H and Takahashi A 2016 Effects of charged particles on human tumor cells *Frontiers in Oncology* **6**(23).

Highland V L 1975 Some practical remarks on multiple scattering *Nuclear Instruments and Methods* **129**(2), 497–499.

Huesman R, Rosenfeld A and Solmitz F 1975 Comparison of heavy charged particles and x-rays for axial tomograpic scanning Technical Report LBL–3040 California Univ., Davis (USA). Dept. of Engineering United States.

Hurley R F, Schulte R W, Bashkirov V a, Wroe a J, Ghebremedhin a, Sadrozinski H F W, Rykalin V, Coutrakon G, Koss P and Patyal B 2012 Water-equivalent path length calibration of a prototype proton CT scanner *Medical Physics* **39**(5), 2438–2446.

Ivanov M, Vignote J, Alvarez-Rodriguez R and Udias J 2011 A systematic study of elastic proton-nucleus scattering *Nuclear Theory* **30**, 116–125.

Jakel O, Smith A and Orton C 2013 The more important heavy charged particle radiotherapy of the future is more likely to be with heavy ions rather than protons *Medical Physics* **40**(9), 090601.

Jan S, Benoit D, Becheva E, Carlier T, Cassol F, Descourt P, Frisson T, Grevillot L, Guigues L, Maigne L, Morel C, Perrot Y, Rehfeld N, Sarrut D, Schaart D, Stute S, Pietrzyk U, Visvikis D, Zahra N and Buvat I 2011 GATE V6: a major enhancement of the GATE simulation platform enabling modelling of CT and radiotherapy. *Phys Med Biol* **56**(4), 881–901.

Janni J F 1982 Energy loss, range, path length, time-of-flight, straggling, multiple scattering, and nuclear interaction probability *Atomic Data and Nuclear Data Tables* **27**(2), 147–339.

Jia X, Schumann J, Paganetti H and Jiang S B 2012 GPU-based fast Monte Carlo dose calculation for proton therapy *Phys Med Biol* **57**(23), 7783–7797.

Johnson L, Keeney B, Ross G, Sadrozinski H W, Seiden a, Williams D, Zhang L, Bashkirov V, Schulte R and Shahnazi K 2003 Initial studies on proton computed tomography using a silicon strip detector telescope *Nuclear Instruments and Methods in Physics Research Section A: Accelerators, Spectrometers, Detectors and Associated Equipment* **514**(1-3), 215–223.

Johnson R P, Bashkirov V, DeWitt L, Giacometti V, Hurley R F, Piersimoni P, Plautz T E, Sadrozinski H F W, Schubert K, Schulte R, Schultze B and Zatserklyaniy A 2016 A fast experimental scanner for proton CT: Technical performance and first experience with phantom scans *IEEE Transactions on Nuclear Science* **63**(1), 52–60.

Keeney B, Bashkirov V, Johnson R P, Kroeger W, Ohyama H, Sadrozinski H F W, Schulte R W M, Seiden A and Spradlin P 2002 A silicon telescope for applications in nanodosimetry *IEEE Transactions on Nuclear Science* **49**(4), 1724–1727.

Koehler A M 1968 Proton radiography. *Science (New York, N.Y.)* **160**(3825), 303–304.

Krah N, Testa M, Brons S, Jäkel O, Parodi K, Voss B and Rinaldi I 2015 An advanced image processing method to improve the spatial resolution of ion radiographies *Phys Med Biol* **60**(21), 8525–8547.

Li T and Liang J Z 2004 Reconstruction with most likely trajectory for proton computed tomography Vol. 5370 pp. 2067–2074.

Li T, Liang Z, Singanallur J V, Satogata T J, Williams D C and Schulte R W 2006 Reconstruction for proton computed tomography by tracing proton trajectories: a Monte Carlo study. *Medical Physics* **33**(3), 699–706.

Lo Presti D, Bonanno D, Longhitano F, Pugliatti C, Aiello S, Cirrone G A P, Giordano V, Leonora E, Randazzo N, Romano F, Russo G V, Sipala V, Stancampiano C and Ventura C 2014 A real-time, large area, high space resolution particle radiography system *Journal of Instrumentation* **9**(06), C06012.

Martin R, Foss M, Moenich J and Lari R 1975 The proton diagnostic accelerator *Nuclear Science, IEEE Transactions on* **22**(3), 1802–1804.

Matsufuji N, Tomura H, Futami Y, Yamashita H, Higashi A, Minohara S, Endo M and Kanai T 1998 Relationship between CT number and electron density, scatter angle and nuclear reaction for hadron-therapy treatment planning *Physics in Medicine and Biology* **43**(11), 3261–3275.

Menichelli D, Bruzzi M, Bucciolini M, Candiano G, Cirrone G A P, Capineri L, Civinini C, Cuttone G, Presti D L, Marrazzo L, Pallotta S, Randazzo N, Sipala V, Talamonti C, Valentini S, Pieri S, Reggioli V, Brianzi M and Tesi M 2010 Characterization of a silicon strip detector and a YAG:Ce calorimeter for a proton computed radiography apparatus *IEEE Transactions on Nuclear Science* **57**(1), 8–16.

Moffett D R, Colton E P, Concaildi G A, Hoffman E W, Klem R D, Knott M J, Kramer S L, Martin R L, Parker E F, Passi A R, Schultz P F, Stockley R L, Timm R E, Skaggs L S and Steward V W 1975 Initial test of a proton radiographic system *IEEE Transactions on Nuclear Science* **22**(3), 1749–1751.

Mohan R and Bortfeld T 2011 Proton therapy: clinical gains through current and future treatment programs *Front Radiat Ther Oncol* **43**, 440–464.

Moliere G 1948 Theory of the scattering of fast charged particles. 2. Repeated and multiple scattering *Z. Naturforsch.* **A3**, 78–97.

Morris C, King N, Kwiatkowski K, Mariam F, Merrill F and Saunders A 2013 Charged particle radiography *Rep Prog Phys* **76**(4), 046301.

Morris C L, Ables E, Alrick K R, Aufderheide M B, Barnes P D, Buescher K L, Cagliostro D J, Clark D a, Clark D J, Espinoza C J, Ferm E N, Gallegos R a, Gardner S D, Gomez J J, Greene G a, Hanson a, Hartouni E P, Hogan G E, King N S P, Kwiatkowski K, Liljestrand R P, Mariam F G, Merrill F E, Morgan D V, Morley K B, Mottershead C T, Murray M M, Pazuchanics P D, Pearson J E, Sarracino J S, Saunders a, Scaduto J, Schach Von Wittenau a E, Soltz R a, Sterbenz S, Thompson R T, Vixie K, Wilke M D, Wright D M and Zumbro J D 2011 Flash radiography with 24 GeV/c protons *Journal of Applied Physics* **109**(10), 104905.

Naimuddin M, Coutrakon G, Blazey G, Boi S, Dyshkant A, Erdelyi B, Hedin D, Johnson E, Krider J, Rukalin V, Uzunyan S, Zutshi V, Fordt R, Sellberg G, Rauch J, Roman M, Rubinov P and Wilson P 2016 Development of a proton computed tomography detector system *Journal of Instrumentation* **11**(02), C02012.

Nuyts J, De Man B, Fessler J, Zbijewski W and Beekman F 2013 Modelling the physics in the iterative reconstruction for transmission computed tomography *Phys Med Biol* **58**(12), R63–R96.

Paganetti H 2002 Nuclear interactions in proton therapy: dose and relative biological effect distributions originating from primary and secondary particles *Physics in Medicine and Biology* **47**(5), 747–764.

Paganetti H 2011 *Proton Therapy Physics* Series in Medical Physics and Biomedical Engineering Taylor & Francis.

Paganetti H 2012 Range uncertainties in proton therapy and the role of Monte Carlo simulations *Physics in Medicine and Biology* **57**(11), R99–R117.

Palmans H and Verhaegen F 2005 Assigning nonelastic nuclear interaction cross sections to hounsfield units for Monte Carlo treatment planning of proton beams *Physics in Medicine and Biology* **50**(5), 991–1000.

Pemler P, Besserer J, De Boer J, Dellert M, Gahn C, Moosburger M, Schneider U, Pedroni E and Stäuble H 1999 A detector system for proton radiography on the gantry of the Paul-Scherrer-Institute *Nuclear Instruments and Methods in Physics Research, Section A: Accelerators, Spectrometers, Detectors and Associated Equipment* **432**(2-3), 483–495.

Penfold S and Censor Y 2015 Techniques in iterative proton CT image reconstruction *Sensing and Imaging* **16**(1), 1–21.

Penfold S, Rosenfeld A, Schulte R and Schubert K 2009 A more accurate reconstruction system matrix for quantitative proton computed tomography *Medical Physics* **36**(10), 4511–4518.

Penfold S, Schulte R, Censor Y and Rosenfeld A 2010 Total variation superiorization schemes in proton computed tomography image reconstruction *Medical Physics* **37**(11), 5887–5895.

Plautz T, Bashkirov V, Feng V, Hurley F, Johnson R P, Leary C, Macafee S, Plumb A, Rykalin V, Sadrozinski H, Schubert K E, Schulte R W, Schultze B, Steinberg D, Witt M and Zatserklyaniy A 2014 200 MeV proton radiography studies with a hand phantom using a prototype proton CT scanner *IEEE Transactions on Medical Imaging* **33**(4), 875–881.

Poludniowski G, Allinson N and Evans P 2015 Proton radiography and tomography with application to proton therapy *Br J Radiol* **88**(1053), 20150134.

Poludniowski G, Allinson N M, Anaxagoras T, Esposito M, Green S, Manolopoulos S, Nieto-Camero J, Parker D J, Price T and Evans P M 2014 Proton-counting radiography for proton therapy: a proof of principle using CMOS APS technology *Physics in Medicine and Biology* **59**(11), 2569.

Poludniowski G, Allinson N M and Evans P M 2014 Proton computed tomography reconstruction using a backprojection-then-filtering approach *Physics in Medicine and Biology* **59**(24), 7905–7918.

Price T and Consortium P 2016 PRaVDA: High energy physics towards proton computed tomography *Nuclear Instruments and Methods in Physics Research Section A: Accelerators, Spectrometers, Detectors and Associated Equipment* **824**, 226–227.

Price T, Esposito M, Poludniowski G, Taylor J, Waltham C, Parker D J, Green S, Manolopoulos S, Allinson N M, Anaxagoras T, Evans P and Nieto-Camero J 2015 Expected proton signal sizes in the PRaVDA range telescope for proton computed tomography *Journal of Instrumentation* **10**(05), P05013.

Quiñones C T, Létang J M and Rit S 2016 Filtered back-projection reconstruction for attenuation proton CT along most likely paths *Physics in Medicine and Biology* **61**(9), 3258–3278.

Rinaldi I 2011 Investigation of novel imaging methods using therapeutic ion beams PhD thesis Ruperto-Carola Univeristy of Heidelberg.

Rit S, Clackdoyle R, Hoskovec J and Létang J 2015 List-mode proton CT reconstruction using their most likely paths via the finite Hilbert transform of the derivative of the backprojection *in* 'Fully 3D Image Reconstruction in Radiology and Nuclear Medicine' Newport, USA pp. 324–327.

Rit S, Dedes G, Freud N, Sarrut D and Létang J M 2013 Filtered backprojection proton CT reconstruction along most likely paths *Medical Physics* **40**(3), 031103.

Sadrozinski H F W, Bashkirov V, Bruzzi M, Johnson L R, Keeney B, Ross G, Schulte R W, Seiden A, Shahnazi K, Williams D C and Zhang L 2003 Issues in proton computed tomography *Nucl Instr Meth Phys Res, Sect A* **511**(1-2), 275–281. Proceedings of the 11th International Workshop on Vertex Detectors.

Sadrozinski H F W, Bashkirov V, Keeney B, Johnson L, Peggs S, Ross G, Satogata T, Schulte R, Seiden A, Shanazi K and Williams D 2004 Toward proton computed tomography **51**(1), 3–9.

Sadrozinski H W, Johnson R, Macafee S, Plumb A, Steinberg D, Zatserklyaniy A, Bashkirov V, Hurley R and Schulte R 2013 Development of a head scanner for proton CT *Nuclear Instruments and Methods in Physics Research Section A: Accelerators, Spectrometers, Detectors and Associated Equipment* **699**, 205–210.

Saraya Y, Izumikawa T, Goto J, Kawasaki T and Kimura T 2014 Study of spatial resolution of proton computed tomography using a silicon strip detector *Nuclear Instruments and Methods in Physics Research Section A: Accelerators, Spectrometers, Detectors and Associated Equipment* **735**, 485–489.

Satogata T, Sadrozinski H W and Ruggiero A 2003 Dose/sensitivity in proton computed tomography *in* 'Nuclear Science Symposium Conference Record, 2003 IEEE' Vol. 5 pp. 3667–3671.

Saudinos J 1987 Imaging with high energy particles *Journal of Optics* **18**(4), 193–202.

Saudinos J, Charpak G, Sauli F, Townsend D and Vinciarelli J 1975 Nuclear scattering applied to radiography *Physics in Medicine and Biology* **20**(6), 890–905.

Scaringella M, Brianzi M, Bruzzi M, Bucciolini M, Carpinelli M, Cirrone G A P, Civinini C, Cuttone G, Presti D L, Pallotta S, Pugliatti C, Randazzo N, Romano F, Sipala V, Stancampiano C, Talamonti C, Tesi M, Vanzi E and Zani M 2013 The PRIMA (proton imaging) collaboration: Development of a proton computed tomography apparatus *Nuclear Instruments and Methods in Physics Research Section A: Accelerators, Spectrometers, Detectors and Associated Equipment* **730**(0), 178–183.

Scaringella M, Bruzzi M, Bucciolini M, Carpinelli M, Cirrone G, Civinini C, Cuttone G, Lo Presti D, Pallotta S, Pugliatti C, Randazzo N, Romano F, Sipala V, Stancampiano C, Talamonti C, Vanzik E and Zani M 2014 A proton computed tomography based medical imaging system *Journal of Instrumentation* **9**(12), C12009.

Schaffner B 2008 Proton dose calculation based on in-air fluence measurements *Phys Med Biol* **53**(6), 1545–1562.

Schaffner B and Pedroni E 1998 The precision of proton range calculations in proton radiotherapy treatment planning: experimental verification of the relation between CT-HU and proton stopping power. *Physics in Medicine and Biology* **43**(6), 1579–1592.

Schneider U, Besserer J, Pemler P, Dellert M, Moosburger M, Pedroni E and Kaser-Hotz B 2004 First proton radiography of an animal patient *Medical Physics* **31**, 1046–1051.

Schneider U and Pedroni E 1994 Multiple coulomb scattering and spatial resolution in proton radiography *Medical Physics* **21**(11), 1657–1663.

Schneider U and Pedroni E 1995 Proton radiography as a tool for quality control in proton therapy *Medical Physics* **22**(4), 353–363.

Schneider U, Pedroni E and Lomax a 1996 The calibration of CT hounsfield units for radiotherapy treatment planning. *Physics in Medicine and Biology* **41**(1), 111–124.

Schneider U, Pemler P, Besserer J, Pedroni E, Lomax A and Kaser-Hotz B 2005 Patient specific optimization of the relation between CT-hounsfield units and proton stopping power with proton radiography *Medical Physics* **32**(1), 195–199.

Schulte R, Bashkirov V, Li T, Liang J Z, Mueller K, Heimann J, Johnson L R, Keeney B, Sadrozinski H F W, Seiden A, Williams D C, Zhang L, Li Z, Peggs S, Satogata T and Woody C 2003 Design of a proton computed tomography system for applications in proton radiation therapy *in* 'Nuclear Science Symposium Conference Record, 2003 IEEE' Vol. 3 pp. 1579–1583 Vol.3.

Schulte R, Bashkirov V, Li T, Liang Z, Mueller K, Heimann J, Johnson L R, Keeney B, Sadrozinski H F W, Seiden A, Williams D C, Zhang L, Li Z, Peggs S, Satogata T and Woody C 2004 Conceptual design of a proton computed tomography system for applications in proton radiation therapy *Nuclear Science, IEEE Transactions on* **51**(3), 866–872.

Schulte R W, Bashkirov V, Loss Klock M C, Li T, Wroe A J, Evseev I, Williams D C and Satogata T 2005 Density resolution of proton computed tomography *Medical Physics* **32**(4), 1035–1046.

Schulte R W, Penfold S N, Tafas J T and Schubert K E 2008 A maximum likelihood proton path formalism for application in proton computed tomography *Medical Physics* **35**(11), 4849–4856.

Schulte R W and Wroe A J 2012 New developments in treatment planning and verification of particle beam therapy *Translational Cancer Research* **1**(3).

Seco J, Clasie B and Partridge M 2014 Review on the characteristics of radiation detectors for dosimetry and imaging *Phys Med Biol* **59**(20), R303–R347.

Seco J and Depauw N 2011 Proof of principle study of the use of a CMOS active pixel sensor for proton radiography *Medical Physics* **38**(2), 622–623.

Seltzer S M 1993 An Assessment of the Role of Charged Secondaries from Nonelastic Nuclear Interactions by Therapy Proton Beams in Water Technical Report NISTIR 5221 National Institute of Standards and Technology Gaithersburg, MD.

Slater J M, Archambeau J O, Miller D W, Notarus M I, Preston W and Slater J D 1992 The proton treatment center at Loma Linda University Medical Center: rationale for and description of its development *Int. J. Radiat. Oncol. Biol. Phys.* **22**(2), 383–389.

Souris K, Lee J A and Sterpin E 2016 Fast multipurpose Monte Carlo simulation for proton therapy using multi- and many-core CPU architectures *Medical Physics* **43**(4), 1700–1712.

Stafford P, Sherwood A and West D 1975 Proton radiographic detection of microporosity in aero-engine turbine castings *Non-Destructive Testing* **8**(5), 235–240.

Steward V 1976 Proton (and other heavy charged particle) radiography in medical diagnosis **23**(1), 577–583.

Steward V and Koehler A 1973*a* Proton beam radiography in tumor detection *Science* **179**(4076), 913–914.

Steward V and Koehler A 1973*b* Proton radiographic detection of strokes *Nature* **245**(5419), 38–40.

Steward V W and Koehler A M 1974 Proton radiography in the diagnosis of breast carcinoma *Radiology* **110**(1), 217–221.

Szymanowski H and Oelfke U 2002 Two-dimensional pencil beam scaling: an improved proton dose algorithm for heterogeneous media *Phys Med Biol* **47**(18), 3313–3330.

Takatsu J, van der Graaf E, Goethem M J V, van Beuzekom M, Klaver T, Visser J, Brandenburg S and Biegun A 2016 Proton radiography to improve proton therapy treatment *Journal of Instrumentation* **11**(01), C01004.

Talamonti C, Bruzzi M, Bucciolini M, Carpinelli M, Cirrone G, Civinini C, Cuttone G, Lo Presti D, Pallotta S, Randazzo N, Romano F, Scaringella M, Sipala V, Stancampiano C, Vanzi E and Zani M 2012 PRIMA proton imaging for clinical application *in* 'Nuclear Science Symposium and Medical Imaging Conference' pp. 2218–2221.

Talamonti C, Reggioli V, Bruzzi M, Bucciolini M, Civinini C, Marrazzo L, Menichelli D, Pallotta S, Randazzo N, Sipala V, Cirrone G, Petterson M, Blumenkrantz N, Feldt J, Heimann J, Lucia D, Seiden A, Williams D, Sadrozinski H W, Bashkirov V and Schulte R 2010 Proton radiography for clinical applications *Nucl Instr Meth Phys Res, Sect A* **612**(3), 571–575.

Tanaka S, Nishio T, Matsushita K, Tsuneda M, Kabuki S and Uesaka M 2016 Development of proton CT imaging system using plastic scintillator and CCD camera *Physics in Medicine and Biology* **61**(11), 4156–4167.

Taylor J, Allport P, Casse G, Smith N, Tsurin I, Allinson N, Esposito M, Kacperek A, Nieto-Camero J, Price T and Waltham C 2015 Proton tracking for medical imaging and dosimetry *Journal of Instrumentation* **10**(02), C02015.

Taylor J, Waltham C, Price T, Allinson N, Allport P, Casse G, Kacperek A, Manger S, Smith N and Tsurin I 2016 A new silicon tracker for proton imaging and dosimetry *Nuclear Instruments and Methods in Physics Research Section A: Accelerators, Spectrometers, Detectors and Associated Equipment* **831**, 362–366.

Tobias C A, Lawrence J H, Born J L, McCombs R K, Roberts J E, Anger H O, Low-Beer B V and Huggins C B 1958 Pituitary irradiation with high-energy proton beams: a preliminary report *Cancer Res.* **18**(2), 121–134.

Tschalär C 1968 Straggling distributions of extremely large energy losses *Nuclear Instruments and Methods* **64**(3), 237–243.

Ulmer W and Matsinos E 2012 A calculation method of nuclear cross-sections of proton beams by the collective model and the extended nuclear-shell theory with applications to radiotherapy and technical problems *Journal of Nuclear and Particle Physics* **3**, 42–56.

Vanzi E, Bruzzi M, Bucciolini M, Cirrone G P, Civinini C, Cuttone G, Presti D L, Pallotta S, Pugliatti C, Randazzo N, Romano F, Scaringella M, Sipala V, Stancampiano C, Talamonti C and Zani M 2013 The PRIMA collaboration: Preliminary results in FBP reconstruction of pCT data *Nuclear Instruments and Methods in Physics Research Section A: Accelerators, Spectrometers, Detectors and Associated Equipment* **730**, 184–190. Proceedings of the 9th International Conference on Radiation Effects on Semiconductor Materials Detectors and DevicesOctober 9-12 2012 Dipartimento di Fisica e Astronomia - Sezione di Astronomia e Scienza dello Spazio - Largo Enrico Fermi, 2, 50125 Firenze Organized by : Università degli Studi di Firenze with the support of Istituto Nazionale di Fisica Nucleare.

Wang D, Mackie T R and Tomé W A 2011 Bragg peak prediction from quantitative proton computed tomography using different path estimates *Physics in Medicine and Biology* **56**(3), 587–599.

Wang D, Mackie T R and Tomé W A 2012 On proton CT reconstruction using MVCT-converted virtual proton projectionsa) *Medical Physics* **39**(6), 2997–3008.

Wang D, Mackie T and Tomé W 2010 On the use of a proton path probability map for proton computed tomography reconstruction *Medical Physics* **37**(8), 4138–4145.

Waters L S, McKinney G W, Durkee J W, Fensin M L, Hendricks J S, James M R, Johns R C and Pelowitz D B 2007 The MCNPX Monte Carlo radiation transport code *AIP Conference Proceedings* **896**(1), 81–90.

West D 1975 The potential of proton radiography *in* 'Seventh International Conference on Cyclotrons and their Applications' Springer pp. 503–506.

West D and Sherwood A 1973 Proton-scattering radiography *Non-Destructive Testing* **6**(5), 249–257.

West D and Sherwood A C 1972 Radiography with 160 MeV protons *Nature* **239**, 157–159.

Williams D C 2004 The most likely path of an energetic charged particle through a uniform medium *Physics in Medicine and Biology* **49**(13), 2899–2911.

Wilson R R 1946 Radiological use of fast protons. *Radiology* **47**(5), 487–491.

Wong K, Erdelyi B, Schulte R, Bashkirov V, Coutrakon G, Sadrozinski H, Penfold S and Rosenfeld A 2009 The effect of tissue inhomogeneities on the accuracy of proton path reconstruction for proton computed tomography *AIP Conference Proceedings* **1099**(1), 476–480.

Yang M, Zhu X R, Park P C, Titt U, Mohan R, Virshup G, Clayton J E and Dong L 2012 Comprehensive analysis of proton range uncertainties related to patient stopping-power-ratio estimation using the stoichiometric calibration *Physics in Medicine and Biology* **57**(13), 4095–4115.

Yepes P P, Eley J G, Liu A, Mirkovic D, Randeniya S, Titt U and Mohan R 2016 Validation of a track repeating algorithm for intensity modulated proton therapy: clinical cases study *Physics in Medicine and Biology* **61**(7), 2633.

Zhang Y and Ning R 2008 Investigation of image noise in cone-beam CT imaging due to photon counting statistics with the Feldkamp algorithm by computer simulations *Journal of X-ray Science and Technology* **16**(2), 143–158.

Zips D and Baumann M 2013 Place of proton radiotherapy in future radiotherapy practice *Semin Radiat Oncol* **23**(2), 149–153.

Zygmanski P, Gall K P, Rabin M S Z and Rosenthal S J 2000 The measurement of proton stopping power using proton-cone-beam computed tomography *Physics in Medicine and Biology* **45**(2), 511–528.